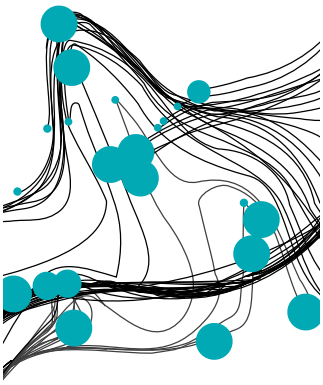

Soft Robotics Lab

Design and Development of a Multi-Axis 3D Weaving Printer for Fiber-Reinforced Multi-Material Cylindrical Structures

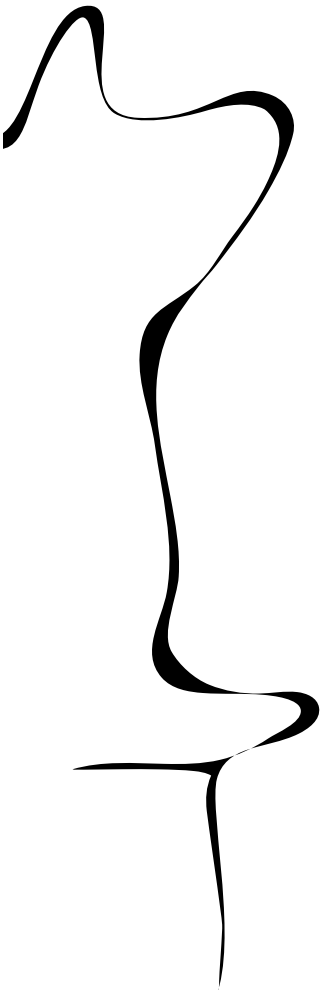

Inês Nunes Borges Pinto
Master Thesis

Committee:
prof.dr.ir. H. van der Kooij (Herman)
dr. A. Sadeghi (Ali)
dr. I. Tamadon (Izad)

March, 2025

Biomechanical Engineering
ET
University of Twente
Building 'Horstring West'
Drienerlolaan 5
7522 NB Enschede
The Netherlands

UNIVERSITY OF TWENTE.

Acknowledgements

First and foremost, I would like to thank my supervisor, Dr. Ali Sadeghi, for his support throughout this period and for turning this project idea into an actual master's thesis assignment. Thank you for allowing me to explore and adapt to this deeply fascinating and challenging field of 3D printing. I truly believe you have enabled me to develop a diverse skill set and knowledge that I can carry with me into many different fields in the future. To the other members of my examination committee, Prof. Dr. Ir. Herman van der Kooij, as chair, and Dr. Izad Tamadon, as an external member, thank you for your time and for your thoughtful assessment of my work.

To the entire lab team—thank you for your constant support, assistance, and companionship. To the PhD candidates, Luca Grignaffini and Mohammad Imanian, for your unwavering help in every situation. Even when it was not required, you never refused to lend a helping hand, share your deep expertise, and, of course, ensure an enjoyable working environment. To Paula, Júlia, Iven, and Marina, for all the (countless) experiences and laughs we shared, as well as all the work we managed to accomplish against all odds. A special thank you to Marina Gómez for all the extra help and for maintaining (and testing) my sanity and patience. The past year has been a truly memorable experience that I will carry with me forever, and it would not have been the same without all of you.

To my friends, all around the world, whether close or far away—your support has always been felt. To my roommate, for your time and patience every step of the way after my "office working hours." I appreciate your willingness to listen and your (attempts to) understand my thesis-related problems and presentations. And of course, to my family—thank you for your heartfelt support, calls, encouragement, and every big and small gesture along the way.

Lastly, to two very special people—the most important in my life. To my dad, thank you for setting me on this incredibly challenging yet equally rewarding path that is engineering. I truly hope that, wherever you are watching from, I have made you as proud as the first day I started university, following in your footsteps. And finally, to my mom—my number one supporter, the reason I have made it this far, both academically and personally—the biggest *thank you*. I truly do not know what I would have done without you. If I am standing here today, completing my master's degree, it is because of you, above anyone else.

Inês Pinto
Enschede, March 2025

Abstract

Fiber reinforcement in additive manufacturing is a promising approach to improving mechanical properties in 3D-printed structures. However, the planar deposition process of conventional fused deposition modeling (FDM) approaches has substantial restrictions on fiber alignment and placement. To overcome these constraints and broaden applications in soft robotics and biomedical implants, this thesis introduces the creation of a multi-axis 3D weaving system for embedding continuous fibers into cylindrical structures.

In order to achieve this, this study investigates hardware changes to incorporate rotating degrees of freedom into an already-existing FDM printer, allowing for automated fiber deposition in both axial and circumferential directions. Included in these adjustments are nozzle extension, print bed support optimization and controlled fiber placement. Furthermore, a unique method for generating G-code is created to support complex fiber patterns modeled after biological structures like the annulus fibrosus and non-planar deposition techniques. The system's performance is evaluated by analyzing fiber alignment, loom deposition quality, and the influence of key parameters—including fiber spacing, angles, and density—on the mechanical properties of the printed structures.

The results demonstrate how the implemented modifications influence fiber alignment and loom deposition quality, revealing the impact of multi-axis motion on fiber placement accuracy and structural consistency. Additionally, the study explores how fiber parameters, such as spacing, angles and density, affect the mechanical properties of the printed structures, providing insights into optimizing fiber reinforcement strategies. By proposing a scalable and automated methodology for fiber embedding in cylindrical geometries, this research contributes to advancing multi-axis additive manufacturing and its applicability in fiber-reinforced bio-inspired structures.

Keywords Multi-Axis 3D Printing · Fiber Reinforcement · Additive Manufacturing · Continuous Fiber Embedding · Non-Planar Deposition · Cylindrical Structures · Fused Deposition Modeling (FDM) · G-code Generation · Soft Robotics · Loom Printing · Bio-Inspired Structures · Axial and Circumferential Fiber Alignment

Contents

List of Figures

List of Tables

Nomenclature

Abbreviations

Abbreviation	Definition
SR	Soft Robotics
FRS	Fiber-reinforced Structure
CNC	Computer Numerical Control
FDM	Fused Deposition Modelling
G-code	Geometric Code
PLA	Polylactic Acid
PET	Polyethylene Terephthalate
DoF	Degrees of Freedom
HH	Head-Head Configuration
TT	Table-Table Configuration

1

Introduction & Literature Review

1.1. Soft Robotics

Challenges with Conventional Rigid Robots

It has been widely researched how **rigid link robotic manipulators**, can revolutionize industrial applications, especially in the the biomedical field. Despite their high precision and efficiency when performing specific tasks, there are still many limitations that this technology faces, namely in **adaptability**, **interaction** and **manipulation** in unstructured environments [1]:

- **Limited adaptability**: Due to their reliance on preset programming, rigid robots need sophisticated control algorithms to adjust to novel tasks or surroundings [2].
- **Unsafe interactions**: When working with people or delicate objects, their inflexible structures may present safety hazards [1].
- **Manipulation limitations**: Regarding delicate jobs like gripping soft or oddly shaped things, rigid robots are less efficient [3].

Overall, despite recent developments in sensor technology and control systems, their limited use in applications that require great **adaptability** and **safety** has remained a difficulty. As such, the research evolution in **continuum robotic manipulators** has led to the development of different manipulator designs [4], from discrete mechanisms made of a sequence of rigid links, all the way to systems made of elastic structures that may bend continuously, depicted on Fig. 1.1.

Emergence of Soft Robotics: Bio-inspired Designs and Adaptability

Thus, the field of **soft robotics**, or SR, emerged inspired by the versatility and stiffness of natural organisms. Soft robots, in contrast to their rigid counterparts, are made of **compliant materials** with low Young's modulus, like **hydrogels**, **silicone**, and **elastomers** [5].

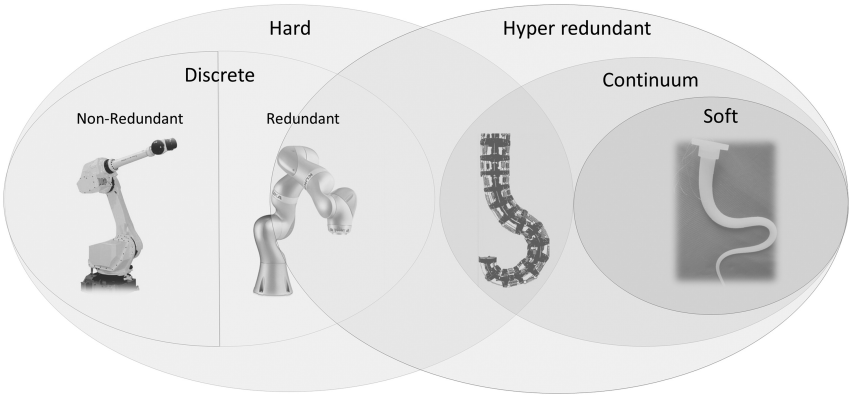

Figure 1.1 Evolution of rigid-link manipulators based on discrete mechanisms to bioinspired continuum robotic manipulators based on structures capable of continuous bending. Adapted from [4].

Ultimately they can continually deform thanks to these materials and therefore simulate different biological processes, adapting their shapes for interacting **safely** whether with humans [6] or delicate objects [3] and also navigate in unstructured and complex environments, with **enhanced adaptability** [7].

Nature is a major source of inspiration for soft robotics design ideas. For example, the architecture of plants and animals exhibit "**physical intelligence**," [5] which allows for interaction and adaptability without the need for sophisticated computing processing [3]. The ability of plant tendrils to change shape or the motion of an octopus arm [7] are two examples. These ideas have influenced the creation of soft robotic systems, which can **bend**, **twist**, and **change their structure** to carry out tasks that rigid robots cannot, especially when it comes to the intricate field **medical of applications** [8].

Applications of Soft Robotics

SR spans a broad area of applications. As previously mentioned, **Manipulation and Interaction in Unstructured Environments** is a key component for innovation in the field. These devices excel in dynamic and unstructured settings, providing flexible solutions when inflexible methods are inadequate. Soft grippers, for instance, may adapt to the forms of delicate objects, such as fruits, guaranteeing safe handling without damaging [9]. Soft robotic arms that resemble octopus tentacles have made it possible to do activities in marine exploration, like safely sampling fragile coral structures [7]. Moreover, SR has transformed instruments for **minimally invasive operations** in the medical field. Surgeons can perform laparoscopic and endoscopic procedures with greater finesse and less tissue injury thanks to flexible manipulators [10]. **Soft exosuits** help people with mobility disabilities by providing support without limiting their natural movement, thanks to their cable-driven or pneumatic actuators use [11].

However, one particularly relevant area of inspiration for this thesis is the focus on **bio-mimetic systems**, especially in mimicking connective tissues in the human body. In biology, connective tissues weave fibers together to form robust, flexible structures that connect stiff bones with soft tissues [12]. By increasing load capacity while preserving flexibility, this method encourages the adoption of **fiber-reinforced soft robots** to simulate comparable transitions. The applicability of these ideas to cylindrical objects, like lumbar disc implants, will be further explored. By imitating these biological systems, hybrid robots that combine strength and flexibility can be produced. For example, bio-mimetic robots, like muscle actuators or artificial fish, use **fiber configurations** to mimic realistic durability and mobility [13]. Additionally, biomedical soft robots have been created to mimic tendon-like actuators [14], heart valves [15], and shape-morphing components [16], all based on the concept of **fiber reinforcement**.

1.2. Fiber reinforcement

Overview of the Fiber Reinforcement Method & Applications

In the production of composites, **fiber reinforcement** is a revolutionary method that improves the mechanical characteristics of base materials such as metals and polymers. These composites are perfect for applications ranging from sports equipment to aircraft because they incorporate **fibers** into a **matrix material**, giving them exceptional strength-to-weight ratio, flexibility, and durability [17].

Fibre reinforcement's adaptability spans a wide range of applications, demonstrating its potential from **industrial** up to **bio-inspired systems**. For example, fiber-reinforced structures, or FRS, have widespread application in the **automotive**, **sports**, and **aerospace sectors**. For constructions like wind turbine blades, high-performance bicycles, and airplane fuselages, lightweight yet durable materials are essential [18].

The **connective tissues** that hold muscle to bone together in biological systems are also a clear example of fiber reinforcement, for example, [12]. Soft robotics' ability to mimic these structures opens the door to the development of **flexible and load-bearing actuators**, which will find use in biomedical devices such as implants and prosthetics [19]. More specifically, for this thesis, fiber reinforcement offers a way to simulate the **annulus fibrosus**, the hard outer layer of the intervertebral

disc, in the particular instance of cylindrical nature-inspired constructions, such 3D-printed lumbar discs [20]. This configuration offers possible options for biomedical implants by improving the **mechanical qualities** and **simulating natural load distribution**.

State-of-the-Art Methods for Fiber Embedding in Soft Robotics

By modifying the **fiber material**, **orientation**, and **density**, mechanical qualities can be customized by fiber reinforcement. **Fiber-based actuators** are employed in SR for applications like surgical instruments and artificial muscles that call for exact motion control. For instance, biological applications such as implants and prosthetics are made possible by **pneumatic actuators with embedded fibers** that replicate the actions of normal muscles [21].

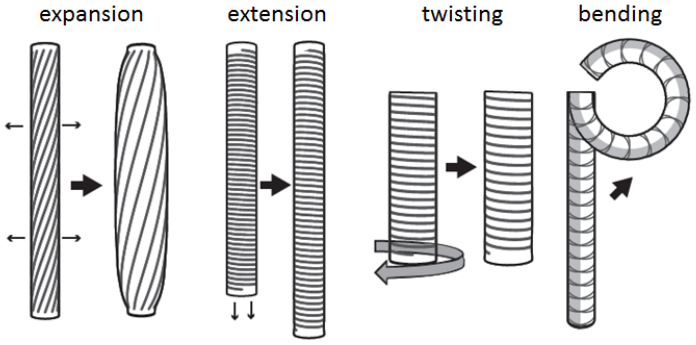

Figure 1.2 Different actuation motions based on fiber pattern. Adapted from [22]

Fiber Patterns and Materials: Soft actuator motion and deformation have been controlled by patterns including axial, helical, and radial arrangements. Axial patterns increase tensile strength and restrict elongation, whereas radial reinforcement facilitates bending and twisting motions [22, 23] (see Fig. 1.2). Because of their great strength, low weight, and sensitivity to external stimuli, materials including carbon fiber, Kevlar, and shape-memory alloys are widely used [24].

Fiber Density: A structure's stiffness and compliance are directly impacted by fiber density. While lower densities permit more flexibility, which is essential in soft robotic actuators and grippers intended for delicate manipulation, higher densities offer a greater load-bearing capability [25].

Functional Fibers: Functional fibers like conductive threads or electroactive polymers allow for energy harvesting, actuation, and sensing in soft robotic systems in addition to providing structural support. Robots can interact with their surroundings and carry out activities more precisely and adaptably thanks to these fibers, which improves their usefulness [26].

With differences in fiber size, continuity, pattern, and type, fiber reinforcement in composite materials is customized to satisfy particular structural needs. **Particulate reinforcement**, **short fiber reinforcement**, and **continuous fiber reinforcement** are the three main types of fibers that are distinguished by their length and continuity [27].

- **Particulate Reinforcement** consists of spreading tiny particles throughout the matrix substance. Because it is simple to mix and process, this method is preferred for achieving slight increases in stiffness. Increasing wear resistance and altering thermal characteristics are typical uses [28].
- **Short Fiber Reinforcement** makes use of short-length fibers, typically between 0.1 and 10 mm. This technique is extensively used in sectors like aerospace and automotive and provides increases in strength and stiffness over particle reinforcement. Short fibers are incorporated to improve mechanical qualities while preserving very straightforward processing methods [27].
- **Continuous Fiber Reinforcement** entails integrating continuous fibers into the matrix, offering better stiffness and strength than discontinuous techniques. Applications needing high load-bearing capacity and directional strength benefit greatly from this technology. Continuous fibers are necessary for soft robotics to create actuators that require precise motion control and inextensibility. The best method for creating inflated soft actuators is continuous fiber re-

inforcement, according to studies, since it guarantees the required performance and structural integrity [29].

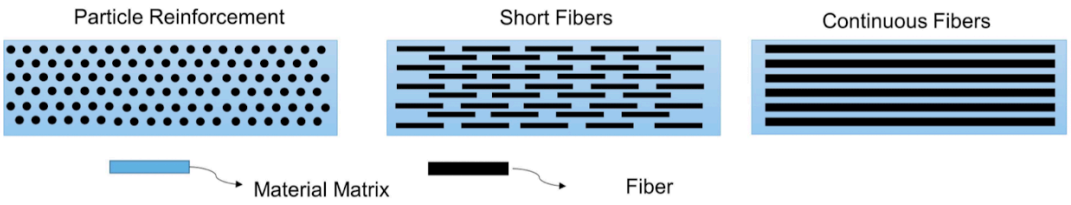

Figure 1.3 Different categories of fiber reinforcements based on the fiber size in the polymer. Adapted from [30]

Although short and particle fiber reinforcements can improve some mechanical characteristics, most inflatable soft actuators lack the necessary inextensibility. The development of 3D structures with **continuous fiber reinforcement** is therefore the main goal to satisfy the demanding requirements of these applications. However, due to its continuous and uninterrupted structure, continuous FRS require more careful consideration, especially in intricate configurations, such as **cylindrical geometries**.

1.3. Fiber Reinforcement in Cylindrical Bio-Inspired Structures

The Fiber Composition of Human Tissue

Taking a closer look into human tissue, we can see that their mechanical properties rely on the composition of the **extracellular matrix (ECM)**, which is abundant in fibrous proteins like **collagen** and **elastin**. Tissues are given **structural integrity and stiffness** by collagen fibers (shown in Fig. 1.4 (A)), which are renowned for their tremendous tensile strength. These fibers can be flexible at mild tension since they are usually crimped or wavy [12]. Collagen fibers grow taut and straighten as tissue deformation increases, greatly increasing tissue stiffness and avoiding overextension. On the other side, by providing elasticity, elastin fibers enhance this structure and allow tissues to **return to their initial shape after contracting or stretching**. For example, elastin surrounds densely packed collagen fibers in the skin to form a three-dimensional meshwork that extends from the papillary to the deep dermis. The **quantity and spatial distribution** of collagen and elastin fibers in relation to one another dictate the **tissue's mechanical response** [31]. Collagen and elastin fibers interact to give tissues their strength and flexibility, which is necessary for several physiological processes. This configuration, for instance, allows blood arteries to tolerate and adjust to the fluctuating pressures of blood flow [32].

Specific Focus on Cylindrical Structures

A crucial area of study for soft robotics and biomedical applications is fiber reinforcement in **cylindrical structures**. For these structures, like blood vessels and lumbar discs, to endure physiological loads and continue to operate, they need **special mechanical characteristics**. In production techniques, cylindrical geometries provide unique difficulties, especially when it comes to integrating **axial reinforcement** and creating **intricate continuous fiber patterns** as presented in Fig. 1.4 (B).

In many biological and engineering applications, cylindrical shapes are essential. Fibre configurations are essential to the **elasticity**, **resistance to torsional pressures** and **regulation of deformation** of natural systems such as blood vessels and tendons [33]. Similar to this, cylindrical geometries are essential for parts like fiber-reinforced pipes and pressure vessels in engineering applications, where the configuration of fibers determines **durability** and **load-bearing capability** [34]. Cylindrical structures in soft robotics can be used in biomedical implants and compliant actuators since they resemble **biological forms**.

For instance, the **annulus fibrosus**, the outer layer of intervertebral discs (Figure 1.4(C)), served as the model for these FRS. The annulus fibrosus, that provides the **tensile strength** and **confines the**

gel-like nucleus pulposus [35], has already been replicated in cutting-edge medical device artificial prototypes [36] using PET fibers (see Fig. 1.4 (D)), and can be further enhanced by being mimicked from fiber-reinforced cylindrical constructions. Replicating the **anisotropic mechanical behavior** of this natural tissue, which supports spinal motion and resists deformation under compression and rotation, requires precise continuous fiber insertion [37].

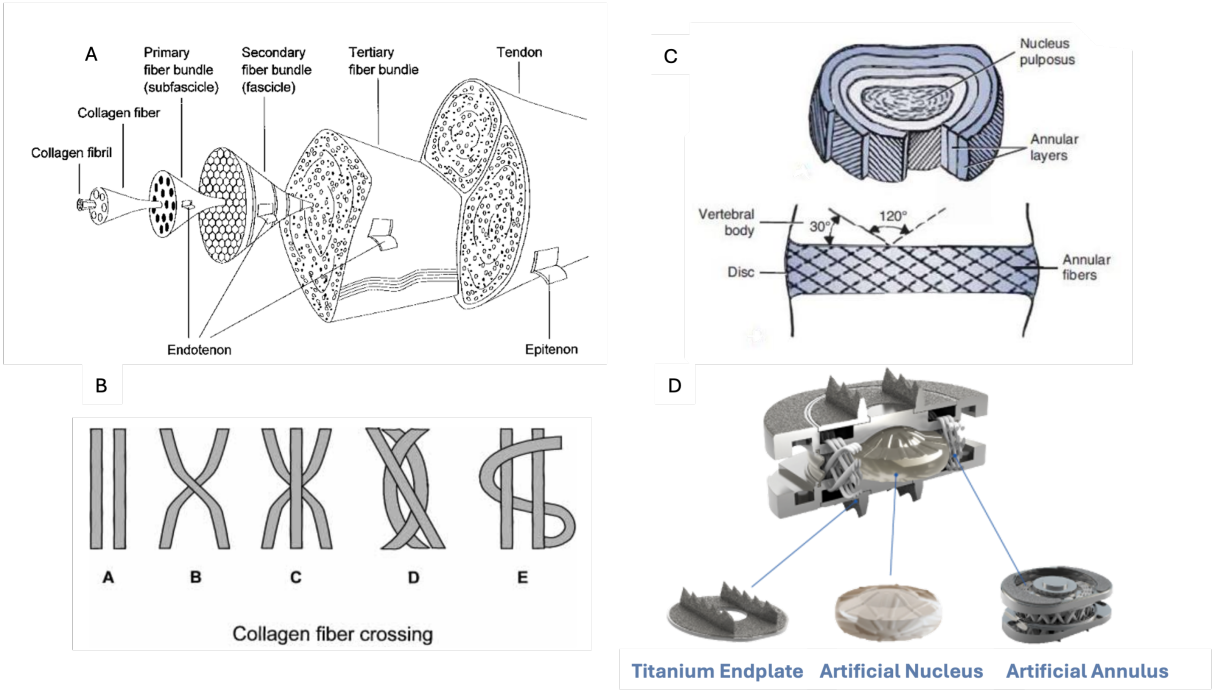

Figure 1.4 Collagen fibers in the human body and its applications (A) Overview of muscle-tendon composition [12] (B) Collagen Fibers different layout and crossing [12] (C) The annulus fibrosus [35] (D) The M6-L artificial lumbar disc and its mimicking of the annulus fibrosus [36]

Mimicking the Lumbar Disc Implant Characteristics

The mechanical and functional characteristics of the natural intervertebral disc are intended to be replicated by fiber-reinforced lumbar disc implants. But firstly, it is necessary to create **a system capable of automating such fabrication**. Tensile strength and flexibility are provided by the annulus fibrosus, which is mainly made up of collagen fibers organized in concentric lamellae. When creating fiber-reinforced lumbar disc implants, important factors to take into account are:

- **Material**: High tensile strength, flexibility, and biocompatibility are desirable qualities for the fibers employed in annulus fibrosus analogs. Commonly utilized materials include carbon fibers, polyethylene terephthalate (PET), and more sophisticated biopolymers like polycaprolactone (PCL). These substances replicate the elastic and load-bearing characteristics of the natural annulus [38]. Additionally, the implant requires structural components that mimic the vertebral endplates, which provide mechanical support and integration. Current artificial lumbar disc implants, such as the M6-L disc, utilize titanium endplates, and other materials such as PEEK (polyether ether ketone), can be used to enhance biocompatibility and osseointegration while maintaining durability [39, 40].
- **Annulus Fibrosus and Lumbar Disc Dimensions**: The dimensions of the annulus fibrosus and lumbar discs vary among individuals and across spinal levels, affecting the mechanical behavior of both natural and artificial discs. Typical lumbar disc heights range from approximately 8 mm to 12 mm, with diameters varying between 35 mm and 55 mm depending on the spinal level [37]. These dimensional constraints influence the structural design of fiber-reinforced implants and the necessary reinforcement strategies to maintain physiological load distribution.
- **Fiber Length**: Longer fibers provide for continuous reinforcement, which improves the structure's ability to disperse stress uniformly and minimizes weak spots brought on by fiber ends.

Collagen fibers are arranged in concentric lamellae within the native annulus fibrosus, and their lengths vary throughout the structure. According to studies, there is a structural adaptation to different mechanical demands since the number of fiber tracts and their lengths rise by around 50% from the inner to the outer annulus [37]. However, current commercially available fiber-reinforced implants lack this variation in fiber length across layers, leading to a uniform fiber structure that does not fully replicate the biomechanical properties of the natural disc.

- **Fiber Strength**: To endure the physiological forces imposed on the implant, especially during spinal motions like bending and twisting, high-strength fibers are needed. The mean length of the collagen fibers in the annulus fibrosus is directly correlated with its tensile stiffness, indicating that longer and more cohesive collagen fibers play a major role in the mechanical integrity of the tissue [37]. In contrast, current implant designs primarily rely on uniform fiber lengths, which may not fully optimize stiffness adaptation across different regions of the annulus.
- **Attachment and Angles**: Fibre orientation has a significant impact on implant performance. Collagen fibers are organized in concentric lamellae with alternating oblique angles in the natural annulus fibrosus. The ideal resistance to tensile and torsional forces is provided by these fiber angles, which range from roughly 25° in the inner lamellae to 45° in the outer lamellae. The annulus's mechanical qualities are improved by this change in fiber orientation, which enables it to handle challenging loading situations [37]. However, current artificial implants do not incorporate this layer-dependent variation in fiber angles, often resulting in a uniform fiber orientation throughout the structure, which may not effectively replicate the load-adaptive properties of the natural disc.

However, there are many restrictions in using current techniques for recreating these structures due to the complex fiber patterns. **Manual techniques**, as it will be further explored, are limited by their **accuracy** and **consistency** errors. Fibers must be precisely aligned along predetermined pathways, including **axial** or **circumferential** patterns, to be embedded in cylindrical geometries.

Beyond the challenges of manual fabrication, incorporating **continuous fibers** in these complex cylindrical structures without requiring fiber cuts presents a significant limitation in existing manufacturing methods. This challenge is further compounded by the need for **traveling in between layers** in standard FDM 3D printing systems. If predetermined endplates are in place, ensuring axial fiber placement becomes difficult, as material deposition in intermediate layers requires precise path planning. Traditional layer-by-layer deposition struggles to integrate axial fiber paths without disrupting the pre-existing structure.

As such, **automated approaches**, relying on 3D printing technologies, have been researched, but as layer-by-layer deposition techniques have restrictions, traditional 3D printing presents its challenges. Because they require sophisticated path planning and tension management, axial and circumferential fibers are difficult to combine simultaneously, as will be seen in the next section. A standard automated process for fiber deposition should not only allow variation of fiber patterns but also maintain **continuous fiber placement** while enabling the controlled **axial deposition of fibers across layers**. Addressing these challenges is crucial for achieving functional and biomechanically accurate fiber-reinforced disc implants.

1.4. Fiber Embedding Automation

Manual Fiber Reinforcement

To better understand the need to automate the process, let's first take a look at the most traditional and widely used manual technique: the **hand-lay-up** method (Fig. 1.5). It is used due to its ease of use and affordability, particularly in applications that call for huge, intricate designs with comparatively low production numbers [41].

Steps in the hand-lay-up process [41]

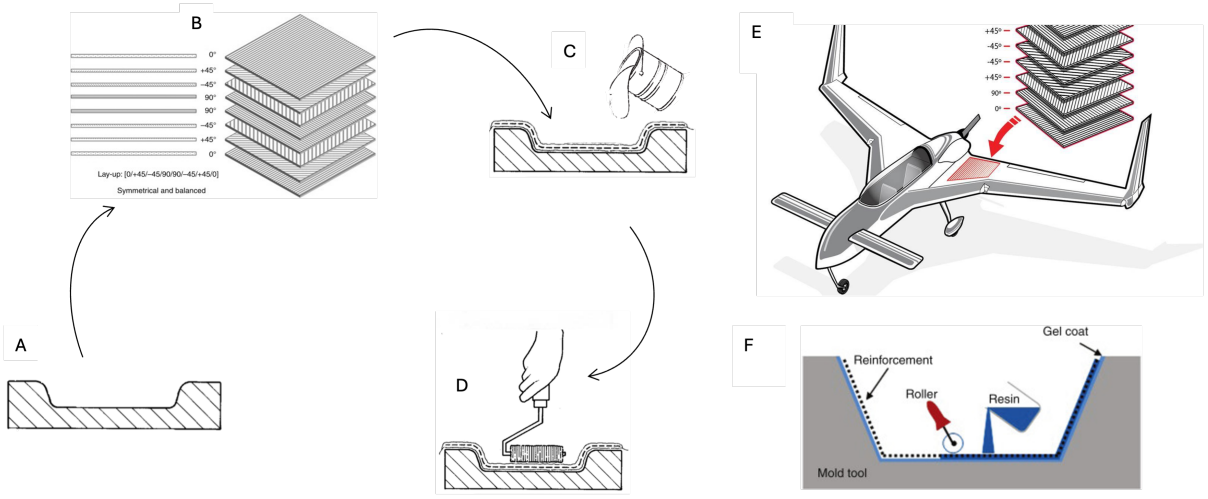

Figure 1.5 The hand-lay-up process (A) Mold preparation (B) Fiber Placement (C) Resin Application (D) Consolidation & Curing (E) Application of composite material in the final product (F) Overview of the hand-lay-up process. Adapted from [41, 42].

(A) Mold Preparation: A mold that represents the intended final product shape is carefully cleaned and given a release agent treatment. This guarantees simple demolding following the cure.

(B) Fiber Placement: Carefully placed onto the mold are reinforcement fibers, such as woven or glass fabrics. These fibers' arrangement and orientation are crucial since they affect the mechanical characteristics of the final composite.

(C) Resin Application: The fibers are covered with a thermosetting resin, usually epoxy, vinyl ester, or polyester. Brushing or spraying might be used for this. For the fibers to properly connect and convey load, the resin must completely soak them.

(D) Consolidation & Curing: Squeegees or rollers are used to remove air bubbles that were caught during the lay-up. This procedure is essential to avoid voids, which could jeopardize the composite's structural integrity. Posteriorly, depending on the resin system, the laminate is either left to cure at room temperature or higher temperatures. Curing turns the resin from a liquid into a solid, which binds the fibers together to make a strong, stable structure.

(E) Demolding & Finishing: The composite item is gently taken out of the mold once it has completely dried. Surface finishing procedures are carried out as necessary, and any extra material is cut away. The composite can then be applied to its industrial purpose.

Accuracy and **consistency** are essential in the manufacturing of fiber-reinforced actuators since even little errors can have a big effect on actuator performance. This being said, the drawbacks of these manual techniques, which mostly rely on pre-made grooves or stitching and result in **variability** and **time inefficiency**, have been addressed by **automation** [43].

Automation techniques & Advantages for Fiber Reinforcement

Automation addresses then the challenges of manual fiber embedding by [44]:

- **Improving Precision**: Consistent fiber placement and tensioning are guaranteed by automated technologies, which improve actuator performance and lower prototype variability.
- **Enhancing Scalability**: Automated methods enable mass manufacturing with consistent quality, which makes them suitable for both commercial and research uses.
- **Expanding Design Freedom**: The range of possible designs and uses is increased by automation, which makes it possible to create intricate fiber patterns that would be impossible to accomplish by hand.

As such, this process has already been investigated for SR actuation designs, with some relevant publications in the most common automation methods: **braiding**, **knitting**, **winding** and **weaving**.

- **Braiding**: Fibres are frequently embedded into cylindrical parts, such as McKibben actuators, using automated braiding machines. These technologies produce repeatable actuators by guaranteeing precise fiber angles and consistent tension. Additionally, braiding enables the input of sensors during manufacture, providing improved functionality [45, 46].
- **Knitting**: Intricate and extendable fiber designs are produced by programmable knitting machines. To incorporate sensing, knitting has been researched as a means of integrating functional fibers, such as conductive threads, into soft actuators. Although it works well for extensible applications, its intrinsic elasticity prevents it from being used in constructions that need inextensible reinforcement [26, 47].
- **Winding**: 2D fibre patterns are made using winding machines. Although these devices enable the controlled insertion of fibers in exact configurations, they are not very suitable for complex geometries [48].
- **Weaving**: Because of its inextensible qualities and capacity to produce strong forces in fiber-reinforced actuators, weaving provides a number of mechanical benefits. Conventional weaving methods create extremely robust structures by interlacing weft fibers with stationary warp fibers under strain. However, because of the intricacy of the designs and the machine requirements, converting weaving into automated procedures for 3D printing has proven difficult. The majority of weaving techniques are limited to 2D applications and do not provide answers for the axial or vertical fiber embedding that is essential for intricate soft robotics [30]. For example, there have been some artist-inspired techniques, taking the first steps into automatizing weaving. From creating a pre-made pathway for the fiber to follow through (Fig. 1.6 (A)) [49] all the way to passing fibers through a metal pin grid (Fig. 1.6 (B)) [50], to create complex structures, the proposed ideas have proven to be quite innovative. But in the end, the same issue is still present: there is a 2D limitation, and axial reinforcement needs to be placed manually and posteriorly to the automated process.

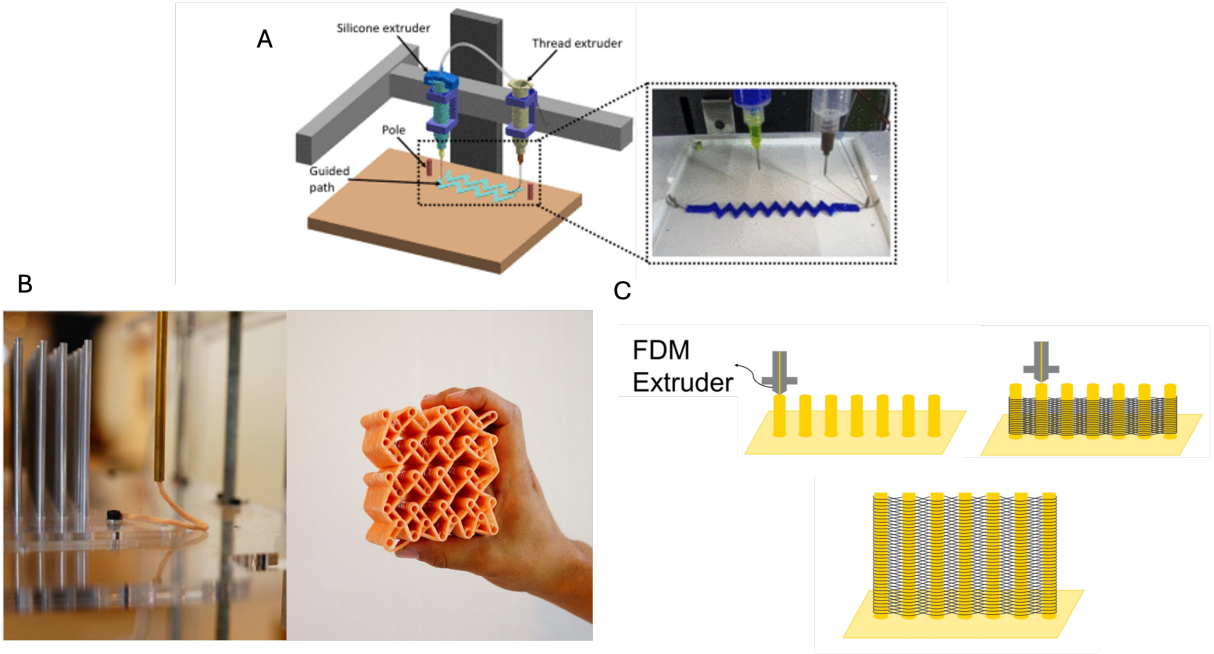

Figure 1.6 State-of-art automation proposals for weaving: (A) Embedding on a pre-made pathway [49] (B) Artistic inspired approach based on a metallic pin grid for fiber pulling and achieved structure [50] (C) Adaptation of artistic approach into 3D printing [30].

Challenges with Weaving in 3D Printing

As seen based on the previous finding, the preferred system for automating fiber embedding processes is through 3D printing. Because of its mechanical qualities, weaving is especially useful for fiber reinforcing; nonetheless, there are several obstacles to its incorporation into 3D printing: for starters, commercial weaving machines need to be significantly **modified to handle 3D geometries**

because they are designed for 2D patterns. They are challenging to modify for small-scale, customizable applications due to their size and complexity [30]. Furthermore, fibers must be placed using **controlled pulling mechanisms** because they cannot be pushed like hard 3D printing filaments can. This makes automation more difficult and induces more limitations throughout the deposition procedure [44]. Lastly, **continuous axial or vertical fibers** that **cross previous printing layers** are difficult to integrate into existing planar systems. This restriction prevents them from taking full advantage of the mechanical advantages of weaving, like improved rigidity and actuator performance [51].

As previously discussed, researchers have suggested ways to automate fiber weaving using predefined looms with metallic pins to overcome the drawbacks of 2D weaving. To create intricate 3D woven constructions, one method is to tie a fiber to a fixed location and then use a gantry system to weave it around the pins. This simplifies the process by removing the need for further stitching or sewing [50]. However, the designs and geometries that can be created are limited by metallic pins. A suggested method incorporates 3D printing for the loom itself to get around this. Customized and non-vertical designs can be produced by printing pins with movable height, diameter, and orientation straight onto the substrate (Fig. 1.6 (C)) [30]. Even with said developments, **automated vertical fiber embedding** is still a difficult task. Mimicking **bio-inspired structures**, especially **cylindrical ones** with axial fibers, is crucial for replicating natural load-bearing properties. In this thesis, inspiration is drawn from cylindrical structures, blood vessels, muscle bundles, and, most importantly, the fiber architecture of the human lumbar disc—the **annulus fibrosus**. To improve actuator performance, especially in bending and twisting motions, vertical fibers are essential.

1.5. Multi-Axis Printing for Fiber Reinforcement

Challenges of Conventional Planar Printing

The planar, **layer-by-layer methodology** of traditional FDM printers restricts their capacity to incorporate intricate fiber-reinforcement techniques, especially in cylindrical constructions. In fiber-reinforced soft robotic applications, where fiber **location** and **orientation** are crucial in determining mechanical attributes including **stiffness**, **flexibility**, and **actuation performance**, these limits become apparent.

Challenges in Non-Planar Fiber Placement [52]
Limitations of Planar Fiber Deposition Traditional planar FDM techniques restrict fiber placement to a fixed XY plane, making it difficult to align reinforcement along stress pathways in 3D structures. Fibers are deposited in stacked horizontal layers when printing cylindrical objects, hindering axial reinforcement essential for McKibben actuators and lumbar discs. The mechanical efficiency of the structure is limited since fibers cannot be aligned axially and circumferentially during the same print process if the printing orientation cannot be dynamically changed.
Challenges in Continuous Fiber Deposition Incorporating continuous fibers in complex cylindrical structures is difficult without cutting the fiber, disrupting its reinforcing properties. Axial fiber placement requires fibers to travel between layers, which is challenging in conventional FDM processes where fibers cannot traverse already printed sections without manual intervention. Predetermined endplates in implants restrict axial fiber alignment, requiring an approach that allows for seamless fiber integration while maintaining structural integrity. Incorporating the continuous fiber and endplate depositions into a single system for cylindrical structures is a challenge yet to be overcome.

Table 1.1: Challenges of Planar Printing for Fiber Reinforcement in Cylindrical Structures

The difficulties of embedding fibers in cylindrical constructions are immediately addressed by **multi-axis 3D printing**. It adds more degrees of freedom and enables dynamic adjustment of the printing plane, ultimately allowing different fiber orientations to be embedded, variance of patterns amongst the same print, and especially across different layers of the structure, all not possible with current planar printing methods.

State-of-the-Art Kinematic Systems for Multi-Axis Printing

Overview of Kinematic Structures

The **kinematic structure**, or the arrangement of joints and connections that control movement,

is the fundamental component of a 3D printer's hardware. The **hotend**, the mechanism in charge of melting and depositing material, can move spatially thanks to its arrangement. The kinematic system and the hotend work together to perform the core task of FDM printing: the kinematic framework moves the material in relation to the build plate, guaranteeing precise placement, while the hot-end deposits material. **Rotational movement** can be added to the printhead or the print bed to enable **multi-axis additive manufacturing**. Research and industry have investigated a number of kinematic designs with differing levels of accessibility and complexity [53].

There are two main reasons why choosing the right kinematic system is essential. First, **kinematic errors** are a major cause of mistakes in 3D printing, and accuracy and precision are crucial for producing high-quality prints [54]. Second, the **accessibility** and **viability** of adapting or updating the printer for multi-axis applications are greatly impacted by cost and complexity [55].

Conventional FDM printers frequently use a variety of kinematic structures, such as Cartesian, delta, and polar systems. **Cartesian systems** are the most widely used of these because of their ease of use and excellent accuracy. Based on how their parts move, such as whether the bed or hotend moves along particular axes, cartesian printers can be further divided into different categories [56].

The **CoreXY system**, a recent development in Cartesian kinematics, uses a belt-driven motion mechanism that lowers the gantry's moving mass to improve print speed and stability. This technique allows for high-speed printing without sacrificing accuracy while increasing movement speed and reducing vibrations [57].

Even with these developments, traditional FDM systems only have **three DoFs**: no rotation and three linear movements (X, Y, Z). Since fiber reinforcement embedding is limited to a fixed XY plane due to these limitations, multi-axis printing is a necessary progression to permit more sophisticated fiber-reinforced structures, such as **axial fibers**.

Robotic Arms

According to the way motion is conveyed through their connections, multi-axis systems can be roughly divided into serial and parallel manipulators.

Motion moves from one joint to the next in serial manipulators, which are made up of successively coupled linkages. The **robotic arm**, which normally has six DoFs (3 translational + 3 rotational DoF), is a well-known example. Because of their great adaptability and broad range of motion, robotic arms are a perfect fit for multi-axis additive manufacturing (AM). They are less available for consumer and prosumer applications, nevertheless, due to their **high cost and complexity** [58].

3+2 Axis Mechanism

The **3+2 axis mechanism**, which incorporates two more rotational degrees of freedom into a standard 3-axis FDM printer, is an alternative to robotic arms that strikes a compromise between **cost**, **accessibility**, and **performance**. This hybrid strategy preserves system affordability while providing notable increases in fiber installation flexibility [59].

This mechanism can be classified into three main configurations based on how the two additional axes are distributed [59] as seen in Fig. 1.7:

- **Table-Table (TT) Configuration**: The workpiece can be dynamically reoriented by applying rotational movements to the print bed. This configuration is appropriate for cylindrical fiber-reinforced constructions such as lumbar discs because it makes printing on curved surfaces and non-planar geometries easier.
- **Table-Head (TH) Configuration**: A more flexible configuration is made possible by placing one axis on the bed and another on the hotend. For hybrid additive-subtractive manufacturing systems, where milling tools are employed in addition to printing to increase surface quality, this configuration has been investigated.
- **Head-Head (HH) Configuration**: Because both extra degrees of freedom are housed in the hotend assembly, print orientation may be precisely controlled without relocating the print bed.

However, because of the additional heft and complexity of the print head, this arrangement is more difficult to install.

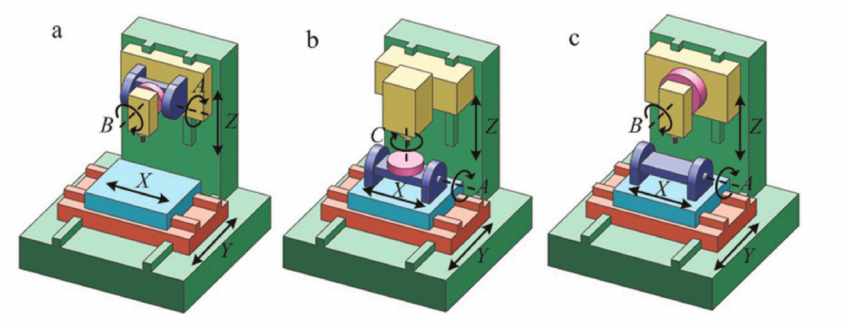

Figure 1.7 Kinematics configurations for 3+2 axis mechanism: (A) head-head; (B) table-table; and (C) head-table [59].

A modified **Creality Ender 5 Plus** printer was used for this study's system starting, taking advantage of its robust frame and high print volume. This arrangement enables continuous fiber deposition in both axial and circumferential directions, which is essential for printing biological structures like the lumbar disc's **annulus fibrosus**.

By incorporating **multi-axis kinematics** into an accessible platform, this research aims to bridge the gap between fiber reinforcement and intricate 3D structures, enabling new possibilities for biomedical applications, and implementing an automation approach for **fiber embedded cylindrical structures**.

Extending the Hot-End for Multi-Axis Printing

The **hot-end assembly** (see Fig. 1.8) in traditional FDM printing is made up of a **cold zone** (heat sink and cooling system) and a **melt zone** (nozzle and heat block), which are joined by a heat break to avoid excessive heat transmission. The filament is forced through the hot end by the extruder, where it melts and is deposited along the print path. The hotend is moved in relation to the build plate by the kinematic system, which enables accurate material placement [60].

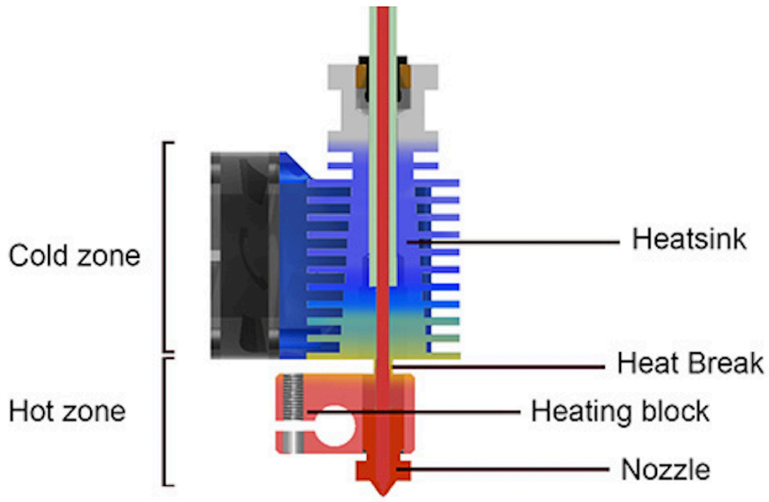

Figure 1.8 Schematic representation of hot-end, showing components and temperature [60]

Additional degrees of freedom for multi-axis printing result in new **geometric limitations** that affect hardware design. Non-planar toolpaths provide interference problems because sections of the printed geometry may **block nozzle movement**, especially when tilting or rotating the printing plane, in contrast to typical planar printing, where the nozzle stays above the part [61].

Long-throated extruders are a possible solution to this problem to improve the distance between the nozzle tip and the surrounding hardware. Interference with previously deposited layers can be reduced by **increasing the nozzle length**. But there are drawbacks to this design [62]:

- **Thermal Management**: The filament may cool before extrusion if the heat block is positioned too far from the nozzle, which raises the possibility of clogging.
- **Cooling Limitations**: Extended nozzles frequently have inadequate cooling ducts, which lowers the surface quality and print speed.
- **Clearance trade-offs**: Although an elongated nozzle lessens interference, it also alters the dynamics of material flow, which could result in uneven extrusion.

Henceforth, independently of the chosen design for the multi-axis system implementation, it is recommended to account for the possible changes regarding hot-end elongation and modifications.

1.6. Research Goal and Outline of Report

The goal of this thesis is to address the challenges of **fiber reinforcement in conventional 3D printing** by developing a **multi-axis 3D weaving system for embedding continuous fibers into cylindrical structures**. Traditional planar deposition limits fiber alignment in automated additive manufacturing reinforcement processes. This work proposes a technique that enables axial fiber placement by integrating a multi-axis kinematic system, expanding the potential applications in SR and biomedical implants.

To achieve this, the research first focuses on the **hardware modifications** required for a multi-axis printing system by introducing **rotational degrees of freedom** to an existing FDM printer. This includes modifying the **print bed support**, **extending the nozzle**, and ensuring **precise automated fiber deposition and positioning**. Next, a **custom G-code generation method** is developed to control the system, incorporating non-planar deposition strategies, toolpath modifications, and axial fiber patterns inspired by human connective tissues, particularly the annulus fibrosus. Finally, the study examines the influence of **fiber spacing**, **angles** and **density** on the **stiffness**, **extensibility**, and overall **load distribution** of the printed structures.

This research is structured around one central question:

How can we develop a multi-axis 3D weaving system for fiber-reinforced multi-material cylindrical structures?

To address this, the study is divided into four sub-questions:

1. **How can we modify an existing FDM printer to enable multi-axis fiber weaving?**
2. **How can we generate a custom G-code to control fiber deposition in a multi-axis system?**
3. **How do the implemented modifications affect fiber alignment and loom deposition quality?**
4. **How do fiber parameters (spacing, angles, and density) influence the mechanical properties of the printed structures?**

By proposing a scalable and automated system for embedding continuous fibers into cylindrical geometries, this thesis aims to advance fiber-reinforced additive manufacturing and unlock new possibilities for axial reinforcement in bio-inspired 3D-printed structures.

2

Materials and Methods

2.1. Requirements & Process

Generalized Requirements for a Multi-Axis Fiber Weaving System

1. **Multi-Axis Motion Capability**
    - The system must allow for rotational and translational movement to achieve non-planar fiber deposition.
    - This ensures proper fiber alignment along both axial and circumferential directions.
2. **Advanced Extrusion and Fiber Deposition Mechanism**
    - The extrusion system must be capable of handling fiber and filament materials simultaneously.
    - It should allow for precise placement and tension control to maintain fiber integrity and filament structure accuracy. Additionally it should account for the nozzle extension requirements to avoid printing collisions.
3. **Custom Toolpath Generation**
    - The system should support custom G-code or slicing algorithms tailored for multi-axis motion.
    - It must accommodate complex patterns and variable fiber orientations across different layers as well as the loom/endplate generation process
4. **Scalability and Structural Compatibility**
    - The system must be adaptable to different fiber orientations across the cylindrical geometries.
    - It should allow for variations in fiber density, angle, and deposition strategy.
5. **Integrated Control and Automation**
    - The printing process must be automated to maintain consistency in fiber deposition.
    - The control system should allow for real-time adjustments to compensate for tension variations and positioning errors.

Proposed Methodology for Multi-Axis Fiber Embedding

The following procedure was traced out to fulfill the specified requirements for a multi-axis 3D weaving system. This step-by-step method guarantees that the computational and hardware adjustments are in line to allow for the automatic deposition of continuous fibers in cylindrical constructions. Nonetheless, we ran into some obstacles during the implementation of this system, as expected, which motivated the changes in design and manufacturing that were performed, as well as the required tests for validation afterward, as will be seen in Fig. 2.1.

The first step involves selecting and implementing a **suitable multi-axis kinematic system**, based on the possible 3+2 configurations that were already discussed, with a focus on adapting an existing FDM printer by incorporating rotational degrees of freedom. This modification will allow for precise deposition of fibers in both axial and circumferential orientations, overcoming the limitations of traditional planar FDM printing.

Next, a **dual-extrusion system** needs to be developed to accommodate both thermoplastic and fiber materials. This will involve modifying the fused filament nozzle, to account for elongation requirements and also create an extrusion setup to ensure proper fiber alignment, control deposition tension and maintain fiber placement accuracy.

After the hardware changes, **the printed loom method**—which involves printing a scaffold structure onto a cylindrical substrate, to simulate the endplates in the artificial implants—will be investigated. Inspired by previous works [50], the goal is set to printing stackable pins on a cylindrical surface, that allows the **fibers to be pushed through**, set in place according to the desired pattern, and that lock them in, incorporating them into the overall composite structure.

MATLAB and Grasshopper will be used to create a custom G-code generation process that will allow for exact fiber deposition. Determining the non-planar toolpaths needed for fiber placement requires this **computational phase**. Fiber orientation will be dynamically controlled by the generated G-code, guaranteeing uniform patterns throughout the cylindrical construction as well as achieving a printed loom on a conformal surface.

Once the G-code workflow is established, a **printing process** tailored for cylindrical fiber-reinforced structures will be implemented.

By **analyzing all the encountered issues** during the development process, a set of experimental procedures will be defined to evaluate the several system modifications that affect the outcome of the prints.

Lastly, the printed samples will be **embedded in a matrix material** which will allow for testing how variations in fiber parameters—such as spacing, angles, and density—affect stiffness, extensibility and overall load-bearing performance. The results will provide insights into how fiber placement strategies influence the mechanical behavior of bio-inspired cylindrical structures.

Printing Process

The printing process for the fiber-reinforced cylindrical structures follows a multi-step workflow that integrates both traditional fused deposition modeling (FDM) and fiber weaving. The process is structured into three main steps, interspersed with tool changes to accommodate different fabrication stages.

1. **Printing the Loom Pins**: The process begins with the deposition of the *loom pins*, which serve as structural supports for fiber placement. These pins are strategically positioned around the cylindrical frame to define the fiber path and anchoring points. Precise placement is critical to ensure uniform fiber distribution and predictable mechanical behavior.
2. **Weaving the Fiber**: Once the loom pins are printed, a *tool change* occurs, switching from the extruder nozzle to the fiber extrusion mechanism. The fiber is then *tensioned and guided* through the loom, following a predefined weaving pattern. The number and spacing of pins dictate the fiber's *angle, extensibility, and structural reinforcement properties*.
3. **Printing the "Locking Mechanism"**: After the fiber is laid, another *tool change* is performed to switch back to the FDM extruder. A "locking mechanism" is then printed over the woven fiber, ensuring that it remains securely embedded in the final structure. This step is essential for integrating the fiber within the printed matrix and enhancing bonding strength, simulating the effect of an endplate. This printing mechanism also allows for the printing of a new support ring, which allows for further layers in the print, maintaining the continuous fiber structure.

Throughout the process, **synchronized movements of the rotational axes (U and V) and linear translations (X, Y, Z)** ensure seamless transitions between printing and fiber embedding. The **G-**

code generation accounts for these tool changes, enabling a **continuous, automated process** that combines fiber weaving with additive manufacturing.

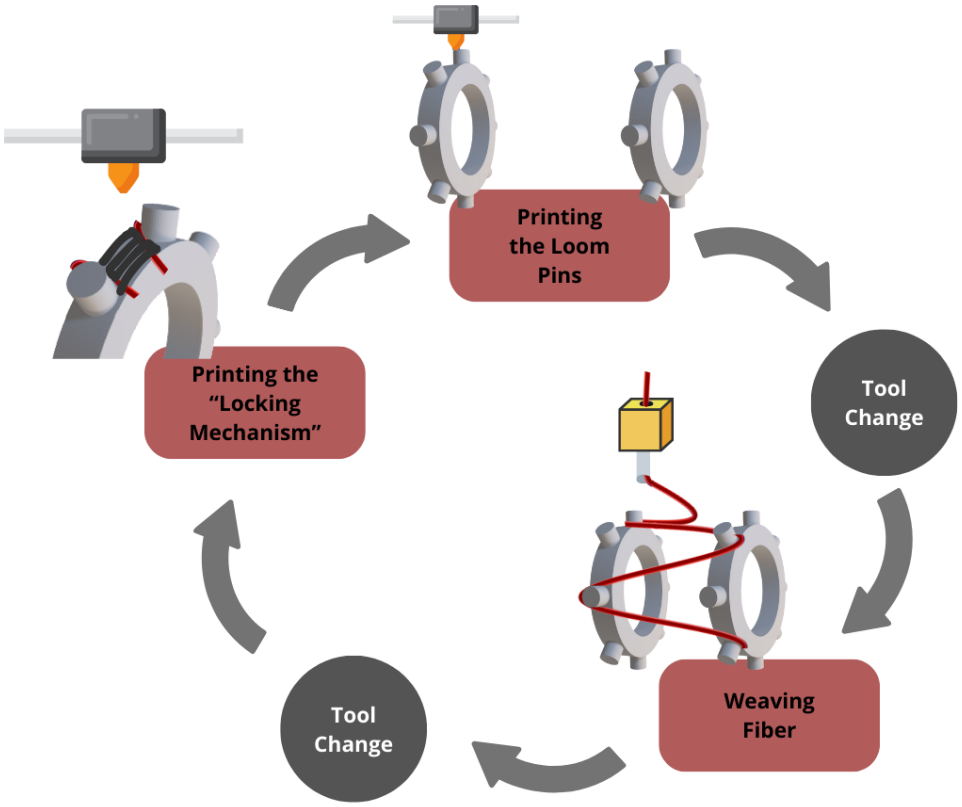

Figure 2.1 Illustration of the multi-step printing process integrating tool changes for fiber-reinforced structure fabrication. The process involves printing the loom pins, weaving the fiber, and securing the structure with a locking mechanism, ensuring controlled reinforcement and structural integrity.

2.2. Materials

For the fabrication of the loom, **Polylactic Acid (PLA)** was chosen due to its ease of printing, dimensional stability, and suitability for structural components. As the fiber material, **Dyneema Ultra-High-Molecular-Weight Polyethylene Fiber** with a diameter of 0.1 mm was selected for its high mechanical strength and low extensibility, ensuring reliable reinforcement. The elastomeric matrix material used for embedding the fiber-reinforced structures was **Ecoflex 00-10 (Smooth-On)**, a commonly used soft elastomer in soft robotics applications.

The printing system was based on a **Creality Ender 5 Plus**, which was modified to include additional rotational axis and fiber deposition mechanisms. The printer modifications were implemented through **Duet WiFi** and **Duex5 control boards** running on **RepRap Firmware**, enabling multi-axis control and precise toolpath generation. Key hardware modifications included two 1.8° **NEMA 17 stepper motors**, four **GT2 pulleys** (60-tooth, 40-tooth and 2 20-tooth), two **GT2 belts** (200 mm and 224 mm), **8 mm flange bearings**, **8 mm shaft collars** and a **slewing ring bearing** for rotational support. Thermal management was achieved using **dual hotend heater blocks**, **two thermistors** for temperature regulation, and a combination of hotend, part cooling, and board cooling fan connections.

For the extrusion process, nozzle modifications were implemented to avoid multi-axis constraints while maintaining print accuracy. The system incorporated an **E3D Super Volcano Nozzle 0.8 mm** and an **MK8 Brass Nozzle 0.4 mm**, along with **hex spacers** featuring female-female and male-female openings.

2.3. Theoretical background

Stepper Motor Calculations for Multi-Axis Printing

Stepper motors, which advance in discrete steps to accurately control movement, power the X, Y, and Z axes in traditional FDM printers. The way stepper motors work is based on a set number of steps each complete 360° rotation. For example, a 1.8° stepper motor typically has 200 steps per revolution (since 360°/1.8° = 200). The printer can precisely position the hotend relative to the build platform by managing the movement of the stepper motor.

Additional **rotating degrees** of freedom must be added to support multi-axis printing. Using **stepper motors and a pulley system** to incorporate a rotational axis is one of the simplest and most effective ways to accomplish this. One of the most straightforward and useful configurations is the **TT (table-table) setup**, in which both rotational axes are implemented at the print bed level. There are various benefits to this configuration, since it minimizes the modifications to the hotend, maintaining printhead stability and reducing the complexity in motion control.

To calculate the movement of the rotational axis, it is essential to determine the steps per degree of rotation based on the stepper motor specifications and pulley system ratios.

Pulley Ratio Calculation

The **ratio** is determined by comparing the number of teeth on the stepper motor pulley and the driven pulley. A larger driven pulley results in a reduction in rotational movement per step, increasing precision:

$$\text{Ratio} = \frac{\text{Teeth on the driver pulley}}{\text{Teeth on the motor pulley}}. \tag{2.1}$$

Steps per Degree Calculation

The **steps per degree** can be calculated using the following equation:

$$\text{Steps per degree} = \frac{SPR \times \text{Microstepping} \times \text{Ratio}}{360}, \tag{2.2}$$

where:

- SPR = Steps per revolution of the stepper motor (e.g., 200 for a 1.8° stepper motor);
- Microstepping = The number of subdivisions per full step (e.g., 16x microstepping divides each step into 16 finer steps);
- Ratio = The pulley ratio, which determines the angular movement per step;
- $360°$ = The total degrees in a full revolution.

Buil area and volume

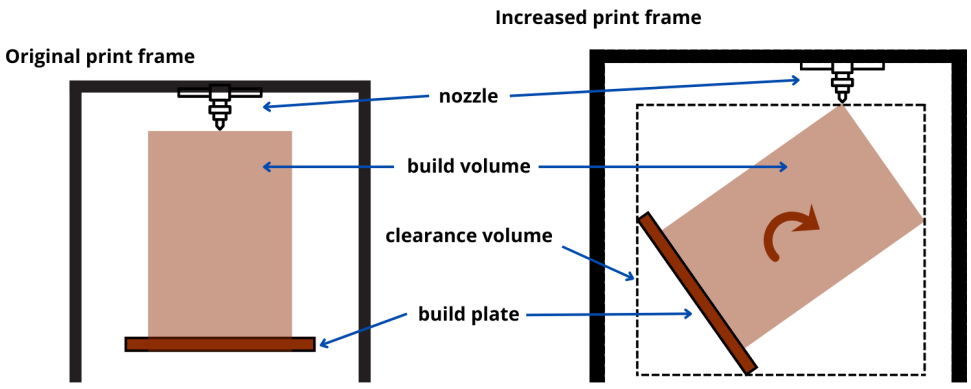

Figure 2.2 Increase in relative printer size to accommodate rotation of print-bed

The Cartesian X, Y, and Z axes determine the build volume in conventional FDM printing, where the printhead deposits material on a stationary build plate **layer by layer**. The build plate itself, however, rotates along two extra degrees of freedom in a table-table (TT) configuration, changing the effective **build volume** and requiring careful consideration of **clearance space**.

The **clearance volume** becomes crucial when rotation is included in the build system. The extra space required to guarantee that the printhead can reach every area of the build volume without encountering any obstacles is referred to as the clearance volume. The revolving print bed's motion requires this additional volume, as depicted in Fig 2.2.

To determine the clearance volume in a **TT configuration**, the required space must be calculated based on the movement of the rotating bed. The equation for the clearance volume is:

$$V_{\text{clearance}} = \sqrt{\sqrt{w^2 + l^2}^2 + h^2}, \tag{2.3}$$

where:

- w is the width of the original build volume;
- l is the length of the original build volume;
- h is the height of the original build volume.

This equation considers the diagonal movement of the build platform due to rotation. Since the **TT configuration rotates around the centroid of the build area**, the effective diagonal must be accounted for to prevent collisions and ensure accessibility.

When adding rotation to the print bed, the effective build volume is reduced compared to a standard Cartesian printer. The reduction is due to the constraints imposed by the need for additional clearance and the geometric limitations of a rotating system. The **reduced build volume** is given by:

$$V_{\text{reduced}} = \frac{\min(l, w, h)^3}{3^{3/2}}, \tag{2.4}$$

where:

- $\min(l, w, h)$ represents the smallest dimension of the original build volume;
- The denominator $3^{3/2}$ is a scaling factor that accounts for the loss in usable volume due to rotation and clearance constraints.

The greatest cubic space that can be accommodated in the rotating workstation while maintaining complete printing accessibility is estimated by this formula. The **effective build volume is always less than in a conventional Cartesian system** since the TT configuration requires a large amount of room for rotation.

Print Bed Clearance

In a multi-axis printing system, the **clearance between the print bed support and the cylindrical support** plays a crucial role in determining the system's stability. When the cylindrical support is rotated (e.g., by 90°), the print bed's tendency to shift at an angle θ depends on the clearance distance d and the height of the cylindrical support h (Fig. 2.3).

The shifting angle θ can be approximated using:

$$\theta = \tan^{-1}\left(\frac{d}{h}\right), \tag{2.5}$$

where:

- d is the horizontal distance from the center of rotation to the edge of the cylindrical support;
- h is the height of the cylindrical support from the print bed;
- θ is the shifting angle, which affects print bed stability.

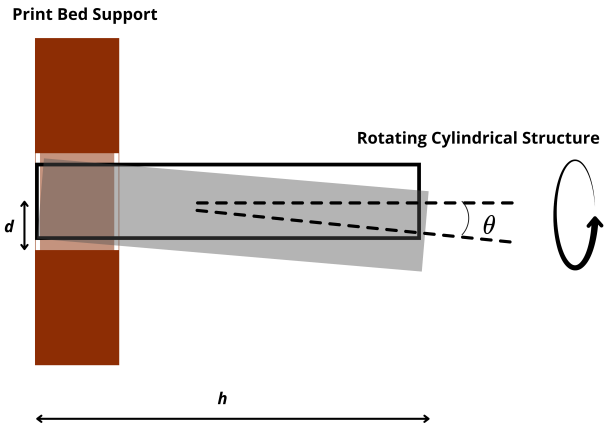

Figure 2.3 Illustration of print bed clearance and its impact on rotational stability. The clearance distance d between the bed support and the cylindrical printing surface influences the shifting angle θ. A larger height h reduces instability by minimizing angular deviation during rotation

A larger value of θ corresponds to greater instability, meaning the print bed is more susceptible to unwanted movement during the printing process. To enhance stability, the design should aim to:

- **Increase** h: A taller cylindrical support reduces θ, minimizing print bed shifting.
- **Decrease** d: Reducing the clearance distance lowers θ, further improving stability.

By optimizing these parameters, the print bed can remain more stable during multi-axis printing, reducing alignment errors and improving print accuracy.

Printing Accuracy

To evaluate the **printing accuracy** of the loom structures after implementing print modifications and custom G-code, the deviation between the designed and printed dimensions is quantified. The accuracy of the printed features is determined using the following formula:

$$S = \frac{L_D - L_M}{L_D} \times 100\%. \tag{2.6}$$

Where:

- S represents the accuracy deviation percentage;
- L_D is the designed length (reference dimension from CAD model);
- L_M is the measured length (actual dimension of the printed part).

This formula quantifies the relative error in the printed parts, allowing for the assessment of dimensional precision. By applying this method to the loom structures, it becomes possible to analyze how **print modifications**, **nozzle adjustments**, and **G-code alterations** affect dimensional consistency. A lower S value indicates higher accuracy of the printed loom which ultimately influences the fiber deposition.

Extrusion Calculations

In multi-axis fiber embedding, **precise extrusion control** is crucial for both standard material deposition and fiber locking. The extrusion amount E is determined based on the volume of material required for a given print path. This section presents two equations: one for normal extrusion and another for cases where fibers need to be locked in place by additional material.

For normal fused deposition modeling (FDM) printing, the extruded material volume is calculated as:

$$E = \frac{h \times L \times W}{\pi \times \frac{d^2}{4}}. \tag{2.7}$$

Where:

- E is the extrusion amount;
- h is the layer height;
- L is the line length;
- W is the line width;
- d is the filament diameter.

In this sense, it is ensured that the correct volume of material is extruded to form a continuous track with the desired dimensions.

When embedding fibers into the structure, additional material is required to ensure stability and adhesion. To account for the volume occupied by the fiber, the extrusion calculation is modified as:

$$E = \frac{h \times L \times W - \frac{\pi \times D^2}{4}}{\pi \times \frac{d^2}{4}}, \tag{2.8}$$

where:

- D is the fiber diameter;
- The term $\frac{\pi \times D^2}{4}$ represents the cross-sectional area of the embedded fiber, which must be subtracted from the extruded material volume.

This adjustment ensures that the fiber remains securely in place without **excessive extrusion** that could lead to deformations or print instability. By dynamically adjusting the **extrusion amount**, the system can effectively integrate continuous fibers into cylindrical structures while maintaining print accuracy and mechanical integrity.

Loom and Fiber Parameters

To analyze how fiber distribution influences mechanical properties, we focus on **pin spacing**, **fiber density**, and **load distribution per pin**. These factors are critical in mimicking **the collagen fiber crossing of the annulus fibrosus** (see Fig. 1.4 (B)), where fibers are arranged at varying angles to control stiffness and load distribution.

The **stiffness** of the fiber structure depends on how fibers navigate the cylindrical loom, particularly the number of pins and their angular spacing. As the number of pins increases, fibers follow a more constrained path, reducing their ability to stretch freely.

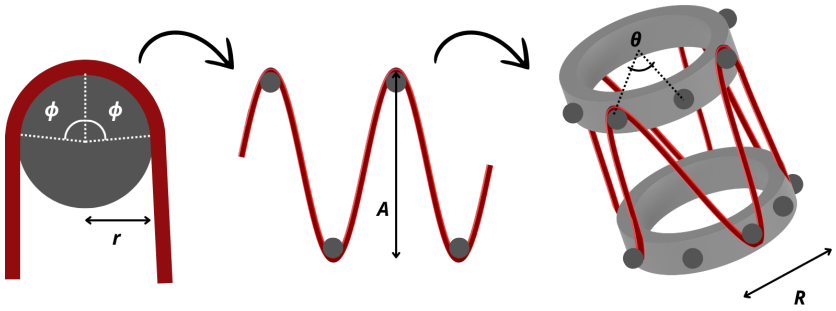

Figure 2.4 Illustration of the fiber pattern using the proposed method, based on the fiber orientation on the inspired bio-structure

For a regular distribution of pins along the circumference, each fiber segment follows an **arc**, with a segment length:

$$s = R\theta, \tag{2.9}$$

where R is the radius of the cylindrical structure and θ is the angle between two consecutive pins. The **total woven fiber length** across n pins can be approximated as:

$$L = n(2R\phi + \sqrt{A^2 + s^2}). \tag{2.10}$$

Where:

- n is the number of pins;
- R is the cylinder radius;
- r is the pin radius;
- θ is the angular separation between pins;
- ϕ is the fiber wrap angle around each pin;
- A is the amplitude of fiber displacement;
- $s = R\theta$ is the circumferential distance between adjacent pins.

Since fibers are cylindrical, the **fiber volume** can be computed as:

$$V_f = L_f \cdot \pi r_f^2, \tag{2.11}$$

where r_f is the fiber radius.

The effective **Young's modulus** of the composite structure is given by:

$$E_c = \frac{V_f}{V_m + V_f} E_f + \left(1 - \frac{V_f}{V_m + V_f}\right) E_m. \tag{2.12}$$

Where:

- E_c is the composite Young's modulus;
- V_f and V_m are the fiber and matrix volumes;
- E_f and E_m are the Young's moduli of the fiber and matrix materials.

By increasing V_f, the overall stiffness increases, reducing deformation. We can quantify the effect of **pin angle ϕ and fiber volume fraction on stiffness**. A larger ϕ increases fiber length and volume, leading to a higher reinforcement effect, similar to the graded stiffness found in annulus fibrosus tissue.

Since fibers interact with multiple pins, understanding how **forces are distributed** is crucial. The force felt at each pin is inversely related to the number of contact points:

$$F_{\text{pin}} = \frac{F_{\text{total}}}{n}, \tag{2.13}$$

where:

- F_{pin} is the force per pin;
- F_{total} is the total applied force;
- n is the number of pins.

This equation suggests that as **the number of pins increases**, the force per pin decreases.

To determine the **smallest printable loom pin dimension**s based on machine constraints, we use the arc length formula, which relates the radius of a circular path to the subtended angle:

$$s = R\theta. \tag{2.14}$$

Where:

- s is the arc length (or the spacing between loom pins in the circumferential direction);
- R is the radius of the cylindrical print bed;
- θ is the angle in radians that corresponds to the spacing between two consecutive pins.

To ensure proper pin placement within the machine's constraints, the **smallest feasible spacing between pins** is dictated by the minimum printable arc length. Given the machine's build volume and the smallest practical printable pin radius r_{min}, the smallest spacing can be expressed as:

$$\theta_{min} = \frac{s_{min}}{R}. \tag{2.15}$$

Where s_{min} is the minimum feasible spacing based on the print resolution.

If a specific arc length s is required for a given angular spacing θ, the necessary print bed radius can be calculated as:

$$R = \frac{s}{\theta}. \tag{2.16}$$

This way we help define the **range of feasible loom pin dimensions given the constraints of the multi-axis printing system**. By adjusting the pin spacing and print bed radius, it is possible to control the minimum and maximum loom configurations that can be printed effectively within the available machine dimensions.

2.4. Building the system

Printer Firmware

The **Duet Wi-Fi** and **Duet X5** controller boards, running with the **RepRap Firmware**, were used to construct the control system for the multi-axis 3D printer. This combination ensures compatibility with **multi-axis toolpath creation** by providing precise motion control for the additional rotating DoFs.

X, Y, and Z linear axes, the **extruder**, and core printer parts like **fans** and **thermistors** (temperature sensors) are all controlled by the Duet Wi-Fi, which acts as the main controller. Two rotational axes (which we will call **U and V**) could be integrated thanks to the addition of the Duet X5 expansion board, which could handle more stepper motor drivers. For a schematic overview refer to Fig: A.1 in Appendix A.

The RepRap Firmware was configured to define the new multi-axis kinematics, enabling synchronized movement across both **translational** and **rotational** axes.

Based on Equations (2.1) and (2.2), taking into account that the stepper motor's pulleys have 20 teeth, the driver pulley for the U axis has 60 teeth, and the driver pulley for the V axis has 40 teeth, the respective steps per degree calculated were $26.\overline{6}$ and $17.\overline{7}$.

Added Rotational Axis Support

As seen, a **TT arrangement**, which implements two additional rotational axes on the print bed, can be used to create a multi-axis fiber weaving system. Because of its **stability**, **simplicity** and **ease of integration** with current FDM printers, this method was selected. The additional axis on the bed provides greater control over rotating movements **without substantially changing the extruder's kinematics**, in contrast to systems that alter the motion of the printhead, adding substantially more complexity to the computational section.

Several open-source designs offer modular solutions for incorporating **two additional rotational axes** using stepper motors and pulley-driven systems. Without the use of intricate robotic arms or inverse kinematics, these configurations enable both axial and circumferential fiber deposition by dynamically adjusting the printing orientation.

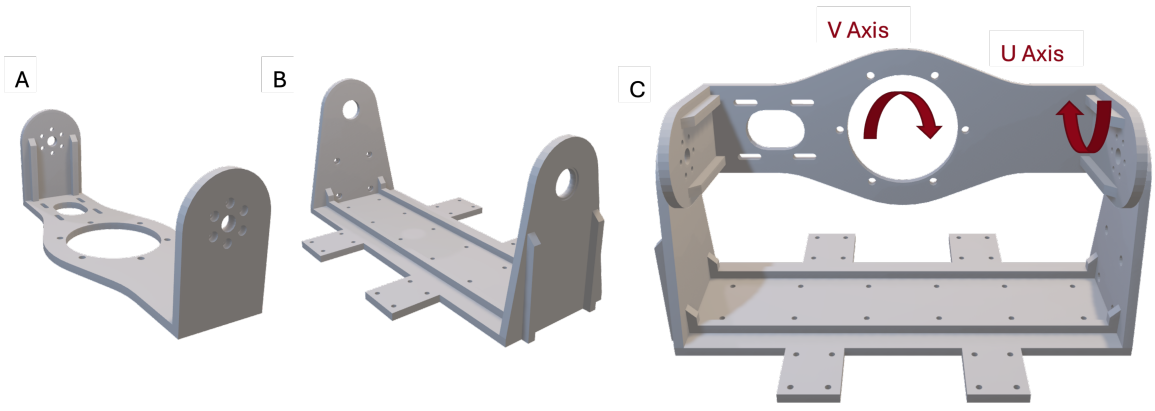

Figure 2.5 Illustration of print bed (A) inner and (B) outer structure and (C) of the 2 added rotational axis

This way we can stably input 2 extra axes, **V and U**, as depicted in Fig. 2.5 (C).

After, a **customized print bed support** is added, depending on the specific application requirements. This modularity ensures that the system can be adapted for different fiber-reinforced structures, such as cylindrical looms or hybrid composite geometries.

Bed Support Modifications

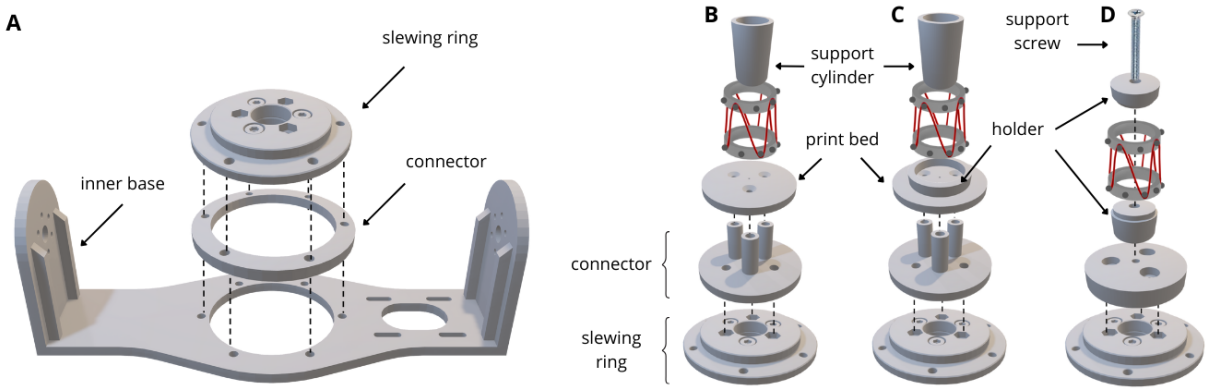

Figure 2.6 Illustration of print bed schematic process: A) Slewing ring to base connection B) First print support design C) Second design with holder incorporation D) Final print support design.

The **slewing ring**, a rotation tool, which is firmly fastened to the inner base of the bed support, allows the V axis to rotate. This configuration ensures controlled rotation throughout the printing process.

First, a **cylindrical support** was set up directly on the print bed plaque, to fit through inside the actual printed loom. Major printing errors were caused by this setup, nevertheless, especially when it came to stability and alignment during multi-axis movements.

A **ring bed holder** was created to solve these problems and maintain the sample's stability. By attaching this holder to the support cylinder, misalignment was decreased and fiber deposition accuracy increased. However, there was still room for improvement even if this change resulted in increased printing quality.

The following design iteration involved **lowering the size** of the **holder support** and changing its location, as a result of previous results and the conclusions shown in Equation (2.5). The holder was inserted via the **inside** of the loom part rather than being fastened externally. To improve stability, the support's total **length was also extended**. A long M5 screw was used to keep all the parts in place, reducing undesired movement and increasing print accuracy. The support cylinder was taken out entirely to further optimize the setup.

Better fiber alignment and overall print quality were ensured by this gradual improvement of the support system, which greatly increased printing process reliability, as will be shown in the Results section.

Nozzle Modifications

Finding a cost-effective way to **increase the nozzle length** was essential to guarantee complete mobility during printing and avoid collisions between the altered parts and the original printer frame (Fig. 2.7 (A)). Clearance was insufficient with a conventional nozzle, especially when the print bed was rotated by $90°$. This led to the conclusion that a minimum nozzle length of 18 mm was necessary.

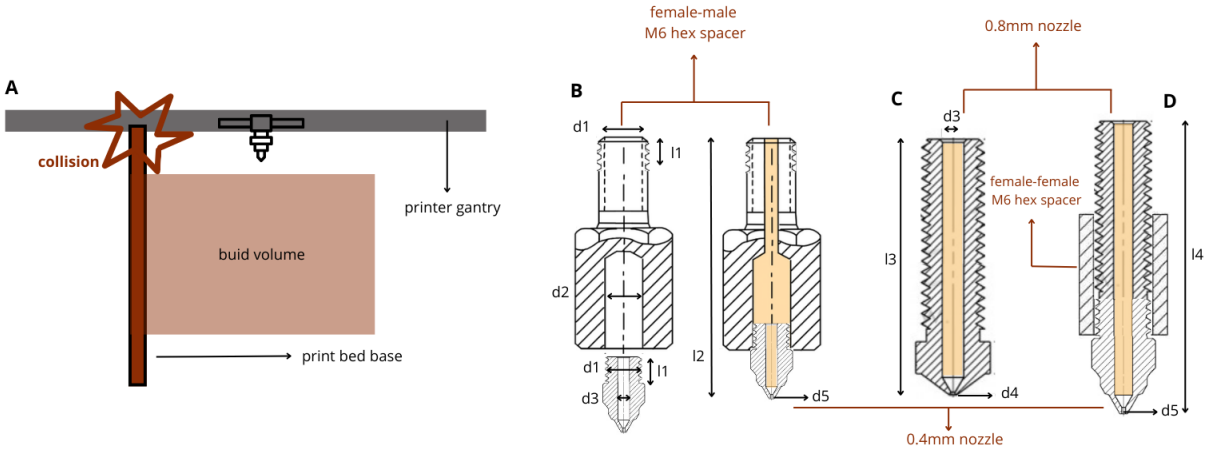

Figure 2.7 Illustration of nozzle modification process process: A) Collision issue in original hot-end assembly B) First Attempt: M6 Hex Spacer Modification C) Second Approach: Extended Nozzle Implementation D) Final Approach: Hybrid Nozzle Design. In orange, is the channel in which the PLA follows through.

First Attempt: M6 Hex Spacer Modification

An **M6 hex spacer** was modified, l_2 of 19.5 mm, in the first attempt, because the diameter of the printer's original nozzle threaded part, d_1, matched its outside diameter, of 5 mm, as well as the threaded lengths, l_1 of 4 mm. To match the nozzle's inner diameter, a hole was drilled through the male-threaded part. But there were two main problems with this strategy:

- **Inner Diameter Mismatch**: The original inner diameter of the hex spacer, d_2 remained significantly larger, 5mm than that of the nozzle d_3, of 1.90 mm, leading to **flow inconsistencies**.
- **Heat Dispersion Problems**: As highlighted in Fig. 1.8, a hot-end consists of a hot zone and a cool zone. The extension of the nozzle length while maintaining the same heater block position led to unwanted heat dispersion. Although **kapton tape** was added for insulation, it was observed that the registered temperature at the heater block was not consistent with the temperature at the nozzle tip. Combined with the increased inner diameter, this resulted in **excessive material deposition** that could not be mitigated even by adjusting retraction settings.

Second Approach: Extended Nozzle Implementation

A commercially available extended nozzle, l_3 of 21 mm, was then tested to meet the size constraints. The minimum nozzle tip diameter, d_4 for the available sizes was 0.8 mm. While this configuration provided some improvements, the **heating inconsistencies** persisted. To address this, a **second heater and thermistor** were introduced at the midsection of the nozzle, and insulation was applied using Kapton tape and silicone glue. However, due to the large nozzle opening of $0.8mm$, rather than d_5 of $0.4mm$ significant inaccuracies in the printing process were observed, making it unsuitable for the precise dimensions required for the loom structure.

Final Approach: Hybrid Nozzle Design

To achieve both temperature stability and accurate extrusion, a hybrid approach, l_4 of 24.5mm, was implemented. The tube section of the 0.8 mm nozzle was cut and fastened with the help of a hex spacer, this time with female-female openings, to the head of a 0.4 mm nozzle, as their inner diameters were identical. Additional modifications included:

- **Insulation**: The hybrid nozzle was insulated with Kapton tape and silicone glue (see Fig. 2.8 (A)) to minimize heat loss.
- **Additional Heating Elements**: A second thermistor and heater block (see Fig. 2.8 (C)) were installed at the midsection to ensure uniform temperature distribution along the extended nozzle.

Figure 2.8 Illustration of nozzle heating and insulation process (A) Application of silicone glue (B) Nozzle extension without adding second heater block (C) Nozzle extension after adding second heater block

This final configuration resulted in **optimal printing accuracy** while maintaining **consistent temperature stability**, as will be seen in the next section, effectively resolving the issues encountered in previous iterations.

Fiber Extrusion Method

According to *Schouten et al.* [63], there are six different categories of multi-material printing techniques, with the **tool-changing method** coming out as preferred for the **continuous fiber** applications in question, embedded in a loom.

Henceforth, we employed a fiber extrusion method inspired by prior work [30], which explored **integrating fiber placement** into a **single-nozzle FDM system** without requiring **additional motors or electronic boards**. Building upon this concept, a custom fiber extrusion tool was developed and adapted to suit the specific requirements of the multi-axis printing setup, as shown in Fig. 2.9.

In contrast to conventional tool-changing mechanisms, which often involve complex docking stations and additional degrees of freedom, this approach streamlines fiber deposition within the existing motion system. The extrusion tool consists of a **guiding needle** to direct the fiber through the loom, a **tensioning mechanism** to regulate fiber placement, and a **secure mounting system**. To ensure seamless integration with the printer's workflow, an anchoring pin was incorporated into the frame, allowing the fiber to be held in place and precisely pulled through the weaving process.

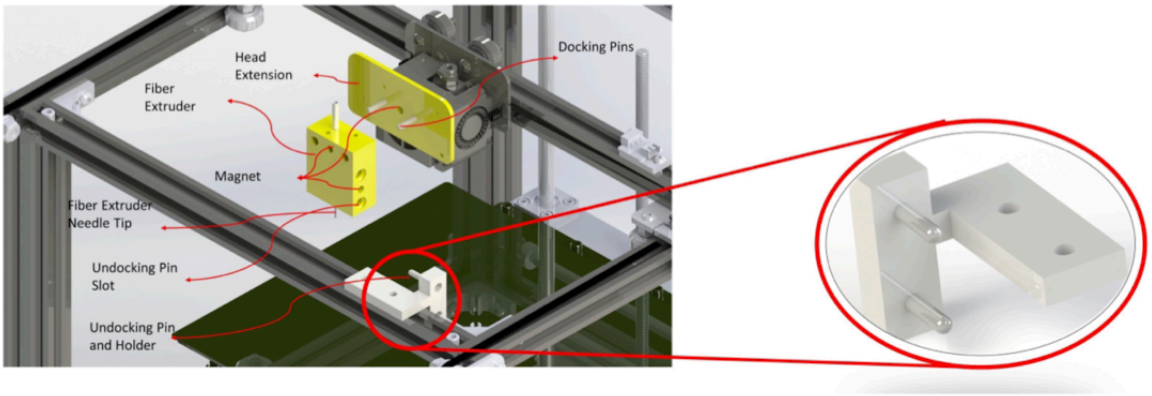

Figure 2.9 Illustration of fiber nozzle modification process process, inspired by [30]

As such, firmware modifications were made to optimize the extrusion system for compatibility with multi-axis motion, using the **RepRap software**, ensuring that fiber placement remains **consistent and stable** throughout the cylindrical weaving process and that the **switching mechanism of the two extruders** can be incorporated within the printing process.

2.5. Software Design

Path Planning Principles

The 3D printing process relies on a **software stack** that converts a 3D model into precise motion and extrusion instructions for the printer. This is achieved through **slicing**, where the model is divided into layers and translated into **Geometric Code (G-code)**, the programming language used for CNC machines and 3D printers.

In Fused Deposition Modeling (FDM), a nozzle deposits molten thermoplastic while following a predetermined toolpath. Each movement is described by **G-code commands**, with the most fundamental being:

```
G1 X10 Y0 E10
```

This moves the printhead **10 units along X** while extruding material (see Fig. 2.10 (A)). Complex shapes are constructed by stringing together multiple **G1 commands**, specifying motion in **X, Y**, **Z** and **extrusion (E)**.

Traditional slicing divides the model into **parallel layers** aligned with the print bed. Each layer consists of **perimeter toolpaths** outlining the shape.

Each toolpath is converted into a sequence of **G1 commands**, with the nozzle following the polyline approximation (Fig. 2.10 (B)). If additional layers are printed on top, the Z-height**G1 commands** increases after each iteration (Fig. 2.10 (C)).

To produce intricate geometries, **polylines** are used—continuous paths defined by a sequence of connected **points** (Fig. 2.10 (D)). These polylines approximate curved surfaces by breaking them into **discrete segments**, with accuracy improving as the number of divisions increases (Fig. 2.10 (E)).

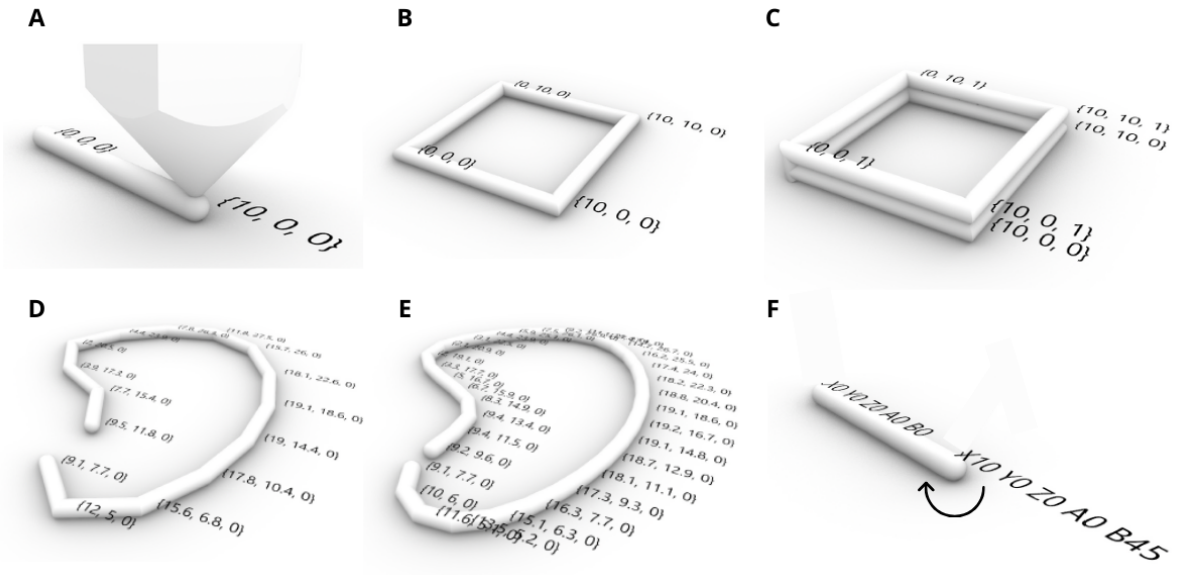

Figure 2.10 (A) Deposition of a single track of material by giving a G-code command. (B) Singular contour defined using X and Y coordinates (C) 3-dimensional shape defined using X, Y, and Z coordinates (D) Contour with rough division of polyline (E) Contour with fine division of polyline (F) Deposition of a single track of material with the change of rotational print bed axis

For **multi-axis printing**, additional **DoFs** must be considered. Unlike planar slicing, **rotational axis U and V** modify the toolpath dynamically to align with the cylindrical geometry of the loom. Instead of only moving in **X, Y, and Z**, the G-code also defines the rotation of the print bed and nozzle orientation.

A **polar coordinates-based approach** determines the toolpath at each point, ensuring correct nozzle alignment for fiber deposition. The G-code is extended to include U and V commands, such as:

```
G1 X10 Y0 Z0 U30 V15 E10
```

where **U and V** define the angular positions needed to optimize fiber placement (Fig. 2.10 (F)).

The algorithm must adjust **U and V rotations** to print out the loom, wrap fibers around the loom with controlled tension and placement, secure the fibers in place, and interchange nozzles throughout the multi-material process.

Due to its smooth integration with digital fabrication tools and parametric design features, *Grasshopper*, a visual programming language in *Rhino 3D*, is frequently used for G-code fabrication. Its node-based programming environment allows users to **specify intricate geometric operations** and **convert them straight into toolpath instructions** for 3D printers and CNC machines. As such, we can mathematically define our structures for both the **pin** (Fig. 2.12 (A)) and **fiber pathway** (Fig. 2.12 (C)) cases, breaking them down into distinct coordinates which we can later compute into the G-code for the machine.

It allows real-time manipulation of parameters such as **layer height**, **extrusion width**, and **movement paths**, enabling greater control over customized G-code generation. For **multi-axis printing**, where exact control over rotational and translational movements is necessary to generate complex geometries, this technique is especially helpful.

Input controlling parameters

The script's first module, **input parameters**, is where the user specifies the geometry to be sliced as well as the slicing parameters. As seen in Fig. 2.11, sliders are used to adjust parameters. These sliders have a default value as well as limitations that correspond to the acceptable range of values anticipated for that parameter. One is then capable of controlling the desired **pin radius** for the loom print, the **pin offset to center** where it specifies the center point of the pin compared to the origin of the system, in accordance to the print bed design, the **number of pins**, which will specify the angle in between different fibers and the **radius of the loom ring**.

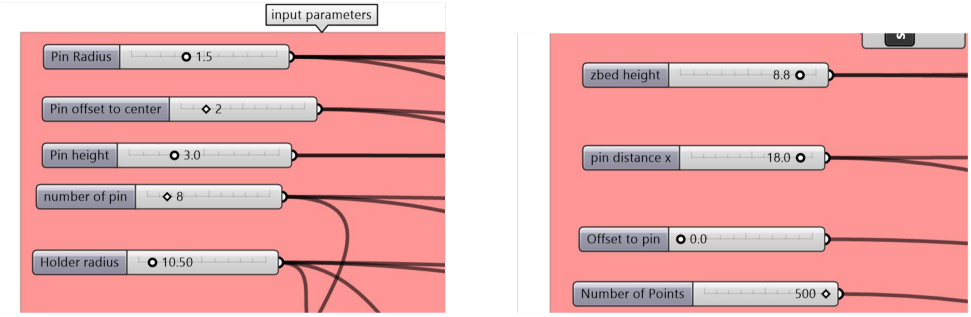

Figure 2.11 Parameters set by the user for each print

Additionally, the **printing starting point for the Z Axis** is also defined, depending on the position of the modified Z-endstop, as well as the **distance in between loom rings** along the X axis, which defines the final structure's height and the angle in between pins. Finally, depending in **how many points the user wishes to break the print into**, in other words, the length of g-code lines, can also be adjusted (see Fig. 2.12 (B)).

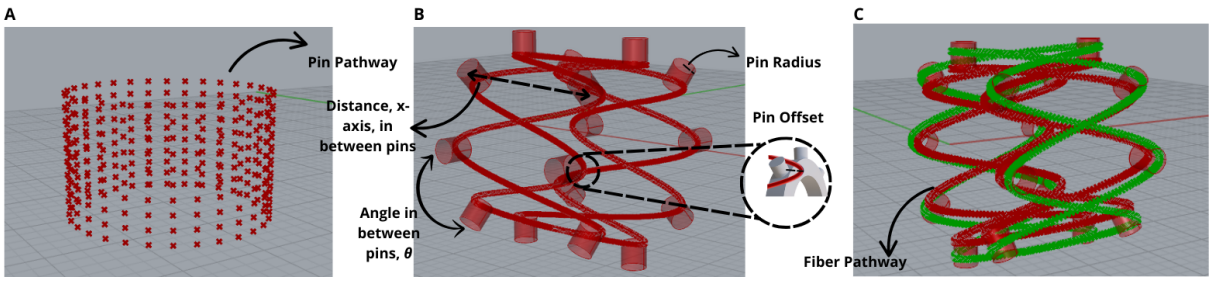

Figure 2.12 Fiber Pathway and Pin Arrangement (A) Visualization of the cylindrical pin layout, showing the spatial distribution of the pin pathway (B) Close-up of the fiber weaving pattern, highlighting the key geometric parameters: pin offset, pin radius, and the angular spacing, θ, between pins. A zoomed-in inset illustrates how the fiber interacts with the pin surface (C) Final fiber structure demonstrating the interwoven fiber pathways, where alternating layers (red and green) create a continuous and structurally integrated fiber arrangement.

These are the controlling parameters for the printing process in question, additionally, the user can also set the standard printing parameters such as **layer thickness**, **filament diameter**, **flow rate** and **printing speed**.

For the remaining processes, the *Grasshopper* iteration is too extensive to showcase in this section, so it will be shown in schematic form, but can nonetheless be consulted in Appendix C.

Loom G-code

To deposit the pins in the loom construction, the first step in the process is to define a **circular base**. The main framework for pin placement is created by extruding this circular profile along its axis to create a three-dimensional **cylinder**. At predetermined intervals along the cylinder's length, **contour lines** are extracted to create reference points for the pin positions. To guarantee consistent pin distribution, these shapes are subsequently separated into **distinct dots**. The produced dots are **flattened** into an organized list and then broken down into their corresponding **X, Y, and Z coordinates** to simplify data management. An example of what this schematic would look like is depicted in Fig. 2.13.

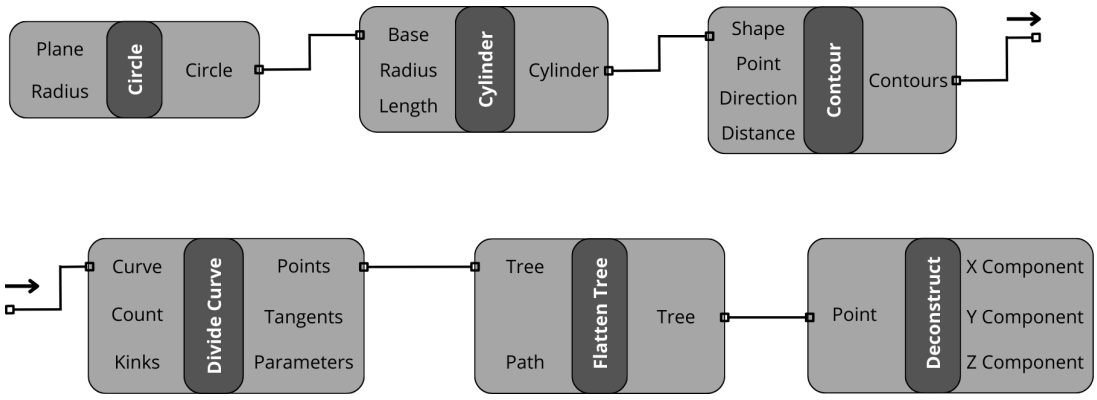

Figure 2.13 Schematic representation of the process for generating loom pin coordinates. A base circular geometry is used to define the cylindrical structure, followed by contour extraction and point division to determine precise pin locations. These coordinates are then deconstructed into individual X, Y, and Z components for further processing.

Afterward, the **coordinate data** is first extracted from the specified cylindrical structure. These coordinates are then organized into different **data blocks** to provide consistency in data handling and each block's **length** is retrieved. These sequences will **repeat** themselves as needed to **match rotational movements based on the specified number of pins**. As such, the V rotational axis values are also structured in blocks and input with the correspondent (X,Y,Z) coordinates. U axis is set to turn to $90°$.

The **extrusion values** are calculated automatically for each line of g-code, based on the **distance**

in between sequential coordinates, **layer thickness**, **filament diameter** and **path width**, in accordance to Equation (2.7). For every movement, a **formatted string** is created that specifies important parameters including feed rate (F600), rotational positions (U, V), extrusion values (E), and Cartesian coordinates (X, Y, Z) to produce **valid G-code commands**.

Fiber Pathway G-code

For **circumferential reinforcement**, this process is implemented in **MATLAB**, where the motion of the **U and V rotational axes** is carefully synchronized with linear movements along the **X-axis** to create the desired fiber trajectory.

To achieve a continuous **circumferential fiber deposition**, the **U-axis is fixed at 90 degrees**, aligning the fiber extrusion path perpendicular to the rotational plane. The **V-axis** is then rotated continuously, controlling the angular displacement of the fiber around the cylindrical substrate. Simultaneously, the **nozzle moves incrementally along the X-axis**, ensuring that each full **360-degree rotation of the V-axis** corresponds to a predefined linear advancement in the X-direction. This incremental shift determines the **helical pitch of the fiber placement**, effectively governing the **fiber density variation along the structure**.

The synchronization between the angular velocity of **V** and the translational velocity along **X** is crucial in defining the **fiber orientation angle**. By varying the **X-axis increment per revolution**, different fiber densities can be achieved, smaller increments lead to a **denser fiber arrangement**, while larger increments result in **wider fiber spacing**.

As for, the **axial fiber reinforcement**, as previously mentioned, the main inspiration point is the orientation of **collagen fibers** in the human **annulus firosus**.

The axial fiber pathway is constructed using a parametric **sinusoidal function**, where the oscillation accounts for the fiber's interaction with the loom pins. The equation for the fiber displacement is defined as:

$$y = A \cdot \sin(w \cdot x + t) + y_0, \tag{2.17}$$

where:

- A represents the **amplitude of the sinusoid**, determined by the spacing between pins in the x-direction, the desired offset to each pin, and the pin radius.
- w is the **angular frequency**, calculated as $w = \frac{2\pi}{P}$, where P is the period of the function, derived from the arc length corresponding to the angular spacing between pins.
- t is a **displacement parameter** that ensures proper alignment of the fiber paths with the pin positions.
- y_0 is the **vertical shift**, incorporating the necessary offset and x-distance to correctly position the sinusoidal wave.

Following the mathematical definition, the x-coordinates for the fiber paths are obtained from the sinusoidal function, while the y-coordinates are generated using a **domain function**. This domain accounts for the starting and ending points of the fiber along the structure, which is determined by the total **circumferential arc distance multiplied by the number of pins**. The domain is then used as an input for a range function, which subdivides the fiber pathway into **discrete points** according to the desired resolution, effectively defining the number of lines in the resulting G-code.

To correctly project the fiber paths onto the cylindrical loom structure, the generated sinusoidal curves are **mirrored**, to ensure overlapping and crossing of fiber layers, and **mapped onto an arc that represents the print surface**. This arc is constructed based on the **radius of the support rings**, ensuring that the fiber pathways conform to the curvature of the cylindrical structure. The transformation of the sinusoidal paths into cylindrical coordinates guarantees that the printed fibers remain in precise alignment with the loom geometry.

Finally, each point is then deconstructed into its respective *x*, *y*, and *z* coordinates using the component `Deconstruct`. The *x*- and *z*-coordinates serve as inputs to a transformation function that determines the rotational angle θ required for fiber intercalation.

The **transformation function** applies an `atan2` operation, ensuring a continuous angle computation. Specifically, when $y < 0$, an offset of 2π is added to prevent discontinuities in the computed angle, avoiding abrupt resets from $360°$ to $0°$. This prevents undesired jumps in fiber orientation, which would otherwise disrupt the intercalating fiber pattern observed in the annulus fibrosus. This way it is possible to **mimic he alternating collagen fiber orientation** in biological tissues (i.e., switching between θ and $-\theta$)

Following the angular computation, the values are passed into a Python script to enforce smooth transitions. Finally, the computed angular and positional values are formatted into G-code commands, by use of a string function.

Fiber Locking Mechanism

To enhance **fiber interlocking** and **structural integrity**, a **conformal surface** printing approach was developed utilizing a structured serpentine motion (Fig. 2.14). This method ensures that **fibers remain in place** during the printing process by coordinating the movement of the translational *x*-axis and the rotational *v*-axis. The printhead remains perpendicular to the print surface, while the *v*-axis adjusts dynamically to accommodate the required angular increments.

The fiber locking mechanism follows a systematic deposition pattern generated via MATLAB-based G-code (see Fig. 2.14):

1. The *v*-axis is incremented every θ degrees, where θ is determined by the number of pins and their angular separation.
2. The printhead moves along the *x*-axis in a structured zigzag pattern, ensuring a continuous locking effect.
3. The motion alternates between (x, v) coordinates:
   $(0,0), (0,40), (1,40), (1,0), (2,0), (2,40), (3,40), (3,0)$, progressively increasing *x* while maintaining fiber entrapment.
4. The controlled incremental movement in *x* allows for gradual advancement along the height of the loom rings while maintaining fiber stability.

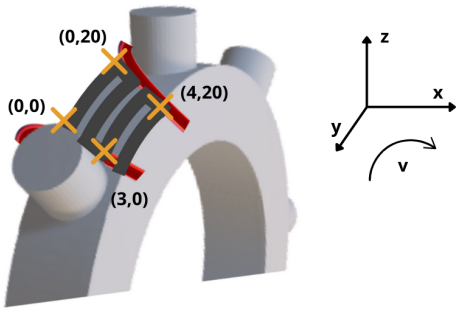

Figure 2.14 Illustration of the fiber locking strategy using a conformal printing approach. The printhead moves in a structured serpentine motion, guided by coordinated x-axis translation and v-axis rotation. The numbered coordinate points represent sequential printing positions, ensuring that fibers remain interlocked with the loom structure. The reference coordinate system highlights the movement along the x- and v-axes.

The extrusion calculations are given by Equation (2.7).

By carefully controlling these parameters, the locking mechanism prevents **fiber displacement during the printing process**. It also allows for the gap in between pins to be fully covered, **recreating the initial ring structure**, and allows for a new layer of printing with the same continuous fiber. As a result it stimulates the **endplates** already seen in the implantable devices.

2.6. Experimental Setups

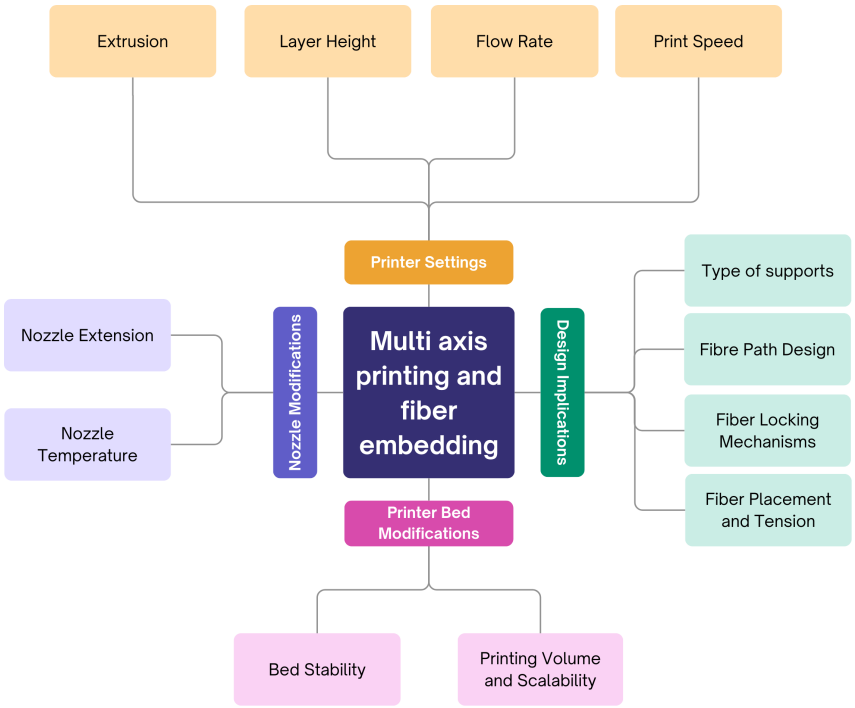

Figure 2.15 Overview of the key factors influencing multi-axis fiber embedding. The experimental setup is structured around four main aspects and their respective influences: Printer Settings, Design Implications, Printer Bed Modifications, and Nozzle Modifications.

The experimental setups were designed to assess the encountered challenges during the development of the multi-axis fiber embedding system and evaluate its performance under different conditions. The analysis is structured around four key aspects: **printer settings**, **design implications**, **printer bed modifications** and **nozzle modifications**. Each of these categories plays a crucial role in determining the feasibility and efficiency of the fiber embedding process.

To systematically evaluate the system, we conducted targeted tests focusing on each of these areas, as seen in Fig. 2.15:

- **Printer Settings:** The influence of extrusion parameters, layer height, flow rate, and print speed on fiber deposition and overall print quality.
- **Nozzle Modifications:** The effects of nozzle extensions and temperature control on fiber deposition accuracy and extrusion consistency.
- **Printer Bed Modifications:** The stability and scalability of the print bed to accommodate multi-axis motion and fiber embedding.
- **Design Implications:** The impact of support structures, fiber pathway optimization and fiber locking mechanisms.

Printer Settings

To quantitatively assess the **accuracy** and **performance** of the developed multi-axis printing system, a series of controlled experiments were conducted under varying process parameters. The objective was to determine the optimal printing conditions that maximize dimensional accuracy. The evaluation process spanned across multiple factors, including **nozzle design**, **flow rate**, **print speed**, and **extrusion rate**.

The three distinct nozzle configurations were tested: he **M6 hex spacer modification**, incorporating an extended path for extrusion, the **extended nozzle implementation**, designed to improve clearance and deposition consistency and the **hybrid nozzle**, a composite configuration combining elements of the previous designs to optimize both extrusion flow and thermal regulation.

The hybrid nozzle was ultimately selected for defining the baseline print settings, as it consistently produced the highest-quality prints. Using this nozzle, a control set of printing parameters was established based on commonly accepted values FDM printing, with deviations introduced at increments of ±10% to ±30% to explore the effect of process variation (±50% for the extrusion cases since smaller increments showed little variance in results).

The experimental methodology followed a systematic approach:

1. **Printing Parameter Evaluation**: The tests were performed by systematically varying key printing parameters:
    - **Flow Rate:** 90%, 100%, and 110% of the standard setting.
    - **Print Speed:** 1000 mm/min, 1200 mm/min, and 1500 mm/min.
    - **Extrusion Factor:** 50%, 100%, and 150%.
2. **Dimensional Accuracy Assessment**: Each print was evaluated using a **digital caliper**, measuring **height**, **width**, and **length**. The obtained values were compared against the theoretical design dimensions using the previously defined accuracy formula in Equation (2.6).
3. **Surface Quality and Structural Integrity Analysis**:
    - **Surface Finish:** Evaluated based on visual inspection to determine smoothness and consistency.
    - **Layer Alignment:** Examined for potential misalignment or deformation in successive layers.
    - **Pin Adherence:** Verified whether the deposited material properly adhered to the loom structure.
4. **Reproducibility and Statistical Validation**: Each test condition was repeated across **eight independent samples** to account for variability, ensuring statistical robustness in the analysis.

Following the identification of optimal parameters using the hybrid nozzle, the same conditions were applied to the previous nozzle designs. This allowed for a direct **comparison of performance**, **quantifying the accuracy losses** and **inconsistencies** associated with each configuration. The comparative analysis aimed to illustrate the extent of improvement achieved through nozzle modifications, validating the necessity of the final hybrid design.

Nozzle modifications

To ensure optimal extrusion and minimize material inconsistencies, an in-depth evaluation of the **thermal performance** and **dimensional accuracy** of different nozzle designs was conducted. Three nozzle configurations were tested: **(1) the M6 hex spacer modification, (2) the extended nozzle implementation, and (3) the hybrid nozzle**, each exhibiting distinct thermal behaviors and flow characteristics.

The primary objective was to **analyze temperature variations** along the nozzle length, assessing their impact on material flow and print quality. Temperature measurements were recorded with a thermal camera (see Fig. 2.16) and plotted across different sections of the nozzle for all three configurations. The results justified the need for **additional heating elements**, particularly in extended nozzles, where heat dissipation led to uneven extrusion. In the first prototype, the **hex spacer modification**, the increased internal diameter due to scaling effects created temperature inconsistencies, which in turn **caused material clogging**—a phenomenon where molten polymer solidifies prematurely inside the nozzle, obstructing flow. Additionally, **oozing** was observed—an over-extrusion effect in which excess material leaks from the nozzle during non-printing movements, leading to surface defects and dimensional inaccuracies, which ultimately motivated the need for such testing.

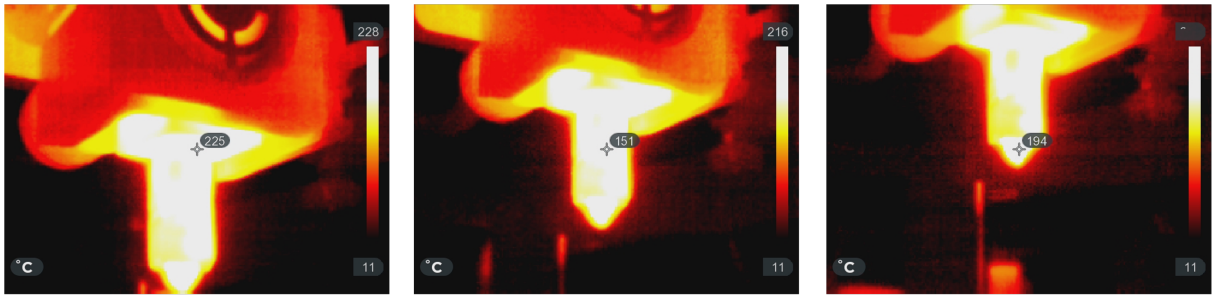

Figure 2.16 Thermal imaging of the modified nozzle at three different measurement points along its length. The first image (left) captures the temperature near the heater block, where heat is most concentrated. The second image (middle) measures the midpoint of the nozzle, revealing a significant drop in temperature due to heat dissipation along the extended extrusion path. The third image (right) shows the temperature at the nozzle tip, highlighting further thermal loss, which can impact extrusion consistency and justify the need for additional heating elements to maintain a stable melt flow.

To quantitatively assess the impact of these thermal variations on **print quality**, the previously described **dimensional accuracy tests** were performed using all three nozzles. This allowed for a direct correlation between thermal regulation and print fidelity, revealing that **unstable temperature distributions** in the initial nozzles led to inconsistencies in extrusion volume and surface quality.

A final critical factor in mitigating over-extrusion and unwanted deposition was **retraction calibration**. Retraction refers to the controlled retraction of the filament within the extruder to counteract oozing, ensuring clean transitions between print paths. The need for computationally optimized **retraction settings** was particularly evident in the first two nozzle designs, where material leakage affected precision. By refining retraction parameters based on observed material behavior, excessive oozing was reduced, improving **surface smoothness and print accuracy**.

Printer Bed Modifications

To ensure precise fiber deposition and mitigate structural inaccuracies during multi-axis printing, modifications to the **printer bed** were implemented and systematically assessed. The evaluation was conducted in two key areas: **bed stability** and **printing volume scalability**, both of which play a critical role in the overall accuracy of fiber embedding.

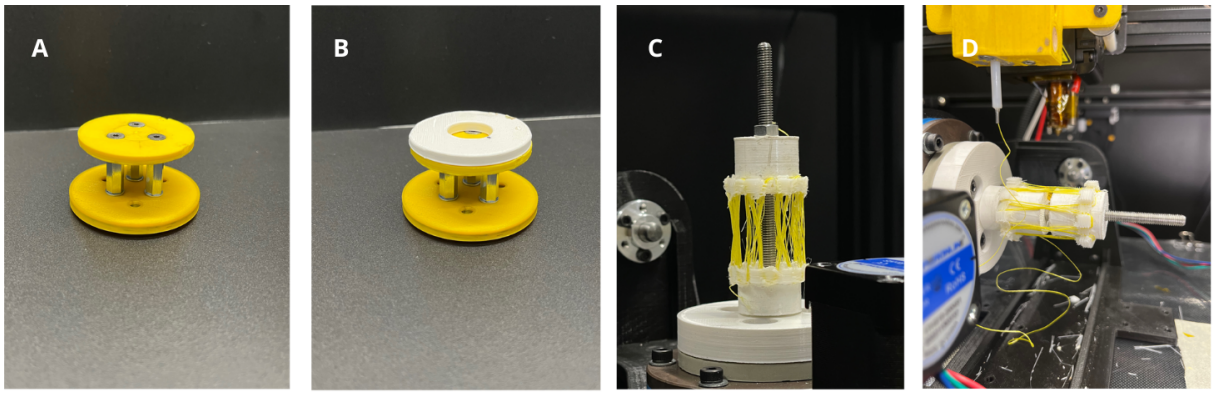

Figure 2.17 Overview of the three print bed configurations developed to enhance fiber deposition accuracy and structural stability. (A) Normal Print Bed Design (B) Intermediate Support Structure (C) Optimized Adjustable Support (D) Implementation of the final support structure in the multi-axis fiber embedding system, ensuring precise fiber alignment and enhanced print repeatability for posterior assessment.

Three distinct print bed configurations were developed and tested (Fig. 2.18):

1. **Normal Print Bed Design:** The first design, where the loom was supported by a cylinder directly onto the print bed, limiting adaptability but providing an initial baseline for comparison.
2. **Intermediate Support Structure:** A design integrating a dedicated holder to secure the loom during the fiber embedding process, reducing unwanted displacements.

3. **Optimized Adjustable Support:** A refined design featuring an extended support structure with an increased vertical length and a **reduced lower ring clearance**, ensuring greater stability while accommodating larger-scale prints.

The accuracy of **fiber placement** and **pin stacking alignment** was systematically analyzed across these three configurations, during a normal printing process. To quantify deviations, **image-based analysis** was performed using **ImageJ**, an image processing tool for precise displacement measurements.

The analysis of **fiber displacement** focused on the deviation of embedded fibers from their intended positions relative to the pin bases.

In parallel, **pin stacking offset** was evaluated, addressing deviations arising from multiple factors: **print-induced inaccuracies**, **fiber-induced tension**, and **bed instability**.

Moreover, the necessary calculations to assess the necessary printing volume and minimum printing requirements for the loom, based on equations (2.3), (2.4) and (2.15) were also performed.

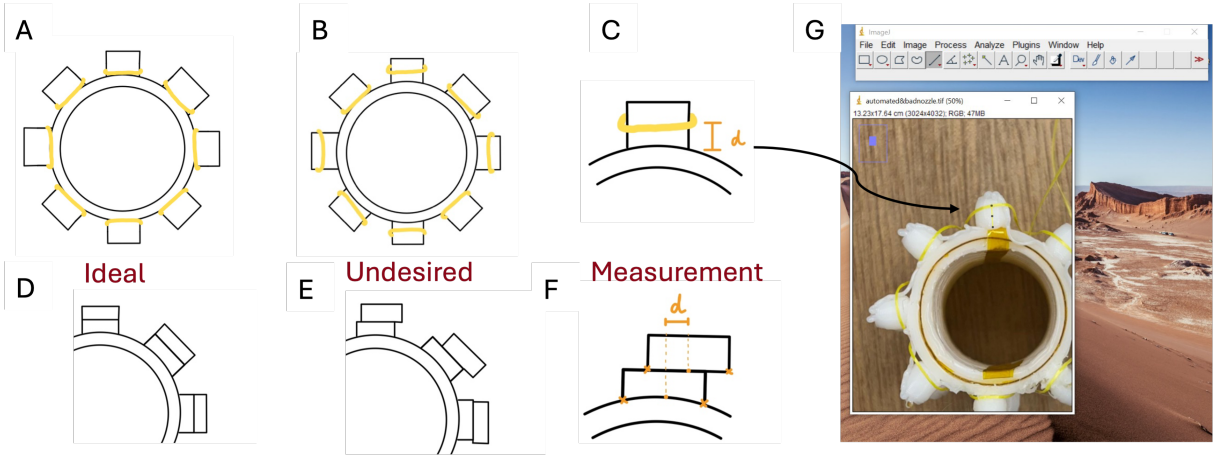

Figure 2.18 Evaluation of fiber placement accuracy and pin stacking offset. (A) Ideal fiber placement where fibers rest at the base of each pin. (B) Undesired misalignment was observed in certain prints. (C) Schematic representation of fiber deviation measurement. (D-E) Side view of ideal and undesired pin stacking. (F) Measurement of pin stacking offset d. (G) ImageJ software is used for quantifying fiber displacement and structural deviations in printed samples.

Design Implications

The structural integrity and performance of the developed multi-axis fiber embedding system were evaluated through four key design considerations: **type of supports**, **fiber path design**, **fiber locking mechanisms**, and **fiber placement and tension**. These factors directly influenced the mechanical stability of the printed structures, the adhesion of fibers to the substrate, and the overall feasibility of the system for scalable and reliable fiber-reinforced fabrication.

- **Pin Structural Integrity and Fiber-Induced Deflection**

During the printing process, fiber tension induces a **capstan effect**, applying shear forces onto the pins that may lead to deflection or structural failure. Ensuring **high bending stiffness** and a **sufficient breaking point** under fiber-induced loads was critical in maintaining the integrity of the loom. To quantify the mechanical resilience of different pin designs, tensile tests were performed using a **universal testing machine** (Instron 3343, Instron, USA).

Each test sample was secured onto the Instron support while a fiber was threaded through a pin, which was also fixed to the machine. A controlled tensile extension was applied, with a maximum load of 200 N, corresponding to the fiber's breaking point and the load cell limitation of the system. The loading rate was set at **0.02 N per second** to progressively evaluate the **deflection and failure characteristics** of each pin design. This approach enabled an assessment of the mechanical limitations of different pin geometries in response to fiber-induced stress.

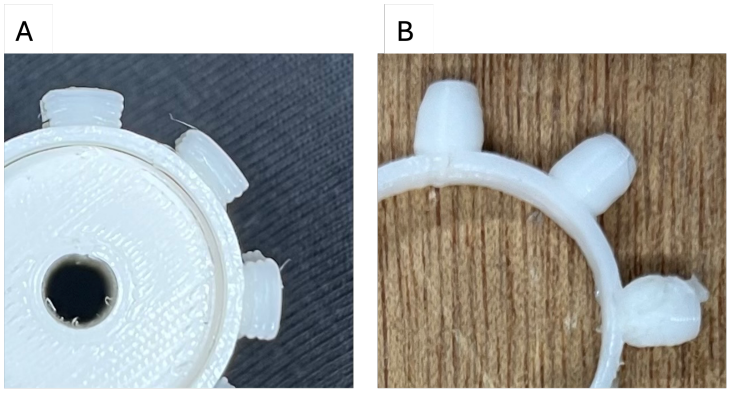

Figure 2.19 Different Achievable Pins (A) Through conformal slicing techniques (B) Cylindrical Standard Pins

In addition to assessing the conventional circular pin arrangement, the study explored the feasibility of applying a **conformal slicing mechanism** to pin-loom fiber embedding. Preliminary tests indicated that **conformal slicing pins** exhibited greater **structural stability** than traditional circular pins, reducing the likelihood of deformation under load. This insight motivated further testing to compare the **mechanical response** of both designs under controlled loading conditions.

While conformal slicing demonstrated advantages in mechanical stability, it also required significantly longer printing times compared to conventional circular pins. To address this limitation, an alternative method was explored: the application of **adhesive bonding** to the support rings prior to fiber embedding. By pre-applying this, the study aimed to determine whether this approach could enhance adhesion and mitigate pin displacement, offering a potential trade-off between **print efficiency and mechanical robustness**.

- **Influence of Pin Spacing on Applied Tensile Force**

The effect of **pin spacing** on the applied tensile force was evaluated to determine how variations in the angular separation between pins influence the overall mechanical response of the system. This assessment was conducted based on Equation (2.13), which establishes the relationship between the total applied force F_{total} and the force experienced per pin F_{pin}

To experimentally validate this relationship, a **tensile test** was performed to assess how changes in the pin angle (i.e., the spacing between consecutive pins) affect the **maximum reaction force in the vertical direction**. The test setup involved applying a controlled displacement of **1.5 mm**—a constrained value reflecting the limited deformability of axially reinforced fiber structures—at a loading rate of **0.02 mm per second**.

The test was repeated for different numbers of pins, thus altering the angular spacing and evaluating its influence on the resulting mechanical behavior. The **maximum vertical reaction force**, which represents the resistance exerted by the fiber system against deformation, was recorded for each configuration.

- **Impact of Fiber Density and Pin Arrangement on Structural Stiffness**

To evaluate the **influence of fiber density and pin arrangement** on the **structural stiffness** and **rotational torque** of the fabricated samples, five distinct specimens were produced and subsequently cast in **Ecoflex 10**, a compliant silicone-based matrix material. The casting ensured that all samples shared a standardized **length of 35 mm** and **diameter of 26 mm**, allowing for direct comparative analysis.

The primary variable in this study was the **pin spacing**, which dictated the angular separation of fiber reinforcements within the cylindrical matrix. The following configurations were tested:

- **4-pin configuration:** Pins positioned at 90° intervals.
- **6-pin configuration:** Pins positioned at 60° intervals.

- **8-pin configuration:** Pins positioned at 45° intervals.

Additionally, to assess the role of **fiber density** on structural stiffness, two variations of the **8-pin configuration** were fabricated:

- One sample reinforced with **three layers** of fiber.
- One sample reinforced with **six layers** of fiber.

To isolate the contribution of fiber reinforcement to mechanical properties, a control specimen consisting of **only the matrix material** (Ecoflex 10, without fiber reinforcement) was also cast. This sample served as a baseline reference to quantify the structural enhancements introduced by fiber integration.

To comprehensively evaluate the **mechanical response** of the fiber-reinforced structures, two distinct experimental setups were implemented.

First, a **torsional torque test** was conducted by implementing additional support to the Instron testing system, ensuring that the composite samples remained **horizontally oriented**. One end of the sample was **fixed**, while the other was subjected to a **rotational force** via a fiber attached to a **pulley system**. The inclusion of the pulley defined a **torque radius of 10.50 mm**. The applied **rotation was set to a maximum Instron extension of 5.5 mm**, allowing for the measurement of the output load, which was subsequently used to compute the torque response of the samples.

Additionally, **compression/extension load cycles** were performed to analyze the **stress-strain behavior** of the different fiber orientations. Each sample underwent **cyclic deformation up to 28.5% strain**, ensuring a comprehensive characterization of their mechanical performance under repeated loading conditions. This test aimed to define the stiffness behavior across multiple load cycles and capture the influence of fiber arrangement on the composite's hysteresis response.

- **Effectiveness of Extrusion Calculations for Fiber Locking**

The effectiveness of the fiber locking mechanism was assessed by evaluating whether the **extrusion volume** was appropriately calibrated to secure the fibers in place while avoiding excessive material deposition that could interfere with the **loom structure** or **support integrity**.

The extrusion parameters were defined based on prior **calculations of material volume**, ensuring that the deposited filament formed a secure bond around the fibers. This assessment involved verifying:

- **Fiber Retention:** Evaluating whether the fibers remained firmly secured in their designated positions throughout the printing process.
- **Excessive Material Deposition:** Determining whether an overestimation in extrusion led to unwanted accumulation, which could **impinge on the pins** or alter the **loom structure integrity**.

The evaluation was conducted through **direct observation**, assessing whether fiber displacement occurred post-printing. If fibers exhibited any noticeable shifts, the extrusion parameters were recalibrated to achieve a balance between sufficient **adhesion** and minimal **structural interference**.

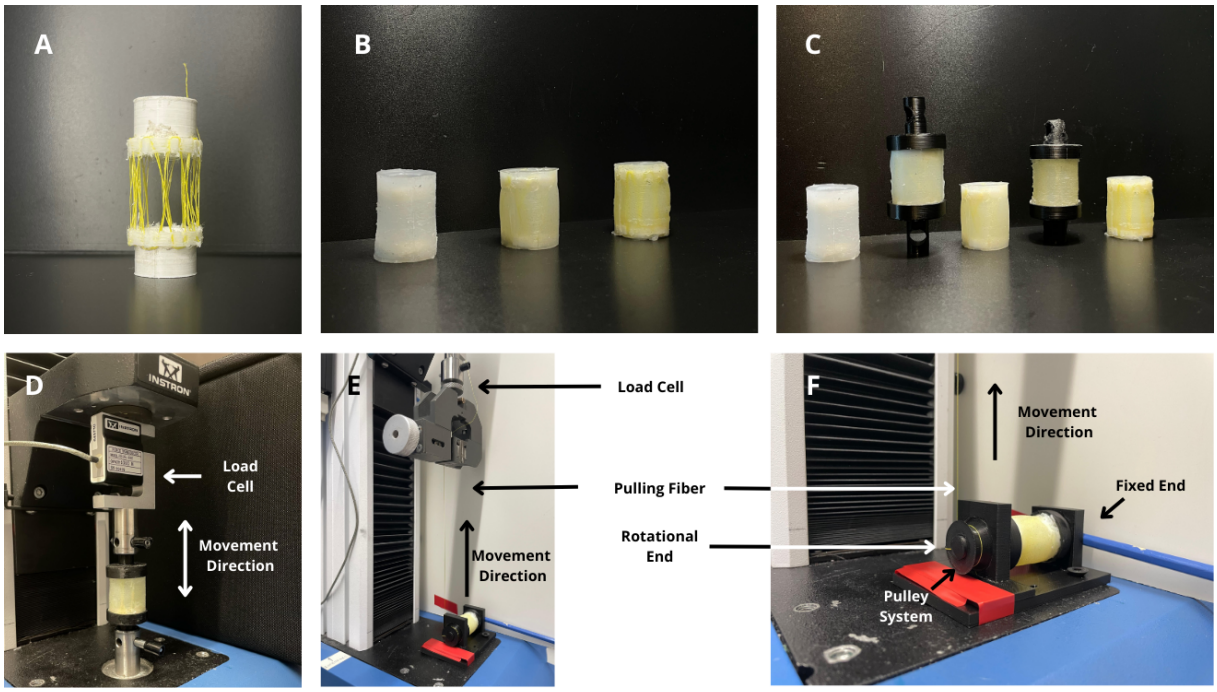

Figure 2.20 Experimental setup and sample preparation for fiber-reinforced structures. (A) Printed fiber-reinforced cylindrical structure before casting. (B) Different cast samples show variations in fiber density, including a control sample without fibers. (C) Final samples mounted for mechanical testing, assessing the impact of fiber reinforcement on structural stiffness. From left to right: control sample, 3 fiber layers and 4 pins, 3 fiber layers and 6 pins, 3 fiber layers and 8 pins, 6 fiber layers and 8 pins. (D) Testing setup for evaluating the structural stiffness of the cast samples through compression/extension load cycles. (E) Rotational torque testing setup for evaluating fiber-induced forces using the Instron testing machine. (F) Close-up to rotational torque testing setup and pulley system.

3

Results & Analysis

3.1. System Performance and Fabrication Outcomes

To validate the effectiveness of the developed multi-axis fiber embedding system, the fabricated structures and printing outcomes were assessed against the predefined design requirements in Chapter 2. This refers to advancements in **multi-axis motion capability**, **extrusion and fiber deposition**, **custom toolpath generation**, **scalability**, and **integrated control and automation**.

Multi-Axis Motion and Printer Configuration

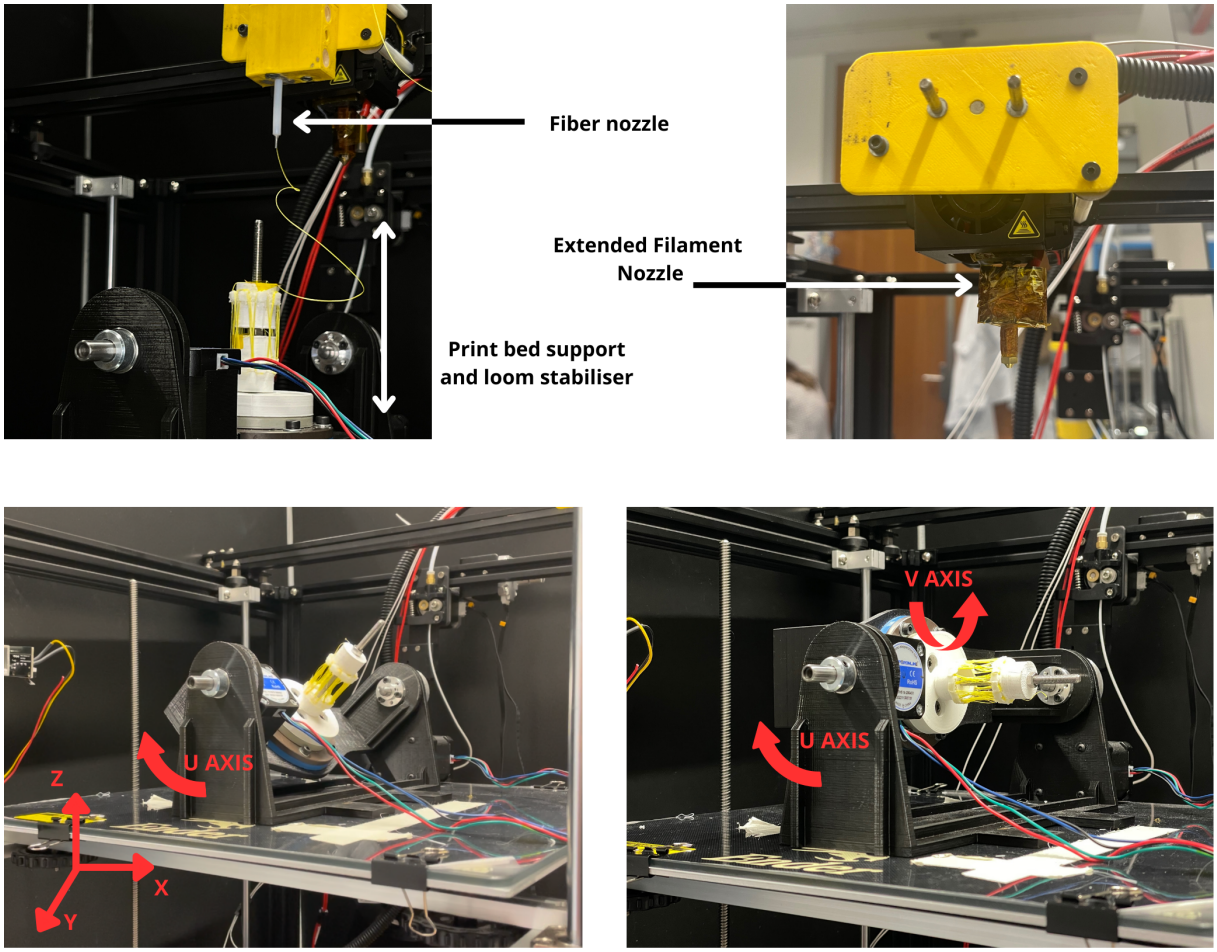

Figure 3.1 Illustration of the added rotational & translational axes enabling multi-axis motion and overview of the modified printer, including the extended nozzle and adapted print bed.

The system successfully integrates both rotational and translational motion to enable non-planar

fiber deposition. The added rotational axes allow for precise control of fiber paths, ensuring proper fiber alignment in both axial and circumferential directions. Fig. 3.1 illustrates the degrees of freedom introduced by the modified motion system, highlighting the additional axes incorporated for enhanced flexibility in fiber embedding.

A comprehensive overview of the modified printer setup is provided in Fig. 3.1, showcasing the implementation of the **extended nozzle**, the **adjusted print bed**, and the overall machine configuration. These modifications directly contribute to improved clearance, controlled extrusion, and adaptable fiber placement strategies.

Printing Orientation and Layering Variability

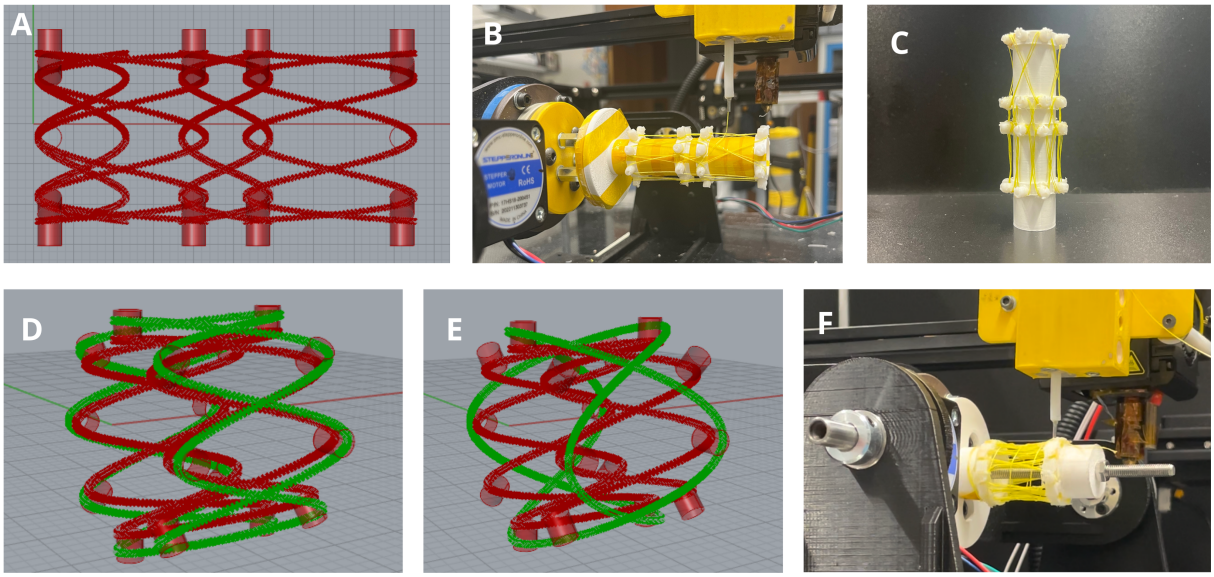

Figure 3.2 Demonstration of Printing Achievable Variability (A) Multi-angle orientation of fiber across the same layer of print. (B) Printing process of multi-angle orientation fibers (C) Achievable multi-angle oriented fiber structure. (D) Deposition of fibers across multiple layers (E) Variance of fiber angle orientation across multiple layers (F) Simultaneous Print of circumferential and Axial fibers

The system demonstrates the capability to vary printing orientation both **within a single layer** and **across multiple layers**, as depicted in Fig. 3.3 (A-E). This flexibility enables the fabrication of **complex fiber architectures**, allowing seamless transitions between different deposition angles while maintaining structural integrity.

To further illustrate the achieved fiber alignment strategies, Fig. 3.3 (F) presents the printed structures incorporating both **axial** and **circumferential** fiber pathways. This capability is critical in ensuring that fibers follow mechanically advantageous trajectories, optimizing load distribution and material efficiency.

The following subsections delve into the quantitative analysis of the system's performance in terms of **dimensional accuracy**, **fiber adherence**, and **mechanical integrity**, providing a detailed examination of the results obtained from experimental testing.

3.2. Printer Settings

Multi-Axis Motion and Printer Configuration

To evaluate the impact of **extrusion thickness**, **flow rate**, and **print speed** on print accuracy, a series of tests were conducted. The error rate was computed using the accuracy formula defined previously (Equation (2.6)), where **negative values indicate over-extrusion**, while **positive values correspond to under-extrusion**. The results were plotted as a function of the number of pins in the

structure. For the extrusion cases, the results can be seen in Fig. 3.3, as for flow rate and speed plots, refer to Appendix B.

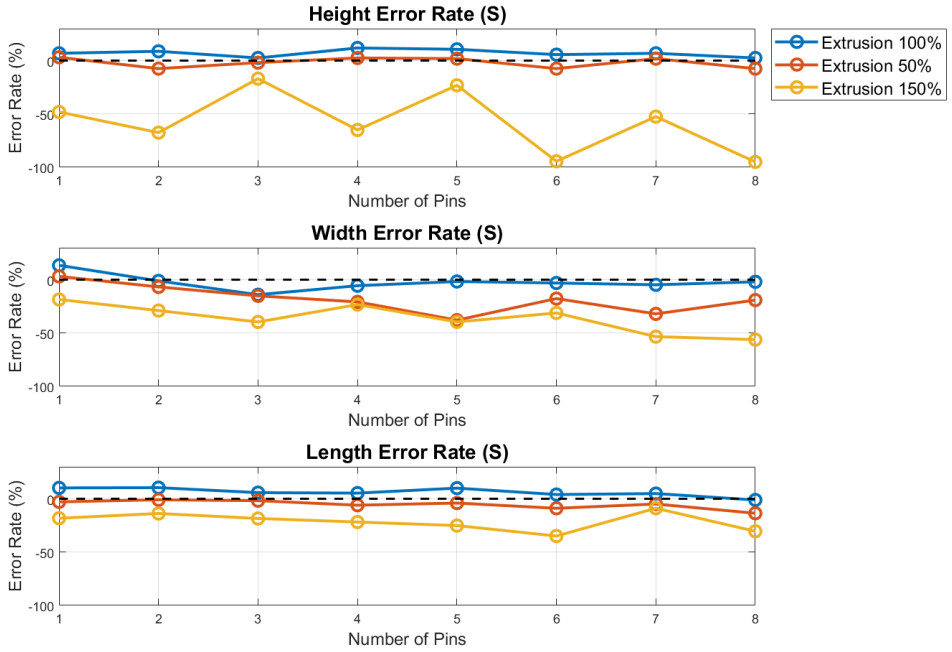

Figure 3.3 Error rate analysis for different extrusion thicknesses (E50%, E100%, and E150%) in a loom print with 8 pins. The plots show the variation in accuracy across height (Z-axis), width (V-axis), and length (X-axis). Negative error values indicate over-extrusion, while positive values correspond to under-extrusion, as defined by the accuracy equation (Equation (2.6)). The results highlight that an extrusion thickness of E100% provides the most stable accuracy across all axes.

Table 3.1: Linear Regression Models for Error Rates Across Printing Parameters

Parameter	Height Error Formula	Width Error Formula	Length Error Formula
Extrusion Thickness (mm)			
E50%	$y = -0.379x + 8.661$	$y = -1.067x + 2.448$	$y = -1.283x + 11.968$
E100% (Calculated)	$y = -0.536x + 0.536$	$y = -3.648x - 1.876$	$y = -1.357x + 0.746$
E150%	$y = -5.283x - 34.040$	$y = -4.484x - 16.162$	$y = -1.354x - 15.349$
Flow Rate (%)			
95%	$y = -0.796x + 1.786$	$y = -1.950x - 7.063$	$y = -0.489x - 3.770$
100% (Standard)	$y = -4.442x + 20.848$	$y = 0.271x - 29.695$	$y = -0.476x - 5.857$
105%	$y = -6.257x - 9.576$	$y = -2.505x - 18.118$	$y = -0.119x - 12.548$
Print Speed (mm/s)			
10 mm/s	$y = -0.260x + 8.594$	$y = 1.311x - 8.076$	$y = -0.952x + 10.230$
15 mm/s (Standard)	$y = -1.310x - 4.576$	$y = -3.909x + 1.475$	$y = -2.032x + 1.476$
20 mm/s	$y = 1.570x - 16.362$	$y = -5.922x + 0.281$	$y = -1.082x - 4.659$

Surface Quality and Layer Adhesion Analysis

Beyond dimensional accuracy, the qualitative assessment considered **surface smoothness**, **layer alignment**, and **fiber adhesion** to the loom structure. The results for each printing condition are summarized below.

Parameter	Avg. Surface Quality	Layer Alignment (%)	Adhered Pins	Not Adhered Pins
Extrusion Thickness (mm)				
E50%	3.875	100	7	1
E100% (Calculated)	4.5	100	7	1
E150%	2.875	75	6	2
Flow Rate (%)				
95%	4.75	100	8	0
100% (Standard)	4.875	100	8	0
105%	4.5	37.5	8	0
Print Speed (mm/s)				
10 mm/s	4.625	100	8	0
15 mm/s (Standard)	4.75	100	7	1
20 mm/s	4.625	50	4	4

Table 3.2: Qualitative Analysis Summary for Extrusion Thickness, Flow Rate, and Print Speed

The plotted error rates (Fig. 3.3) illustrate the effect of varying **extrusion thickness** on **height (z-axis)**, **width (v-axis)**, and **length (x-axis) accuracy**. The analysis is based on a loom print with **8 pins**, ensuring a consistent structure across all tested cases.

Height Accuracy (Z-Axis): The results indicate that **extrusion E50%** maintains a relatively stable trend, with error values close to the zero-reference line, suggesting that it provides consistent layer height deposition. The **extrusion E100%**, which corresponds to the calculated optimal value, exhibits an even more stable accuracy profile. However, **extrusion E150%** introduces significant fluctuations, with large negative values indicating **over-extrusion**, leading to material accumulation that disrupts layer stacking. The same can be observed for the flow rate and speed cases.

Width Accuracy (V-Axis): The width error rate follows a downward trend, which suggests a dependency on the **rotational alignment of the v-axis**. Both **extrusion E50% and E100%** maintain relatively small deviations, with **extrusion E100%** confirming its alignment with theoretical predictions. However, **extrusion E150%** significantly deviates downward, indicating **severe over-extrusion**, which likely results in excess material spilling beyond the intended extrusion path. The same can be observed for the flow rate and speed cases.

Length Accuracy (X-Axis): The length error rate remains the most stable across all tested conditions, suggesting that errors along the **x-axis** are primarily affected by the motion system rather than extrusion thickness. The **extrusion E50% and E100%** exhibit nearly identical trends, while **extrusion E150%** shows a slight but consistent downward shift, indicative of minor material accumulation. The same can be observed for the flow rate and speed cases.

Analysis of Regression Models (Table 3.1)

The regression models (Table 3.1) provide insights into how **extrusion thickness, flow rate, and print speed** influence print accuracy across height, width, and length.

For **extrusion thickness**, increasing from **E50% to E150%** led to more pronounced errors, particularly in height and width accuracy. The **steep negative slope of -5.283x** in the height error for **E150%** suggests significant over-extrusion, disrupting layer stacking. Width errors also increased substantially, confirming that excessive material deposition compromises dimensional stability. In contrast, **E100%** maintained the most stable error trends, aligning with theoretical predictions.

For **flow rate**, deviations from the standard **100%** setting negatively impacted accuracy. At **105%**, the large negative slopes in height and width errors ($-6.257x$ and $-2.505x$) indicate severe over-extrusion, leading to layer misalignment. Conversely, reducing the flow rate to **95%** mitigated these effects but introduced minor under-extrusion, seen in the **positive width error slope (0.271x)**.

For **print speed**, increasing beyond **15 mm/s** caused a noticeable decline in accuracy. The **steep width error slope (-5.922x) at 20 mm/s** suggests that higher speeds reduce layer bonding time,

resulting in misalignment. Height accuracy also became inconsistent, highlighting the trade-off between print speed and structural integrity.

These findings confirm that an **optimized balance** of extrusion, flow rate, and speed is required to achieve accurate and stable fiber-reinforced structures. The results validate that maintaining **E100% extrusion thickness, 95-100% flow rate, and 15 mm/s print speed** ensures the best accuracy while minimizing defects.

Qualitative Analysis Discussion (Table 3.2)

Beyond dimensional accuracy, the qualitative analysis provides insight into **surface smoothness, layer alignment, and fiber adhesion**. The results show that **extrusion E100%** achieves the highest **surface quality (4.5)** and **100% layer alignment**, confirming that it is the most reliable setting. In contrast, **extrusion E150%** suffers from significant misalignment (75%), resulting in the lowest **surface quality (2.875)** due to excessive material deposition.

Flow rate adjustments further impact the print's structural integrity. At **105% flow rate**, layer misalignment drops drastically to **37.5%**, reinforcing that excessive flow leads to **irregular deposition and reduced print stability**. Similarly, increasing print speed beyond **15 mm/s** results in poor layer adhesion, with the **20 mm/s case** reducing alignment to **50%**, demonstrating that **higher speeds hinder proper material bonding**.

Final Discussion and Conclusions

The results indicate that an **extrusion thickness of E100%** is the optimal setting, minimizing error rates in height, width, and length while also ensuring the highest **surface quality and layer adhesion**. Over-extrusion (E150%) and excessive flow rates (105%) severely **disrupt layer stacking and introduce defects**, while reducing flow rate to 100% slightly improves surface quality but still risks over-extrusion.

Print speeds above 15 mm/s negatively impact layer adhesion, suggesting that maintaining the **standard print speed of 15 mm/s** and a **flow rate of 100%** ensures the most stable structure.

3.3. Nozzle Modifications

Thermal Performance of Nozzle Modifications

The **set extrusion temperature was 210°C**, ensuring that the filament remains fully melted as it passes through the nozzle. However, the heat transfer efficiency and thermal gradient across the nozzle depend on multiple factors, including the **material**, **internal diameter**, and overall **length of the extrusion system**.

From a theoretical standpoint, a nozzle consists of three key thermal zones, as discussed in Chapter 1: the **cool zone**, the uppermost section where the filament is still solid, the hot zone where heat is transferred to the filament, allowing it to transition from solid to a semi-molten state and the **melt Zone**, the final segment before extrusion, where the filament is fully melted and ready for deposition.

In a standard nozzle, the transition from the cool zone to the hot zone is gradual, ensuring proper material softening. However, in extended nozzles, an increase in internal volume creates an enlarged **melt zone**, which can cause excess material accumulation and fluctuations in filament flow.

Temperature Distribution Across Modified Nozzles

To evaluate how heat propagates through different extended nozzles, temperature measurements were taken along 8 segments (with 0 being the closest to the heater that connects to the cold zone of the nozzle and 8 the segment closest to the extrusion point) of three configurations.

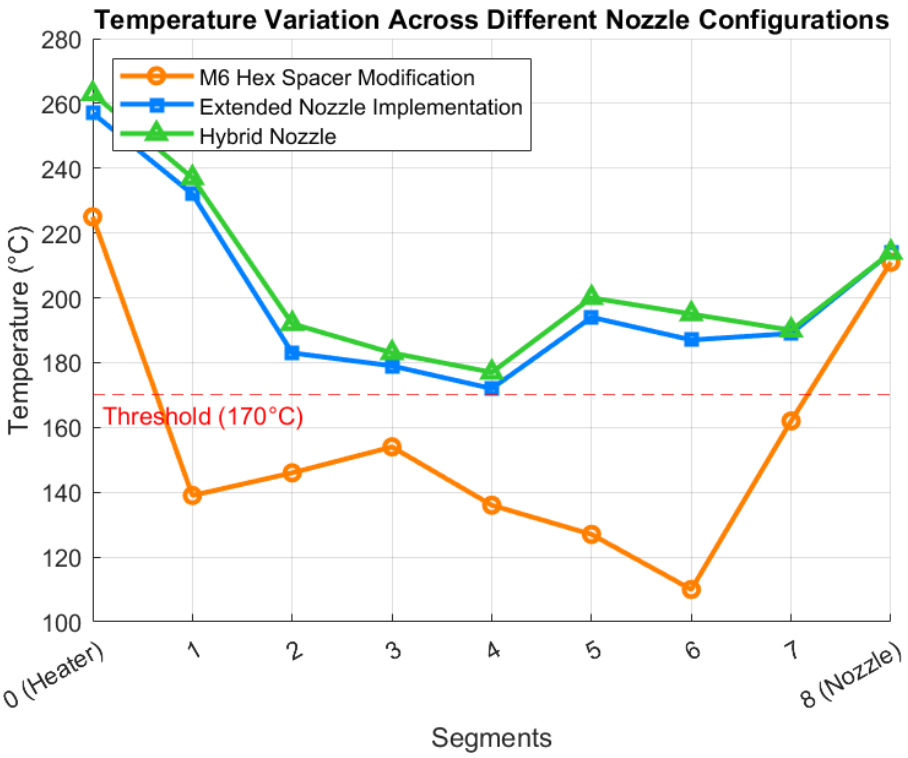

Figure 3.4: Temperature distribution across different nozzle configurations and in different nozzle segments. The M6 hex spacer modification exhibits a drastic heat loss along its extended length, whereas the hybrid nozzle maintains a stable thermal profile above the critical melting threshold.

The results in Fig. 3.4 show that the **M6 hex spacer modification** experienced a sharp temperature drop after the first segment, reducing the temperature below the **170°C critical threshold**, the PLA melting point, across several regions. This cooling effect occurred due to the increased length and lack of additional heat sources to compensate for conductive losses. Despite this drop, the final segment of the nozzle reached a temperature close to the set **210°C**, suggesting that the material exiting the nozzle was still sufficiently heated. However, the extended cold region resulted in **severe clogging and oozing**, particularly due to the increased internal diameter, which allowed molten material to accumulate before extrusion. These issues motivated the need for an additional heater block to sustain consistent temperatures.

In contrast, both the **Extended Nozzle Implementation** and **Hybrid Nozzle** exhibited improved thermal retention, maintaining temperatures above the **critical threshold** across most segments, as a result of adding a second heater block in the middle of the length, that as we see from Fig. 3.4 **picked up the temperatures**. The hybrid nozzle provided the most stable temperature profile, preventing premature cooling while avoiding excessive heat buildup that could cause oozing.

As a first approach to mitigate extrusion irregularities, **retraction settings were implemented** in the G-code to control material flow in sections with major nozzle shifts. Whereas the **Hybrid Nozzle** exhibited a moderate response to retraction, requiring values between **E-0.1 to E-1**, which successfully reduced oozing and stringing between movements, the same could not be said for the **M6 Hex Spacer Nozzle**. It showed persistent material leakage, even when retraction values were increased up to **E-2**, indicating that the excessive internal volume caused delayed filament retraction, making oozing unavoidable.

Implications for Printing Performance

Based on the thermal results and retraction settings, both the **Extended Nozzle Implementation** and **Hybrid Nozzle** appeared to be viable options for multi-axis printing. However, during actual printing trials, significant extrusion discrepancies were observed, particularly with the **0.8 mm nozzle**.

These deviations required a formal accuracy analysis to quantify the extent of dimensional errors and assess the viability of these nozzle modifications.

Accuracy of the 0.8 mm Nozzle

To evaluate the extrusion accuracy of the 0.8 mm nozzle, an error rate analysis was conducted under **standard printing conditions**. The results, shown in Fig. 3.5, reveal significant deviations compared to previously tested configurations.

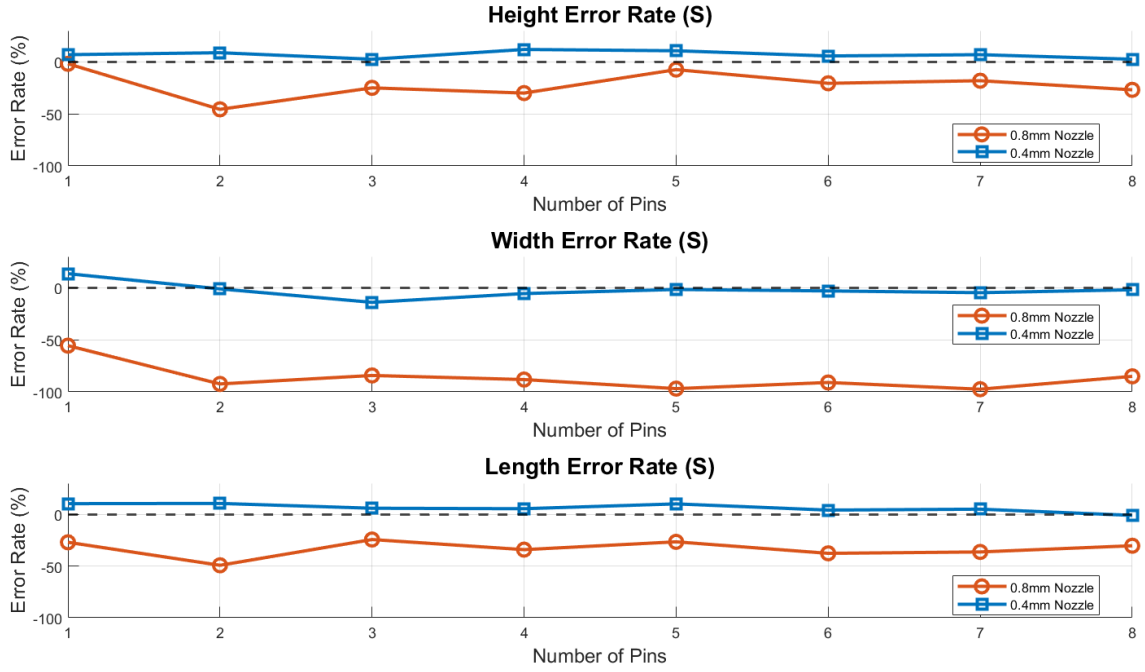

Figure 3.5: Accuracy analysis of the 0.8 mm nozzle under standard printing conditions, compared to the 0.4 mm nozzle. The results indicate extreme over-extrusion, particularly in the width and length dimensions, leading to poor feature definition.

The error rate analysis highlights a consistent trend of **severe over-extrusion**, particularly in the **width and length dimensions**. The width error rate showed extreme deviations, exceeding **-100% in multiple regions**, indicating excessive filament deposition beyond the expected feature boundaries. Similarly, the length dimension exhibited persistent negative error rates, reflecting excess material accumulation. Interestingly, the **height error rate remained relatively stable**, with smaller deviations compared to width and length. Looking into the results, it is visibly shown how, despite its good thermal management, the **0.8 mm extended nozzle** also does not prove to be a viable option.

3.4. Print Bed Modifications

To improve fiber embedding accuracy, three distinct print bed designs were tested:

1. **First Print Bed Support**: The initial design placed the loom directly on the print bed without additional structural support, leading to significant fiber displacement.
2. **Intermediate Print Bed Support**: This modification introduced a dedicated holder to stabilize the loom, reducing misalignment during fiber embedding.
3. **Final Print Bed Support**: A refined structure with extended vertical support and reduced lower ring clearance, ensuring high positional accuracy and repeatability.

The fiber deviation length and pin stacking offset were systematically analyzed for each configuration. For the fiber deviation length from its desired position within the printing loom, it was also interesting to assess how the proposed system could compare to a **manual approach**. As such the

v-axis value was incremented at a slow speed, F250, or approximately 4.2 mm/s, and the fibers were warped around the loom pins.

For the **fiber deviation length**, three samples were produced per support method and the manual case, each with 8 pins for the fiber to pull through. Whereas for the **pin stacking offset** one sample was tested per print bed modification, each with 8 loom pins as well, printed on top of a previous loom support with 8 base pins. The deviations, *d* were assessed for each case as depicted in Fig. 2.18 (C, F and G).

Fiber Deviation from Desired Position

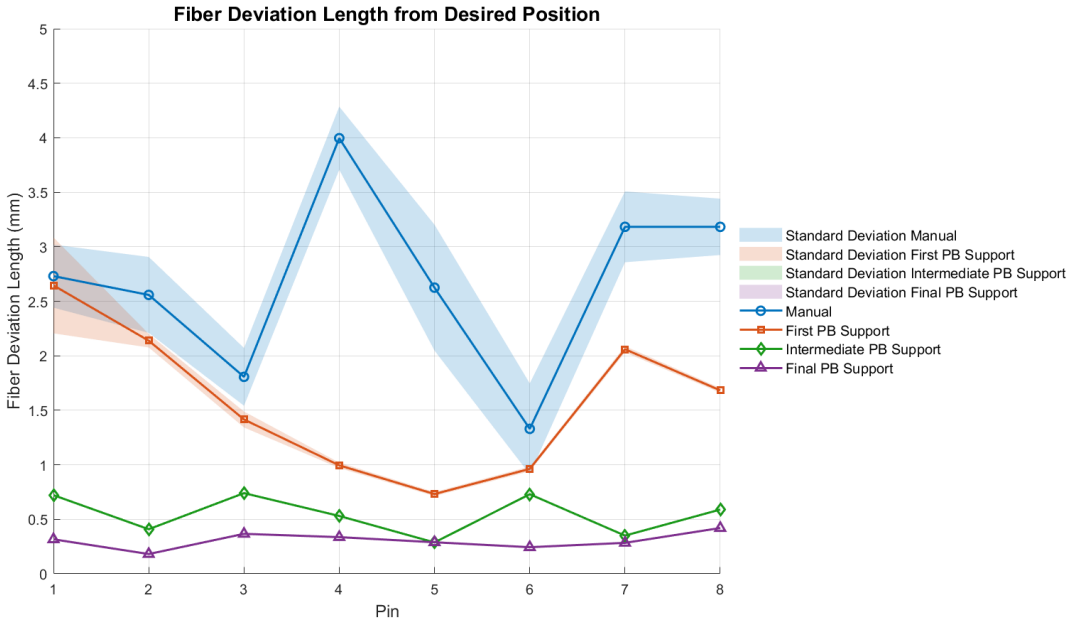

Figure 3.6 Fiber deviation length from the desired position across 8 pins for each print bed configuration. The shaded regions indicate standard deviation, highlighting print repeatability.

The fiber deviation results indicate that **manual fiber embedding results in the highest positional inaccuracies**, with deviations reaching up to 4 mm. The variation of said deviations across the same print also suggests poor accuracy in consistent fiber placement. Furthermore, the standard deviation is also the largest for this condition, suggesting poor repeatability between different prints. The lack of structural constraints in manual embedding results in significant misalignment between layers of deposited fiber, as theoretically proposed.

The **First Print Bed Support** significantly reduces fiber deviation, as shown by the downward shift in deviation values. However, the standard deviation remains relatively high, indicating inconsistencies across prints. Furthermore, the deviations across pins in the same print are still rather undesirable. This suggests that while the support structure improved fiber alignment from manual cases, **external factors such as bed instability still affected print accuracy**.

The **Intermediate Print Bed Support** further reduces deviation length, averaging below 1 mm, with a notably lower standard deviation, as it is almost unnoticeable by the visual assessment of the plots. The improved stabilization mechanism reduces the influence of external disturbances, enhancing repeatability. The variations across the same print are still slightly noticeable, leaving room for improvement in the next iteration design.

The **Final Print Bed Support** achieves the best results, with fiber deviations below 0.5 mm and **exceptionally low standard deviation values**, demonstrating high repeatability. This confirms that structural improvements in print bed design **directly contribute to enhanced fiber placement accuracy and consistency across multiple prints**. Moreover, the results for the same print present

very slight variations ensuring repeatability not only across prints but also for **all the pins in the same structure as well**.

Pin Stacking Offset Analysis

Pin stacking offset analysis further highlights the importance of **print bed stabilization**. The results demonstrate that deviations increase **with the number of stacked layers**, particularly for unstable print bed configurations.

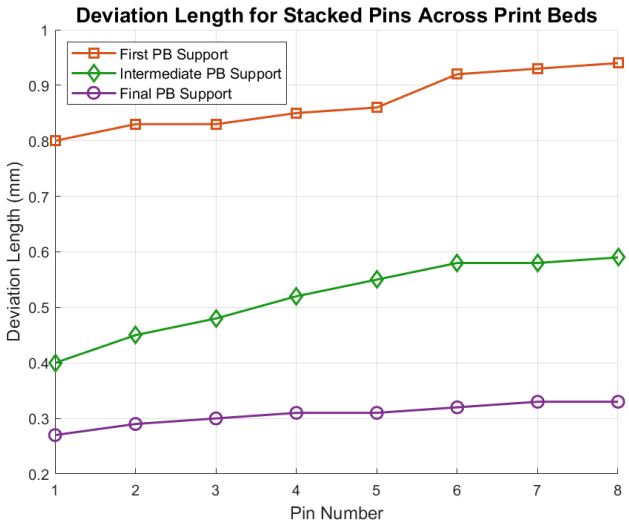

Figure 3.7 Pin stacking offset deviations across 8 pin positions for each print bed configuration.

The **First Print Bed Support** shows the highest pin stacking offset, exceeding 0.9 mm at later pins. This suggests that the lack of stabilization leads to gradual misalignment over multiple stacked layers.

The **Intermediate Print Bed Support** significantly improves stacking alignment, with deviations remaining below 0.6 mm. The results indicate that additional support reduces but does not fully eliminate print-induced inaccuracies.

The **Final Print Bed Support** minimizes stacking offset, maintaining deviations below E150% across all pin positions. The near-linear trend suggests **a high degree of uniformity and alignment accuracy**, validating the effectiveness of the final support structure.

Print Bed Modifications and Volume Constraints

The transition from a conventional Cartesian coordinate system to a **table-table (TT) configuration** in the Ender 5 Plus printer significantly impacts the **effective build volume**. Unlike stationary print beds, the rotating nature of the TT setup introduces **clearance constraints**, reducing the usable printing area. As seen in Table 3.3, while the **original build volume is 49,000 cm^3**, the constraints imposed by rotation reduce the effective print volume to **21,465 cm^3**, resulting in a **16.84% reduction**.

To maximize the available space within these constraints, the print bed height support was optimized to **80 mm**. This allows for the **simultaneous printing of multiple fiber-reinforced structures**, as seen in Figure 3.2C, ensuring efficient use of the limited volume. The **outer print bed structure**, as designed in Figure 2.5B, maintains a length of **2340 mm**, ensuring compatibility with the TT-modified Ender 5 Plus.

Loom Pin Dimensions

For effective stiffness testing, loom structures were designed with **fiber angles of 90° (4 pins), 60° (6 pins), and 45° (8 pins)**. These angles were selected as **distinct values** to provide variation

Table 3.3: Print Bed Volume Constraints

Configuration % Reduction	l (mm)	w (mm)	h (mm)	V_{build} (cm^3)	$V_{reduced}$ (cm^3)
TT (Ender 5 Plus) 16.84%	350	350	400	49,000	21,465

while maintaining reasonable print times.

To ensure **printability**, the **minimum feasible pin radius is 1.5 mm**, which accommodates a **0.4 mm thermoplastic material nozzle** and allows for structural integrity during printing. Additionally, a **2 mm clearance** was implemented with the offset to pin parameter in Grasshopper. This is due to the diameter of the fiber nozzle of 2 mm and added size discrepancies between the printed and designed loom.

The **fiber amplitude chosen was 35 mm**, to **simplify stiffness evaluations** post-printing. However, for accurate biological modeling, the annulus fibrosus goes to a minimum height of **8 mm**, so we also tested up to minimum amplitude values of **5 mm** to prove scalability.

Considering biological references, **the annulus fibrosus**, which consists of circumferential fibers spaced at **25° intervals (12 pins)**, would require a **minimum loom bed radius of 11.46 mm** to accommodate this spacing. By comparison, the **minimum loom radius for the 45° configuration (8 pins) is 6.37 mm**. These calculations ensure that the loom supports can be printed within the reduced TT volume while maintaining biomechanical relevance. So a radius of **11.5mm** was selected for the stiffness sample tests to account for all future possibilities of increasing the number of pins. For further requirements details, refer to Appendix B.

3.5. Design Implications

Pin Structural Integrity Under Fiber-Induced Loads

To evaluate the mechanical integrity of the loom pins under fiber-induced stresses, tensile tests were conducted using a **universal testing machine** (Instron 3343, Instron, USA). The goal of these tests was to determine the breaking force of different pin designs when subjected to fiber-induced loads. Three distinct configurations were tested:

- **Standard Circular Pins:** Traditional cylindrical pins are used as a baseline.
- **Conformal Slicing Pins:** Pins manufactured with an alternative slicing strategy to improve strength.
- **Circular Pins with Adhesive Bonding:** Standard circular pins reinforced with adhesive bonding before fiber embedding.

Quantitative Results

The breaking force values recorded for each sample are summarized in Table 3.4. The mean and standard deviation (**Mean** $\pm$ **SD**) for each pin configuration are also reported to illustrate the variability in mechanical performance.

Table 3.4: Breaking force of different pin configurations under fiber-induced loads.

Pin Type	Sample 1	Sample 2	Sample 3	Mean $\pm$ SD (N)
Standard Circular Pins	12.60	21.59	16.18	**16.79** $\pm$ **4.55**
Conformal Slicing Pins	67.59	59.35	47.06	**57.99** $\pm$ **10.36**
Circular Pins with Adhesive Bonding	81.81	99.48	101.84	**94.38** $\pm$ **10.61**

From the results, it is evident that **standard circular pins** exhibited the lowest structural integrity, with an average breaking force of **16.79 N**. This suggests that traditional pin designs may be more susceptible to failure when subjected to fiber-induced loads.

On the other hand, **conformal slicing pins** demonstrated a significant improvement, with an average breaking force of **57.99 N**, more than three times higher than the standard pins. This suggests that the conformal slicing approach enhances mechanical resilience by optimizing material distribution and increasing structural stability.

The highest strength was observed in the **circular pins with adhesive bonding**, which reached an average breaking force of **94.38 N**. This indicates that adhesive reinforcement plays a crucial role in increasing pin stability, potentially offering a balance between print efficiency and mechanical robustness.

The results suggest that while conformal slicing significantly improves mechanical strength, adhesive bonding provides an alternative solution that maximizes stability with quicker printing processes.

Influence of Pin Spacing on Applied Tensile Force

To validate the relationship described in Equation (2.13) experimentally, a tensile test was performed to assess **how changes in the pin angle** (i.e., spacing between consecutive pins) affected the **maximum reaction force in the vertical direction**, as previously mentioned. As such, a fiber was weaved through **multiple pin configurations (2, 4, 6, and 8 pins)** to evaluate the relationship between pin spacing and reaction force.

The maximum vertical reaction force, representing the **fiber system's resistance to deformation**, was recorded for each configuration.

The recorded forces for each configuration are summarized in Table 3.5. The results demonstrate the influence of increasing pin count (i.e., decreasing angular spacing) on the maximum vertical force.

Table 3.5: Maximum reaction force recorded for different pin spacing configurations.

Number of Pins	Angular Spacing (°)	Max. Force (N)
2	180°	2.289
4	90°	6.398
6	60°	8.943
8	45°	13.338

The experimental results confirm that **increasing the number of pins leads to a higher total reaction force**. The observed trend aligns with the expected mechanical behavior, where the **total force is distributed across multiple pins**, reducing the individual load per pin while increasing the overall fiber tension resistance.

- **Lower Pin Counts (2-4 pins, 180°-90° spacing)**: The reaction force remains relatively low, indicating higher load concentration per pin and greater susceptibility to deformation.
- **Higher Pin Counts (6-8 pins, 60°-45° spacing)**: The reaction force significantly increases, demonstrating enhanced resistance to deformation as load distribution improves.

This trend is particularly relevant to the **stiffness and torque assessments** conducted in this study, as configurations with smaller pin angles not only distribute force more efficiently but also contribute to a **stiffer fiber architecture**. The increased structural resistance observed in denser pin arrangements suggests that **optimizing pin density** in fiber-reinforced designs could be a key factor in enhancing the mechanical integrity of multi-axis printed structures.

Impact of Fiber Density and Pin Arrangement on Structural Stiffness and Rotational Torque

To evaluate the **influence of fiber density and pin arrangement** on the **structural stiffness** and **rotational torque** of the fabricated samples, five distinct specimens were produced and subsequently cast in **Ecoflex 10**.

A **torsional torque test** was conducted by implementing additional support to the Instron testing system, ensuring that the composite samples remained **horizontally oriented**. One end of the

sample was **fixed**, while the other was subjected to a **rotational force** via a fiber attached to a **pulley system**. The inclusion of the pulley defined a **torque radius of 10.50 mm**. The applied **rotation was set to a maximum Instron extension of 5.5 mm**, allowing for the measurement of the output load, which was subsequently used to compute the torque response of the samples.

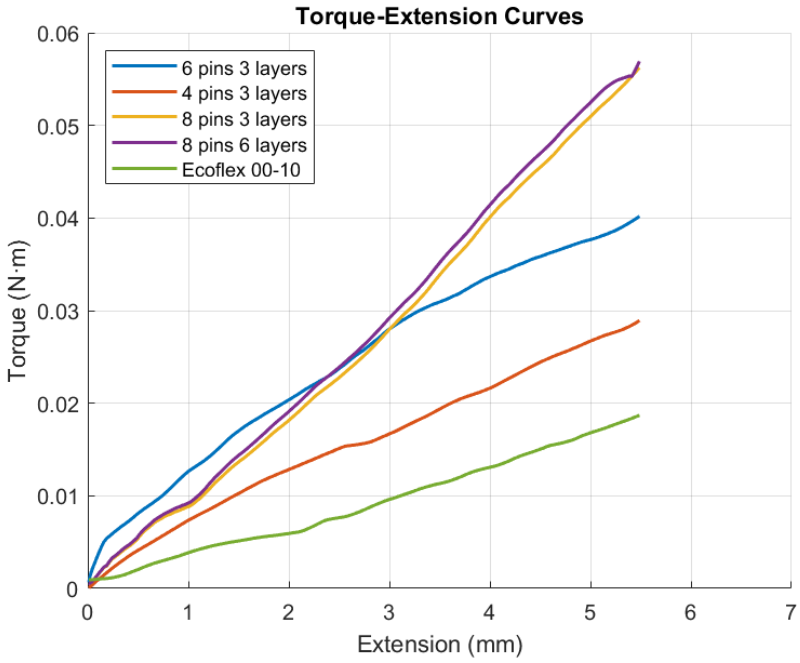

Figure 3.8: Torque-extension curves for different pin configurations and fiber densities.

Table 3.6: Maximum Torque Recorded for Each Sample

Sample Configuration	Maximum Torque (N·m)
Ecoflex 00-10 (Control)	0.019
4 pins, 3 layers	0.029
6 pins, 3 layers	0.040
8 pins, 3 layers	0.056
8 pins, 6 layers	0.057

The results in Fig. 3.8 and Table 3.6 indicate that increasing the **number of pins** follows a clear pattern of increasing **torque resistance** while increasing the **fiber layers** does not yield the same proportional improvement. This behavior can be directly related to the **fiber path constraints**, the **force per pin distribution**, and the **fiber volume fraction** as described in the governing equations.

The total woven fiber length across the structure is governed by Equation (2.10), where the fiber follows an arc between pins. As the **number of pins increases**, the fibers experience shorter free spans between pins, reducing their ability to stretch and deform. This leads to a **higher torque resistance**, as seen in the increase from **4 pins (0.029 N·m) to 6 pins (0.040 N·m) and further to 8 pins (0.056 N·m).**

In contrast, when the **fiber layer count doubles (from 3 to 6 layers in the 8-pin configuration)**, the torque only marginally increases **(from 0.056 N·m to 0.057 N·m).** This suggests that additional fiber layering does not proportionally increase mechanical resistance, likely due to **saturation of fiber-matrix interactions and the limited role of additional layers in torque transmission.**

Additionally, **compression/extension load cycles** were performed to analyze the **stress-strain behavior** of the different fiber orientations. Each sample underwent **cyclic deformation up to 28.5%**

strain, ensuring a comprehensive characterization of their mechanical performance under repeated loading conditions. This test aimed to define the stiffness behavior across multiple load cycles and capture the influence of fiber arrangement on the composite's hysteresis response. To simplify result interpretation, the **8-pin 6-layer sample was excluded from this assessment**, as its deformation response in the torque-extension test indicated minimal variation from the 8-pin 3-layer case.

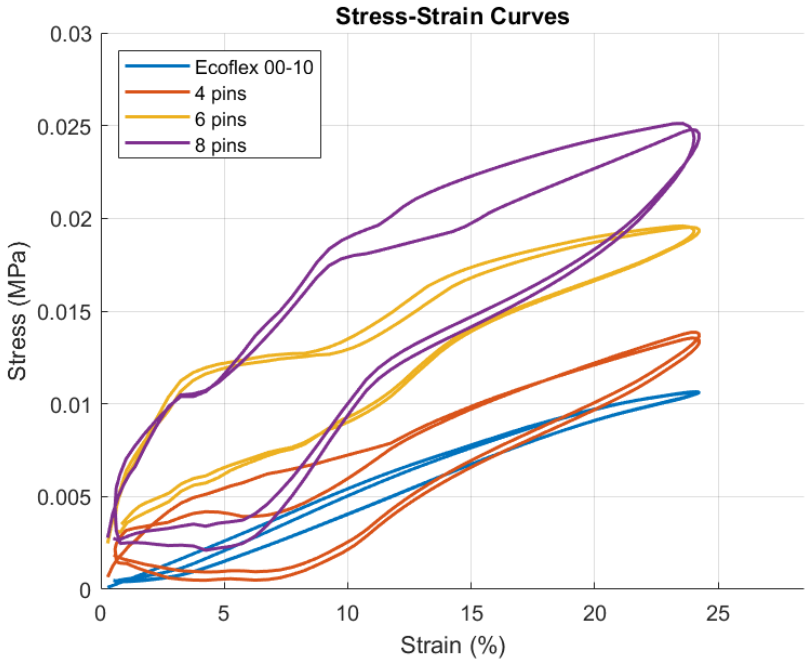

Figure 3.9: Stress-strain curves of fiber-reinforced cylindrical samples with varying pin arrangements and fiber densities.

The stress-strain curves presented in Fig. 3.9 highlight the mechanical response of the FRS under cyclic loading. The recorded stiffness values, summarized in Table 3.7, indicate that increasing the number of reinforcement points leads to a **progressive increase in stiffness**. The 8-pin configuration exhibited the highest stiffness (96.87 kPa), aligning with the trend observed in the torque-extension tests, where additional fiber anchoring points enhance resistance to deformation.

Table 3.7: Secant Stiffness and Hysteresis Energy for Each Sample

Sample	Secant Stiffness (kPa)	Hysteresis Energy (J)
Ecoflex 00-10	44.10	370.43
4 pins	54.52	1435.16
6 pins	72.05	1665.98
8 pins	96.87	3165.89

For clarity, stiffness is reported as the **secant stiffness**, which is derived from the slope of the stress-strain curve between the initial and final deformation points. This metric provides a global measure of resistance to deformation across the loading cycle, effectively capturing the influence of fiber reinforcement, rather than the tangent stiffness, more sensitive to noise.

Additionally, the **hysteresis energy** was quantified to assess the **energy dissipation** during cyclic loading. The 8-pin configuration demonstrated the highest hysteresis energy (3165.89 J), confirming that increased fiber anchoring results in greater energy absorption. This behavior is indicative of enhanced damping properties, a crucial characteristic in applications requiring **shock absorption and mechanical resilience**.

Analysis of Extrusion for Fiber Locking

To prevent fiber displacement during the printing process, an extrusion parameter (**E-value**) was calibrated to lock the fibers securely without over-depositing material, which could interfere with the loom structure. Initial tests were conducted at **100%** of the calculated extrusion volume, but this led to excess material accumulation, affecting both **pin integrity** and the **structural cohesion** of the loom. The results of varying extrusion values are presented in Table 3.8.

Table 3.8: Effect of Extrusion Parameter on Fiber Locking and Structural Stability

Extrusion Parameter (E)	Observation	Result
100%	Overextrusion, structural interference	Not feasible
70%	Secure fiber locking, no structural risk	Optimal
50%	Insufficient extrusion, fibers loosened	Not feasible

The optimal extrusion value was determined to be **70%** of the original calculated value, as it ensured proper fiber retention without excessive deposition. At **50%**, fibers loosened due to inadequate material coverage, while **100%** led to excessive accumulation that compromised the integrity of both the pins and the loom support.

4

Discussion

4.1. Overview of Findings

By the original design specifications, the **multi-axis fiber embedding system** effectively exhibited its capacity to create **fiber-reinforced cylindrical constructions** with **accurate fiber placement** and **regulated mechanical properties**. By introducing rotating degrees of freedom into a standard FDM printer, **multi-axis motion** features were integrated, allowing for both **axial** and **circumferential** fiber deposition. This modification guaranteed scalable fiber orientations inside cylindrical geometries and addressed the drawbacks of planar fiber reinforcement.

Fibre and filament materials could be handled simultaneously thanks to the creation of a **dual extrusion and fibre deposition system**. **Extending the nozzle** assembly prevented undesired interference between the printer gantry and the bed structure while maintaining accurate printing results. V**ariable fiber orientations and densities across several layers** were made possible by this system as a result of the **unique toolpath generation approach**, done using MATLAB and Grasshopper.

The printed loom methodology successfully fulfilled the **scalability and structural compatibility** requirement by enabling fiber placement onto stackable pins, allowing the system to accommodate **variations in fiber density and deposition strategy**. The integration of real-time process automation and control mechanisms ensured that tension variations and positioning errors were dynamically compensated for, optimizing fiber placement accuracy.

The system's ability to generate reliable, load-bearing **fiber structures** while addressing problems encountered during the system's development, was validated experimentally. The ability of this technique to produce **mechanically adjustable, bio-inspired cylindrical structures** was further illustrated by the embedding of fiber-reinforced samples in a matrix material.

All in all, all challenges previously found in state-of-the-art solutions were surpassed. This system represents a major advancement in the automated **embedding of continuous fibers in cylindrical structures across different orientations in a multi-axis setting** (see Fig. 4.1). It combines the 3D printing advantages for the incorporation of **multi-material deposition**, achieving the total device fabrication within one single printing process, with **continuous fiber placing** that can pass through the standard planar layers, by changing the printing angle with its **multi-axis capabilities**. It sets the first steps for implementation in biomedical devices fabrication, for example, the lumbar disc's implants, within one single automated process, for both the **annulus fibers** and **endplates**. Taking it into a step forward, it also allows for **customization of fiber orientation and stacking across layers**.

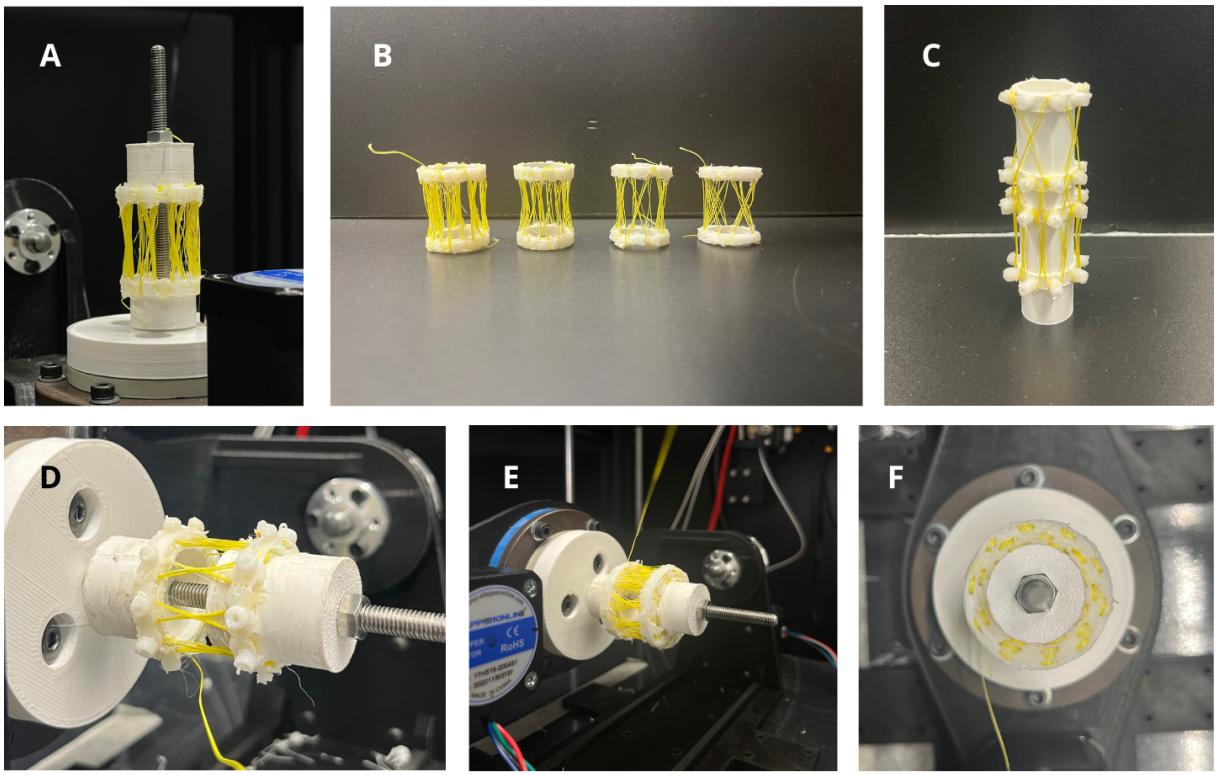

Figure 4.1: Overview of key achieved printed results: (A) Final printed fiber-reinforced structure (B) Showcase of fiber orientation and dimension variation across samples based on different pin spacing (C) Variation of fiber orientation across the same layer (D) Variation of fiber orientation across multiple layers and printing of new loom pins on top of previously printed layers (E) Variation of fiber orientation across multiple layers, side view (F) Variation of fiber orientation across multiple layers, top view.

4.2. Effectiveness of Print Settings on Dimensional Accuracy

The findings confirm that **extrusion thickness, flow rate, and print speed** must be carefully controlled to achieve **high-accuracy prints**. The results indicate that:

- **E100% extrusion** provides the most stable accuracy across all axes, minimizing both under-extrusion and over-extrusion effects.
- **Over-extrusion (E150%)** leads to material accumulation, particularly affecting **height (z-axis) accuracy**, where excess material builds up and disrupts **layer stacking**.
- **Under-extrusion (E50%)** results in **incomplete layer bonding**, negatively affecting **width (v-axis) accuracy** by reducing structural consistency across printed layers.
- **Flow rates above 100%** lead to **excessive material deposition**, particularly affecting **width and height accuracy** due to filament spreading beyond the intended print paths.
- **Print speeds above 15 mm/s** negatively impact **layer adhesion** and **surface smoothness** due to **reduced bonding time**, introducing inconsistencies in both **width (v-axis) and length (x-axis) accuracy**.

Unlike conventional **planar 3D printers**, this system incorporates **rotational motion (u and v-axis)**, adding complexity to **dimensional accuracy**. The **x-axis remains relatively stable**, as it functions similarly to traditional FDM printers, but **the v-axis is particularly sensitive to rotational misalignment**. However, when looking at the results, there are often more pronounced discrepancies in the height cases (x-axis) rather than the width cases (v-axis). One possible explanation could be related to the fact that, unlike in linear movement, rotational one in a conformal surface allows for more area of **redistribution and less material drag**, since there is only one contact point between the loom surface and nozzle, at a given line of G-code.

Height accuracy (z-axis) is directly influenced by **pre-defined layer height settings**, with **E150% extrusion leading to stacking errors** due to excess material flow, since the layer is at a pre-defined height, not leaving much room for material redistribution.

Additionally, print speed affects **both layer adhesion and feature resolution**. Faster speeds (>15 mm/s) result in **weaker layer bonding**, contributing to **misalignment across width and height dimensions**. Conversely, slower speeds improve print resolution but **increase print duration significantly**, when taking into account a full print cycle, highlighting the trade-offs in optimizing settings.

4.3. Effectiveness of Nozzle Modifications

Temperature measurements across modified nozzles revealed that **extended nozzles without additional heating** suffered from thermal losses, leading to clogging and oozing. However, the temperature recovers near the nozzle tip. Some possible explanations can be due to **heat redistribution** from the heater block, **thermal mass stabilization**, and the **filament spending enough time in the heated environment** to regain sufficient temperature before extrusion.

The accuracy results suggest that the primary limitation of the 0.8 mm nozzle lies in its inability to maintain precise extrusion control in the **horizontal plane**, leading to **filament spreading and deformation** rather than a uniform layer deposition. One of the possibilities to justify this relies on the fact that the layer height is set for 0.2 mm preventing more steep discrepancies in the length parameter.

To improve print quality and fiber deposition control, several nozzle modifications were explored. The first tested approach involved using an **M6 Hex Spacer Modification nozzle** to extend the extrusion path. However, as seen in Fig 3.4, the extended internal volume led to a significant drop in temperature within the nozzle body. While the tip temperature remained close to the set value of **210°C**, the drop in the intermediate sections fell below the **170°C threshold**, leading to **partial solidification of the filament before reaching the extrusion point**. This effect, combined with the increased internal diameter, resulted in **material accumulation, clogging, and excessive oozing**, ultimately affecting print consistency.

To mitigate this issue, a second heater block was installed to compensate for heat loss along the nozzle length. However, commercially available extended nozzle solutions, for the set height requirements, start at a minimum **0.8 mm diameter**, which introduces additional **extrusion control challenges**. The **Extended 0.8 mm Nozzle** was tested under optimized temperature conditions, maintaining **210°C at the tip**, but as observed in Fig. 3.5, accuracy remained poor across all three measured dimensions.

In response to these challenges, a **Hybrid Nozzle Design** was developed, integrating an extended nozzle profile while **retaining a smaller nozzle diameter of 0.4mm** to maintain precise material flow. This design was used for the accuracy tests in the previous section, and as shown, it demonstrated significantly improved performance when combined with the **optimal print parameters**. The hybrid nozzle successfully maintained **dimensional accuracy, minimized oozing with lower retraction values (E-0.1 to E-1), and avoided excessive material deposition**, proving to be the most effective solution for multi-axis fiber-reinforced printing.

4.4. Print Bed Modifications and Loom Constraints

The results demonstrate that **print bed stabilization is critical for both fiber accuracy and pin stacking alignment**. The **Final Print Bed Support** consistently outperforms other configurations, exhibiting the lowest deviations and highest repeatability. These findings go by Equation (2.5) that suggests increasing h and decreasing d minimizes the shifting angle, improving bed support stability and printing accuracy.

Opting for a *table-table* (TT) configuration rather than a *head-head* (HH) configuration, significantly altered the effective build volume by introducing additional degrees of rotational freedom. While this increased flexibility in part orientation, it also imposed severe spatial constraints, exponentially reducing the available print volume.

A comparative analysis was performed for the **Creality Ender 5 Plus** and **Creality Ender 5**, pre-

senting the corresponding reduction in effective build volume for TT configurations (Table 4.1). The results demonstrate that the TT setup **reduces the usable volume at a nonlinear** rate as the build dimensions increase.

These results indicate that **increasing the original print volume results in disproportionately greater volume losses in the TT system**. This is due to the necessity of additional clearance volume, which scales with the diagonal movement of the rotating bed.

Table 4.1: Reduction of effective build volume for TT configurations in Creality Ender 5 and Ender 5 Plus.

Configuration	l (mm)	w (mm)	h (mm)	V_{build} (cm^3)	V_{reduced} (cm^3)
TT (Ender 5)	220	220	300	14520	2049
TT (Ender 5 Plus)	350	350	400	49000	21465

Despite this reduction constraint, the **HH configuration** does not suffer from the same exponential volume loss. While HH setups introduce additional mechanical complexity, they allow for **greater scalability** by maintaining a predictable volume reduction trend. However, the increased number of moving components in HH configurations could pose challenges related to **system rigidity and calibration precision**, making the TT system a more practical alternative despite its volume constraints.

The **table-table (TT) printing configuration** introduced clearance constraints that influenced the design and scalability of the loom structures. The results indicated that the **effective print volume was reduced by 16.84%** due to rotational constraints, which required redefining the maximum achievable loom dimensions.

By evaluating the minimum radius required for the ring support, based on pin spacing constraints, it was determined that:

- A **45° spacing (8 pins)** required a minimum radius of **6.37 mm**.
- A **25° spacing (12 pins, annulus fibrosus-inspired)** required a radius of **11.46 mm**.

These findings highlight a critical **design trade-off**: smaller loom radii limit the number of fibers per structure but allow for **compact, high-density fiber placement**, while **larger loom radii permit greater flexibility in fiber spacing but require increased clearance volume**.

4.5. Design Implications

The results from Instron testing of different pin designs revealed that **standard circular pins exhibited the lowest failure force**, while **conformal slicing and adhesive-reinforced pins significantly increased mechanical stability**. The capstan effect during fiber embedding induced shear forces onto the pins, requiring **high bending stiffness** to maintain loom integrity.

Pins with **conformal slicing resisted failure better** due to a greater surface area and load distribution, but their longer print times remain a trade-off. Alternatively, **adhesive-reinforced pins showed the highest failure resistance** while maintaining fabrication efficiency, suggesting an optimized balance between printability and mechanical strength.

These findings confirm that pin deformation and breakage risks can be mitigated by optimizing **pin geometry and surface bonding techniques**, ensuring long-term stability in fiber-reinforced prints.

The tensile tests examining how **pin spacing affects fiber system deformation** demonstrated that smaller angles between pins (higher pin density) lead to **greater resistance against deformation**. The reaction force in the vertical direction increased by pin number increase, confirming that **densely spaced fibers improve structural reinforcement**.

This suggests that systems requiring higher mechanical stability and resistance to strain should employ **higher fiber densities**, while **lower-density configurations** can be used for more flexible structures.

Furthermore, these results validate the **theoretical force distribution model**, demonstrating how applied tensile force scales with pin spacing in multi-axis fiber reinforcement. The system's ability to control these parameters allows for **fine-tuned customization of mechanical performance**.

One of the key findings was that increasing the number of pins per structure resulted in **greater mechanical resistance to deformation**, an effect that aligns with established principles of fiber-reinforced composites. Beyond validating the system's ability to modulate stiffness and torque via fiber placement, these findings demonstrate that the developed **multi-axis fiber embedding technique effectively replicates the mechanical behavior of natural fiber-reinforced biological tissues**.

Notably, the ability to **adjust fiber orientation and density** aligns with the structural characteristics of connective tissues such as the **annulus fibrosus**, where fiber reinforcement plays a crucial role in load distribution and mechanical resilience. Much like the theoretical background explained in Chapter 1, the results emphasize how the outer layers, with less pin spacing, are responsible for a higher **reported stiffness and torque response**. This behavior mirrors the natural adaptation of the annulus fibrosus, where the outer lamellae experience greater tensile loads and thus require **denser, circumferentially arranged collagen fibers** to resist deformation, torsional loads, shock abortion, and support spinal stability.

From Equation (2.13), the force per pin is inversely related to the number of pins. Since each pin bears a fraction of the total force, increasing the **pin count reduces the load per pin**, stabilizing the structure against deformation. This explains why the **8-pin samples exhibit higher torque values** than the 4-pin and 6-pin cases.

However, for a **fixed number of pins**, simply increasing fiber layers does not introduce additional constraints in fiber movement at each pin. The force distribution per pin remains **nearly unchanged**, leading to only a **small torque increase in the 8-pin 6-layer sample.** This further confirms that **fiber organization (pin spacing and layout) is a stronger determinant of mechanical behavior than fiber volume alone.**

According to Equation (2.12), the effective Young's modulus of the structure depends on the fiber and matrix volume fractions. While adding layers increases **total fiber volume** V_f, the lack of significant improvement in torque suggests that stiffness gains have reached a **plateau effect**, where additional fibers do not contribute as effectively to rotational resistance, or the increase in fiber volume was too insignificant compared to the entire composite structure,

The observed results indicate that **pin spacing and fiber routing dominate mechanical performance**, with additional fiber layers reaching a **diminishing return threshold** for improving torque and stiffness.

While the primary objective of this study was not to exactly replicate the full biomechanical behavior of the lumbar disc, it is informative to contextualize the stiffness results against literature values. The highest secant stiffness measured in this study (96.87 kPa for the 45° sample) remains lower than the modulus reported for the native annulus fibrosus, which typically ranges between 0.4 MPa and 2 MPa, (from 45° to 30°) and direction of loading [35, 37, 38]. This discrepancy is expected, as the samples tested here represent **simplified, fiber-reinforced analogues of individual disc layers** rather than a complete disc structure. Contributing factors include the **reduced radius of the samples** (26 mm compared to 45–55 mm in human lumbar discs [35]), **lower fiber content**, and differences in boundary conditions and deformation regimes. Nevertheless, the system effectively captures the **relative contribution of fiber angle and orientation to stiffness and damping**, providing a **tunable foundation** for further development toward **bioinspired annulus fibrosus mimics**.

Another fundamental challenge in **multi-axis fiber weaving** was ensuring that fibers remained **securely embedded** throughout the printing process, ensuring multi-material bonding and printing sequence. The study evaluated different extrusion percentages for fiber locking, revealing that:

- **100% extrusion** caused **over-deposition**, interfering with the loom structure.
- **50% extrusion** resulted in **fiber slippage** and loose embedding.

- **70% extrusion** provided the **optimal balance**, ensuring strong fiber retention without excess material accumulation.

These results go slightly against the theoretical equation for the fiber-locking mechanism. Some possible causes not accounted by it can be related to material spreading, surface interactions and mostly the need for multi-material bonding. It is then concluded that reducing the theoretically obtained values by roughly 30% ends up leading to a more stable print, and subsequent structure for additional layer deposition.

5

Conclusion

5.1. Conclusion

In conclusion, by allowing for controlled, scalable fiber insertion within cylindrical geometries, the developed multi-axis fiber embedding method effectively solved the drawbacks of conventional planar fiber reinforcement and state-of-the-art methods. By combining dual-material extrusion, rotational motion, and an enlarged nozzle assembly, the technology maintained compliance with traditional FDM principles while guaranteeing precise fiber deposition. In addition to enabling precise fiber orientation and real-time tension adjustments, the automated technique showed that continuous fiber-reinforced structures with mechanical properties that could be altered were feasible.

This technique establishes the foundation for completely automated manufacturing of biomedical devices, including lumbar disc implants, where fiber orientation and endplate integration are critical to performance, by fusing 3D printing with multi-material deposition. By offering new opportunities for optimizing material properties and structural configurations in a single, efficient process, this research lays the groundwork for future developments in fiber-reinforced additive manufacturing.

5.2. Future Work

Building on these results, several enhancements and research directions could be pursued to further optimize the system:

Different Multi-axis configurations

Despite their added complexity, exploring other configurations such as the HH, could prove advantageous for preserving reduced printing volume across printer dimensions increase.

Process Optimization for Increased Loom Adhesion

Future studies should investigate heating incorporation on the print bed support as an alternative to adhesives. This could enable **direct thermal bonding**, enhancing loom stability in an automated manner.

Improved Print Stability through Cooling Control

The introduction of an **elongated cooling fan system** could enhance **uniform solidification**, reducing local deformations in the loom prints. Testing different cooling rates would provide insight into optimal print stabilization parameters for multi-axis printing.

Integration of matrix embedding into the system

One key advancement would be to **incorporate the loom and fiber structure into the matrix material within the print process**. Nowadays, there are already printing mechanisms capable of

extruding soft material, such as silicone, which coupled with this proposed system would completely revolutionize the field of fiber embedding automation for biomedical purposes.

Material choice optimisation

This study made use of **PLA thermoplastic material** and **Ultra-High-Molecular-Weight Polyethylene, UHMWPE fiber**, which were suitable for its purpose and demonstrations. As a next step, it is proposed to experiment with different materials that bring the final composite closer to mimicking current implantable artificial lumbar discs. For example, and as mentioned in Chapter 1, using biocompatible solutions that enhance osseointegration such as **PEEK**, **Titanium Alloys (Ti6Al4V)**, **Hydroxyapatite (HA)** coatings and even silicone based elastomers.

This work stands as a pioneering advancement in multi-axis fiber reinforcement for 3D printing, not only demonstrating a refined approach to automating complex fiber architectures but also laying the foundation for a transformative research trajectory that could redefine the integration of fiber reinforcement in additive manufacturing, with biomedical applications extending far beyond lumbar discs to include cardiac, muscular, and soft tissue engineering solutions.

References

[1] Daniela Rus and Michael Tolley. “Design, fabrication and control of soft robots”. In: *Nature* 521 (May 2015), pp. 467–75. DOI: 10.1038/nature14543.

[2] Josie Hughes et al. “Soft Manipulators and Grippers: A Review”. In: *Frontiers in Robotics and AI* 3 (Nov. 2016). ISSN: 2296-9144. DOI: 10.3389/frobt.2016.00069.

[3] Eric Brown et al. “Universal robotic gripper based on the jamming of granular material”. In: *Proceedings of the National Academy of Sciences* 107 (44 Nov. 2010), pp. 18809–18814. ISSN: 0027-8424. DOI: 10.1073/pnas.1003250107.

[4] Thomas George Thuruthel et al. “Control Strategies for Soft Robotic Manipulators: A Survey”. In: *Soft Robotics* 5 (2 Apr. 2018), pp. 149–163. ISSN: 2169-5172. DOI: 10.1089/soro.2017.0007.

[5] Matteo Cianchetti et al. “Biomedical applications of soft robotics”. In: *Nature Reviews Materials* 3 (6 May 2018), pp. 143–153. ISSN: 2058-8437. DOI: 10.1038/s41578-018-0022-y.

[6] Cecilia Laschi et al. “Soft Robot Arm Inspired by the Octopus”. In: *Advanced Robotics* 26 (7 Jan. 2012), pp. 709–727. ISSN: 0169-1864. DOI: 10.1163/156855312X626343.

[7] Barbara Mazzolai et al. “Octopus□Inspired Soft Arm with Suction Cups for Enhanced Grasping Tasks in Confined Environments”. In: *Advanced Intelligent Systems* 1 (6 Oct. 2019). ISSN: 2640-4567. DOI: 10.1002/aisy.201900041.

[8] Yunwen Bo et al. “Advancements in materials, manufacturing, propulsion and localization: propelling soft robotics for medical applications”. In: *Frontiers in Bioengineering and Biotechnology* 11 (Jan. 2024). ISSN: 2296-4185. DOI: 10.3389/fbioe.2023.1327441.

[9] Nina R. Sinatra et al. “Ultragentle manipulation of delicate structures using a soft robotic gripper”. In: *Science Robotics* 4 (33 Aug. 2019). ISSN: 2470-9476. DOI: 10.1126/scirobotics.aax5425.

[10] Yoshikazu Nakajima et al. “Suction-fixing surgical device for assisting liver manipulation with laparoscopic forceps”. In: *International Journal of Computer Assisted Radiology and Surgery* 15 (10 Oct. 2020), pp. 1653–1664. ISSN: 1861-6410. DOI: 10.1007/s11548-020-02239-3.

[11] Javier Bermejo-García et al. “Actuation Strategies for a Wearable Cable-Driven Exosuit Based on Synergies in Younger and Older Adults”. In: *Sensors* 23 (1 Dec. 2022), p. 261. ISSN: 1424-8220. DOI: 10.3390/s23010261.

[12] P. Kannus. “Structure of the tendon connective tissue”. In: *Scandinavian Journal of Medicine Science in Sports* 10 (6 Dec. 2000), pp. 312–320. ISSN: 0905-7188. DOI: 10.1034/j.1600-0838.2000.010006312.x.

[13] Moise Raphael Tsimbo Fokou et al. “A Soft Robotic Fish Actuated by Artificial Muscle Modules (SoRoFAAM-1)”. In: *Journal of Bionic Engineering* 20 (5 Sept. 2023), pp. 2030–2043. ISSN: 1672-6529. DOI: 10.1007/s42235-023-00390-6.

[14] Meng Li et al. “Soft actuators for real-world applications”. In: *Nature Reviews Materials* 7 (3 Nov. 2021), pp. 235–249. ISSN: 2058-8437. DOI: 10.1038/s41578-021-00389-7.

[15] Fergal B. Coulter et al. “Bioinspired Heart Valve Prosthesis Made by Silicone Additive Manufacturing”. In: *Matter* 1 (1 July 2019), pp. 266–279. ISSN: 25902385. DOI: 10.1016/j.matt.2019.05.013.

[16] J. H. Pikul et al. “Stretchable surfaces with programmable 3D texture morphing for synthetic camouflaging skins”. In: *Science* 358 (6360 Oct. 2017), pp. 210–214. ISSN: 0036-8075. DOI: 10.1126/science.aan5627.

[17] P.K. Mallick. *Fiber-Reinforced Composites*. CRC Press, Nov. 2007, pp. 7–8. ISBN: 9780429122064. DOI: 10.1201/9781420005981.

[18] Dervis Ozkan, Mustafa Sabri Gok, and Abdullah Cahit Karaoglanli. “Carbon Fiber Reinforced Polymer (CFRP) Composite Materials, Their Characteristic Properties, Industrial Application Areas and Their Machinability”. In: vol. 124. Springer, 2020, pp. 235–253. DOI: 10.1007/978-3-030-39062-4_20.

[19] Yuzhe Wang et al. “Pioneering healthcare with soft robotic devices: A review”. In: *Smart Medicine* 3 (1 Feb. 2024). ISSN: 2751-1871. DOI: 10.1002/SMMD.20230045.

[20] Bibhas K. Bhunia et al. “3D printing of annulus fibrosus anatomical equivalents recapitulating angle-ply architecture for intervertebral disc replacement”. In: *Applied Materials Today* 23 (June 2021), p. 101031. ISSN: 23529407. DOI: 10.1016/j.apmt.2021.101031.

[21] Martin A. Freilich et al. “The design and fabrication of fiber-reinforced implant prostheses”. In: *The Journal of Prosthetic Dentistry* 88 (4 Oct. 2002), pp. 449–454. ISSN: 00223913. DOI: 10.1067/mpr.2002.128173.

[22] Fionnuala Connolly et al. “Mechanical Programming of Soft Actuators by Varying Fiber Angle”. In: *Soft Robotics* 2 (1 Mar. 2015), pp. 26–32. ISSN: 2169-5172. DOI: 10.1089/soro.2015.0001.

[23] Yali Han, Quan Xu, and Feng Wu. “Design of Wearable Hand Rehabilitation Glove With Bionic Fiber-Reinforced Actuator”. In: *IEEE Journal of Translational Engineering in Health and Medicine* 10 (2022), pp. 1–10. ISSN: 2168-2372. DOI: 10.1109/JTEHM.2022.3196491.

[24] Huma Ozair et al. “Shape Memory Hybrid Composites”. In: *ACS Omega* 7 (41 Oct. 2022), pp. 36052–36069. ISSN: 2470-1343. DOI: 10.1021/acsomega.2c02436.

[25] Mariangela Manti, Vito Cacucciolo, and Matteo Cianchetti. “Stiffening in Soft Robotics: A Review of the State of the Art”. In: *IEEE Robotics Automation Magazine* 23 (3 Sept. 2016), pp. 93–106. ISSN: 1070-9932. DOI: 10.1109/MRA.2016.2582718.

[26] Jiaqing Xiong, Jian Chen, and Pooi See Lee. “Functional Fibers and Fabrics for Soft Robotics, Wearables, and Human–Robot Interface”. In: *Advanced Materials* 33 (19 May 2021). ISSN: 0935-9648. DOI: 10.1002/adma.202002640.

[27] K. K. Chawla. “Short Fiber Reinforced Composites”. In: *Composites Science and Engineering*. Ed. by E. Talbot. Vol. 6. Oxford, UK: EOLSS Publishers, 2010, pp. 45–60. URL: https://www.eolss.net/sample-chapters/c05/E6-36-02-05.pdf.

[28] Khaled Eldressi et al. “Review of recent developments in polymer matrix composites with particulate reinforcements”. In: (Feb. 2024).

[29] Muhammad Azfar Jamal et al. “Additive Manufacturing of Continuous Fiber-Reinforced Polymer Composites via Fused Deposition Modelling: A Comprehensive Review”. In: *Polymers* 16 (12 June 2024), p. 1622. ISSN: 2073-4360. DOI: 10.3390/polym16121622.

[30] Arman Goshtasbi. *Thesis Report 3D Weaving of Continuous Fiber Reinforced Soft Robot*. Apr. 2023.

[31] Hanna Trębacz and Angelika Barzycka. “Mechanical Properties and Functions of Elastin: An Overview”. In: *Biomolecules* 13 (3 Mar. 2023), p. 574. ISSN: 2218-273X. DOI: 10.3390/biom13030574.

[32] Charanpreet Singh, Cynthia Wong, and Xungai Wang. “Medical Textiles as Vascular Implants and Their Success to Mimic Natural Arteries”. In: *Journal of Functional Biomaterials* 6 (3 June 2015), pp. 500–525. DOI: 10.3390/jfb6030500.

[33] Chiara Rinoldi et al. “Fibrous Systems as Potential Solutions for Tendon and Ligament Repair, Healing, and Regeneration”. In: *Advanced Healthcare Materials* 10 (7 Apr. 2021). ISSN: 2192-2640. DOI: 10.1002/adhm.202001305.

[34] Levend Parnas and Nuran Katırcı. “Design of fiber-reinforced composite pressure vessels under various loading conditions”. In: *Composite Structures* 58 (1 Oct. 2002), pp. 83–95. ISSN: 02638223. DOI: 10.1016/S0263-8223(02)00037-5.

[35] Sara Molladavoodi, John McMorran, and Diane Gregory. “Mechanobiology of annulus fibrosus and nucleus pulposus cells in intervertebral discs”. In: *Cell and Tissue Research* 379 (3 Mar. 2020), pp. 429–444. ISSN: 0302-766X. DOI: 10.1007/s00441-019-03136-1.

[36] *The M6-L Artificial Lumbar Disc*. URL: https://m6disc.global/m6-l-lumbar/.

[37] George Youssef, Cesar Lopez, and J Michael Kabo. “Composite mechanics of the multilayer structure of the annulus fibrosus”. In: *Journal of Mechanical Engineering and Biomechanics* 1 (Mar. 2017), pp. 126–134.

[38] Alyah H. Shamsah et al. “Tissue Engineering the Annulus Fibrosus Using 3D Rings of Electrospun PCL:PLLA Angle-Ply Nanofiber Sheets”. In: *Frontiers in Bioengineering and Biotechnology* 7 (Jan. 2020). ISSN: 2296-4185. DOI: 10.3389/fbioe.2019.00437.

[39] Ian J. Wellington et al. “Cervical and Lumbar Disc Arthroplasty: A Review of Current Implant Design and Outcomes”. In: *Bioengineering* 9 (5 May 2022), p. 227. ISSN: 2306-5354. DOI: 10.3390/bioengineering9050227.

[40] Fabio Cofano et al. “Carbon fiber reinforced vs titanium implants for fixation in spinal metastases: A comparative clinical study about safety and effectiveness of the new “carbon-strategy””. In: *Journal of Clinical Neuroscience* 75 (May 2020), pp. 106–111. ISSN: 09675868. DOI: 10.1016/j.jocn.2020.03.013.

[41] Bethany Middleton. “Composites: Manufacture and Application”. In: Elsevier, 2016, pp. 53–101. DOI: 10.1016/B978-0-323-34061-8.00003-X.

[42] Sarah Deener. *HOW IT WORKS: COMPOSITE CONSTRUCTION*. June 2016. URL: https://www.aopa.org/news-and-media/all-news/2016/august/flight-training/how-it-works.

[43] Kaspar Fras Jan and Althoefer. “Soft Fiber-Reinforced Pneumatic Actuator Design and Fabrication: Towards Robust, Soft Robotic Systems”. In: *Towards Autonomous Robotic Systems*. Ed. by Jelizaveta, Zhang Ketao Althoefer Kaspar, and Konstantinova. Springer International Publishing, 2019, pp. 103–114. ISBN: 978-3-030-23807-0.

[44] T. Stalin et al. “Automated Fiber Embedding for Tailoring Mechanical and Functional Properties of Soft Robot Components”. In: *2019 2nd IEEE International Conference on Soft Robotics (RoboSoft)*. IEEE, Apr. 2019, pp. 762–767. ISBN: 978-1-5386-9260-8. DOI: 10.1109/ROBOSOFT.2019.8722752.

[45] Danial Sangian et al. “Three-Dimensional Printed Braided Sleeves for Manufacturing McKibben Artificial Muscles”. In: *3D Printing and Additive Manufacturing* 6 (1 Mar. 2019), pp. 57–62. ISSN: 2329-7662. DOI: 10.1089/3dp.2018.0103.

[46] Wyatt Felt, Khai Yi Chin, and C. David Remy. “Contraction Sensing With Smart Braid McKibben Muscles”. In: *IEEE/ASME Transactions on Mechatronics* 21 (3 June 2016), pp. 1201–1209. ISSN: 1083-4435. DOI: 10.1109/TMECH.2015.2493782.

[47] Yiyue Luo et al. “Digital Fabrication of Pneumatic Actuators with Integrated Sensing by Machine Knitting”. In: *CHI Conference on Human Factors in Computing Systems*. ACM, Apr. 2022, pp. 1–13. ISBN: 9781450391573. DOI: 10.1145/3491102.3517577.

[48] Yi Sun et al. “Design and fabrication of a shape-morphing soft pneumatic actuator: Soft robotic pad”. In: *2017 IEEE/RSJ International Conference on Intelligent Robots and Systems (IROS)*. IEEE, Sept. 2017, pp. 6214–6220. ISBN: 978-1-5386-2682-5. DOI: 10.1109/IROS.2017.8206524.

[49] Snehal Jain et al. “Flexible Fiber Interconnects for Soft Mechatronics”. In: *IEEE Robotics and Automation Letters* 5 (3 July 2020), pp. 3907–3914. ISSN: 2377-3766. DOI: 10.1109/LRA.2020.2982367.

[50] Katie Treggiden. *Oluwaseyi Sosanya invents 3D-weaving machine*. June 2014. URL: https://www.dezeen.com/2014/06/23/oluwaseyi-sosanya-invents-3d-weaving-machine-show-rca-2014/.

[51] Indraneel R. Chowdhury and John Summerscales. “Woven Fabrics for Composite Reinforcement: A Review”. In: *Journal of Composites Science* 8 (7 July 2024), p. 280. ISSN: 2504-477X. DOI: 10.3390/jcs8070280.

[52] K. Rithika and J. Sudha. “Additive Manufacturing of Fiber□Reinforced Composites—A Comprehensive Overview”. In: *Polymers for Advanced Technologies* 35 (12 Dec. 2024). ISSN: 1042-7147. DOI: 10.1002/pat.70002.

[53] T. M. Mohan and A. J. Hart. “Multi-Axis Printing in Additive Manufacturing: Kinematic Considerations and Path Planning Strategies”. In: *Journal of Manufacturing Processes* 45 (2020), pp. 25–33. DOI: 10.1016/j.jmapro.2020.04.005.

[54] Joshua Ray Chen et al. “Three-dimensional printing accuracy analysis for medical applications across a wide variety of printers”. In: *Journal of Medical Imaging* 10 (02 Apr. 2023). ISSN: 2329-4302. DOI: 10.1117/1.JMI.10.2.026501.

[55] Engineering.com. *Printing Bigger and Cheaper with the Multi-Axis Process*. Accessed: February 17, 2025. 2025. URL: https://www.engineering.com/printing-bigger-and-cheaper-with-the-multi-axis-process/.

[56] O V Zakharov, K G Pugin, and T N Ivanova. “Modeling and Analysis of Delta Kinematics FDM Printer”. In: *Journal of Physics: Conference Series* 2182 (1 Mar. 2022), p. 012069. ISSN: 1742-6588. DOI: 10.1088/1742-6596/2182/1/012069.

[57] Ilmawan Mustaqim et al. “Machine Design and Development of CoreXY FDM 3D Printer for Learning”. In: *International Journal of Artificial Intelligence Research* 8 (1 June 2024), p. 128. ISSN: 2579-7298. DOI: 10.29099/ijair.v8i1.1186.

[58] Chengkai Dai et al. “Support-free volume printing by multi-axis motion”. In: *ACM Transactions on Graphics* 37 (4 Aug. 2018), pp. 1–14. ISSN: 0730-0301. DOI: 10.1145/3197517.3201342.

[59] Sitong Xiang et al. “Multi-machine tools volumetric error generalized modeling and Ethernet-based compensation technique”. In: *Proceedings of the Institution of Mechanical Engineers, Part B: Journal of Engineering Manufacture* 230 (5 May 2016), pp. 870–882. ISSN: 0954-4054. DOI: 10.1177/0954405414564407.

[60] Filament2Print. *Direct extrusion and Bowden systems*. Forum post. 2020. URL: https://filament2print.com/gb/blog/94_bowden-direct-extrusion.html.

[61] Freddie Hong et al. “Open5x: Accessible 5-axis 3D printing and conformal slicing”. In: *Conference on Human Factors in Computing Systems - Proceedings*. Association for Computing Machinery, Apr. 2022. ISBN: 9781450391566. DOI: 10.1145/3491101.3519782.

[62] Hao Liu, Zhoupeng Liu, and Siting Hao. “Design of a Throat-extended FDM Extruder for Multi-axis 3D Printing”. In: *Strojniški vestnik – Journal of Mechanical Engineering* (Apr. 2021), pp. 167–179. ISSN: 00392480. DOI: 10.5545/sv-jme.2021.7124.

[63] Martijn Schouten et al. “A Review of Extrusion-Based 3D Printing for the Fabrication of Electro- and Biomechanical Sensors”. In: *IEEE Sensors Journal* 21 (11 June 2021), pp. 12900–12912. ISSN: 1530-437X. DOI: 10.1109/JSEN.2020.3042436.

A

Appendix

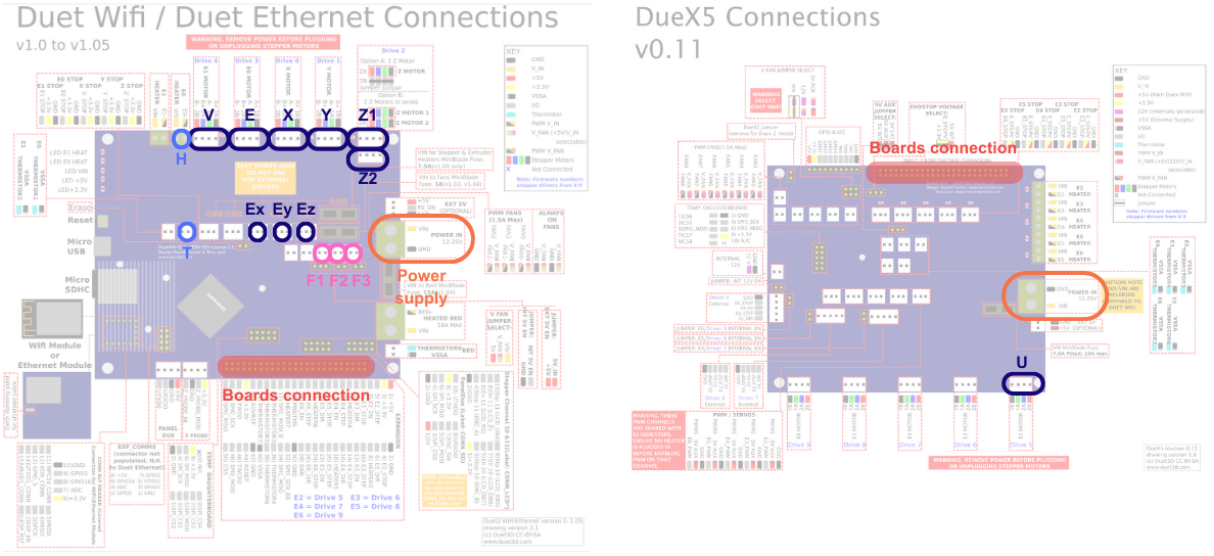

Figure A.1 Duet Operating Boards Schematic Overview

B

Appendix

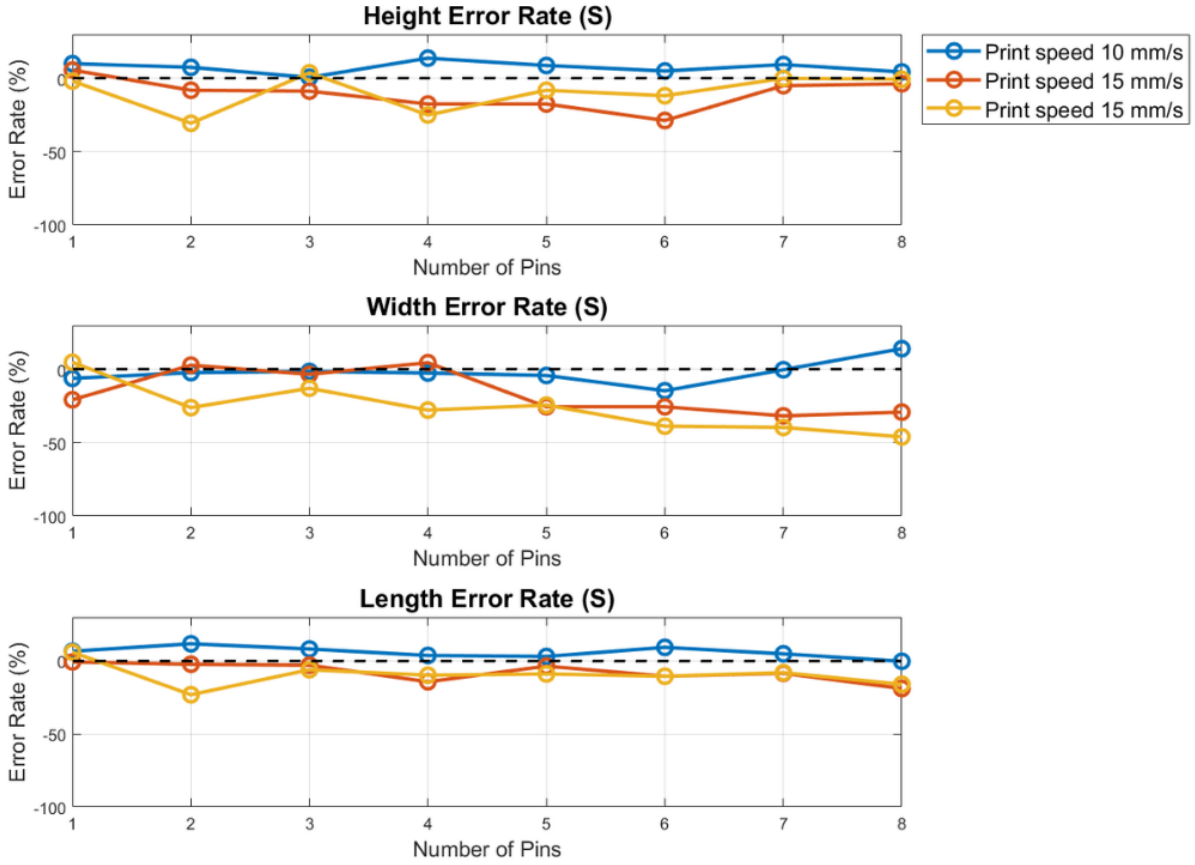

Figure B.1 Print Speed Accuracy Plots

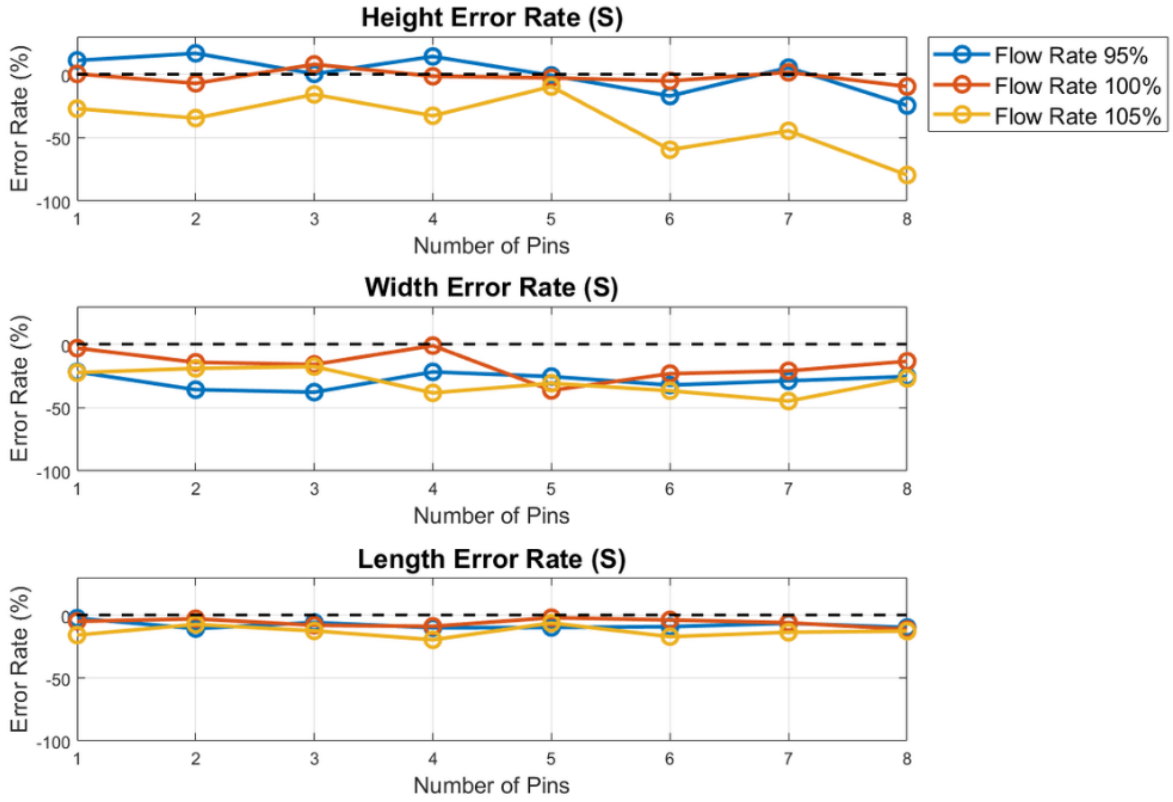

Figure B.2 Flow Rate Accuracy Plots

Table B.1: Loom Pin Dimensions and Printability

Parameter	Value	Justification
Selected angles	90°, 60°, 45°	Balances variation and print time
Minimum pin radius	1.5 mm	Ensures printability with a 0.4 mm nozzle
Minimum clearance	2 mm	loom printing over-dimensions + 2 mm nozzle diameter
Maximum print bed height	80 mm	Allows multiple structures per print
Fiber amplitude range	5 mm - 35 mm	Allows for mimicking of biological structures and feasibility of testing
Minimum loom radius (45° spacing, 8 pins)	6.37 mm	Ensures clearance and print accuracy
Selected loom radius	11.5 mm	Accounts for future added needs of loom structure

C

Appendix

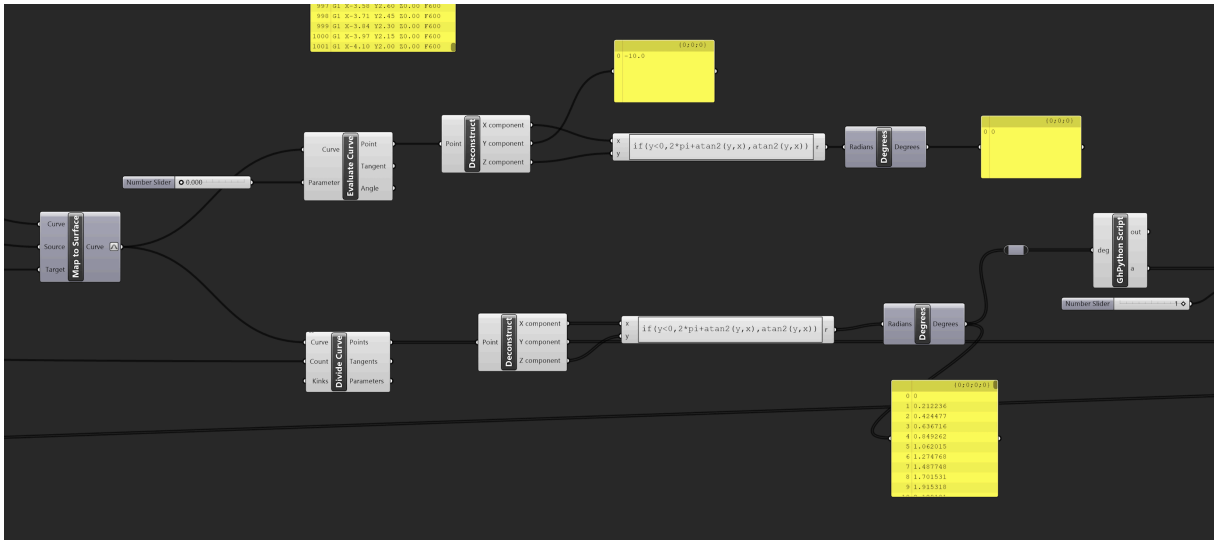

Figure C.1 Fiber G-code Generation Process.

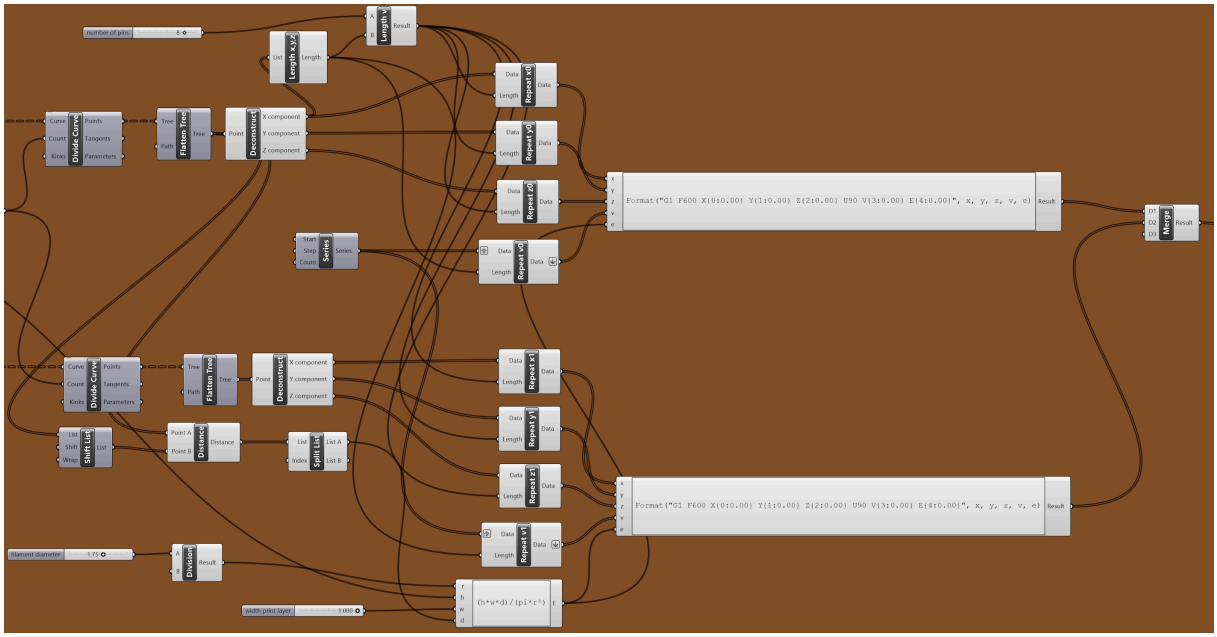

Figure C.2 Loom G-code Generation Process.

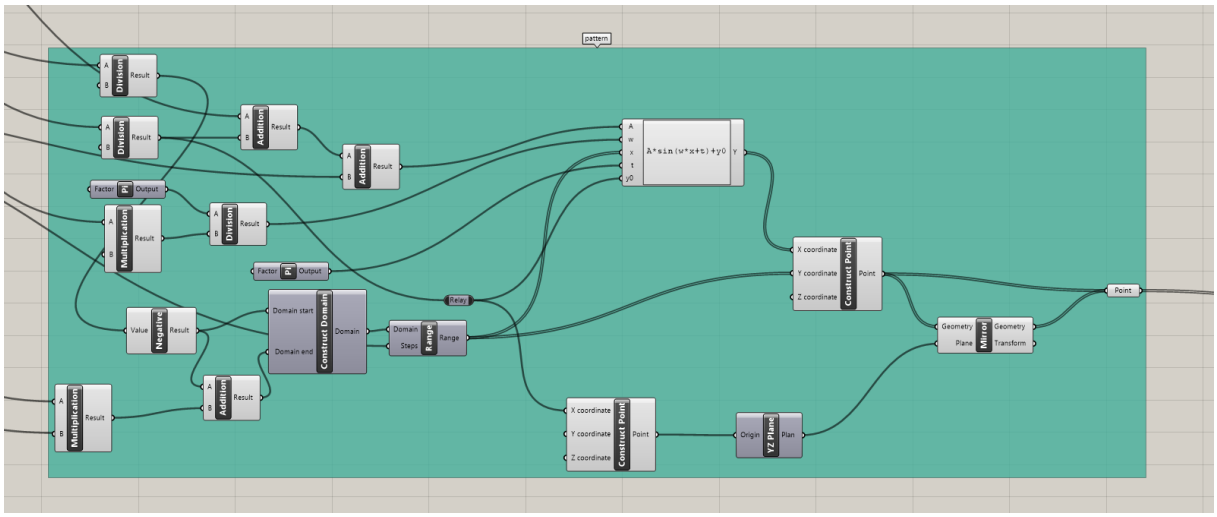

Figure C.3 Fiber Shape Generation Process.